

Organomineralization of Microbialites from Storr's Lake, San Salvador Island, Bahamas:

Calcium Stable Isotope Analysis using TIMS and a ^{42}Ca - ^{43}Ca double spike

Thesis

Presented in Partial Fulfillment of the Requirements for the Degree Master of Science in
the Graduate School of The Ohio State University

By

Brittan Valhalla Wogsland, B.A.

Graduate Program in Earth Sciences

The Ohio State University

2020

Thesis Committee

Elizabeth Griffith, Advisor

Matthew Saltzman, Committee Member

Thomas Darrah, Committee Member

Copyrighted by
Brittan Valhalla Wogsland
2020

Abstract

The isotopic composition and mineralogy of modern microbialites provides us with tools useful for interpreting the formation processes and environments of ancient microbialites. Growing in the hypersaline and turbid Storr's Lake on San Salvador Island in The Bahamas today are microbialites with low levels of photosynthesis and high levels of sulfate reduction-in contrast to many of their modern counterparts. Living planktonic, motile microorganisms and suspended algal and bacterial debris create the high turbidity of the shallow lake (<2 m) and rapidly attenuate sunlight in the water column.

Within Storr's Lake microbial metabolisms induce precipitation of carbonate within microenvironments of the microbial mats. Both high-Mg calcite (HMC) and aragonite are found within a majority of the microbialites measured leading to the hypothesis that the organomineralization process involves a step where HMC transforms to aragonite. Mineralogy and elemental analysis of a wide sampling of microbialites was undertaken to understand the extent of aragonite within Storr's Lake microbialites. It was found that aragonite occurs at water depths greater than 40 cm within the lake and was present in all but one microbialite measured in this study.

New calcium (Ca) stable isotopic analyses from the thermal ionization mass spectrometer using a ^{42}Ca - ^{43}Ca double spike provides evidence for exploring the systems fractionating Ca within Storr's Lake water and microbialites. In contrast to geochemical

data and previous Mg stable isotopic measurements on the same waters, the Ca stable isotopic value ($\delta^{44/40}\text{Ca}$) of water in Storr's Lake is not homogeneous. While the northern sector is primarily influenced by seawater, the southern sector $\delta^{44/40}\text{Ca}$ is shifted away from seawater to lower values, suggesting internal variability within the lake. In both microbialites measured, $\delta^{44/40}\text{Ca}$ is strongly correlated to mineralogy and trace elements in the carbonate. To explore the potential influence of microbial processes on the Ca isotopic composition of the microbialite carbonate, $\Delta^{44/40}\text{Ca}_{\text{carbonate-lake water}}$ was calculated. For the purest aragonite sample measured, $\Delta^{44/40}\text{Ca}_{\text{carbonate-lake water}}$ falls within the range of experimental $\Delta^{44/40}\text{Ca}_{\text{aragonite-water}}$ of biogenic and abiogenic aragonite. This suggests that the Ca within aragonite may or may not be influenced by biological fractionation during its formation within the microbialite.

Dedication

To my mom, who showed me I could do anything.

Acknowledgments

Thank you to everyone who helped me and offered their support during my Master's degree, I could not have done this without you. Thanks to Friends of Orton Hall and American Chemical Society Petroleum Research Fund Award 54853-ND2 awarded to EMG for their crucial monetary support of my research. Additional thanks to Zijian Li for his MS work on Storr's Lake microbialites and everyone who assisted with sample collection in 2016.

My sincerest thanks to my advisor Elizabeth Griffith. You took a chance on a chemist and turned me into a geochemist. I am forever grateful for the opportunity to begin my career in the geosciences with you. Your careful training in the lab has heightened my meticulous tendencies and granted me so many new skills that I will carry with me into my career. Thanks Liz.

To my committee, Matt Saltzman and Tom Darrah, thanks for taking the time to read such a beast of a Master's thesis. I appreciate your varied insight and it has made my project more well-rounded. I truly enjoyed taking field courses with you both and have learned a great deal from working with you.

Special thanks to my lab group and officemates JJ Kim, Sam Carter, Teresa Avila, Chris Conwell, and Datu Adiatma. You all made me feel welcome in Ohio and helped me

through a number of hard times. I could not have made it through this without your encouragement and philosophical lunch time discussions.

To my first year buddies: Lindsey Hernandez and JJ Kim, thank you for the milk tea, excellent friendship, and commiseration over the trials of graduate school. Adolfo Calero, thanks for being such a great friend. Joe Schulze, thanks for always talking about planets with me and being such a chaotic character in Dungeons and Dragons.

To my Dungeons and Dragons party: You guys have kept me sane. I look forward to at least a few more sessions of ridiculous role playing and Jeff getting up to hilarious murder. Thanks to Cole Bradley, Derrick James, Prescott Vayda, and Joe Schulze.

Many more people in SES have helped me through my degree. I shall list a few here, but if you do not find your name, know that I am still grateful to you for making SES the environment it was. Many thanks to Devin Smith, Emma Oti, Oliver McLellan, Jack Dechow, Jaime Price, Mike Braunagel, Angie Rogers, Kira Harris, Karina Peggau, Nicole Whalstrom, LJ Risteski, Amelia Nelson, Myles Moore, and a mountain of others. Thank you all.

Outside Ohio my family and friends have been integral to my completion of this degree. Unending thanks and love to August, Maxwell, Zara, Mimi, Elinor, and my mom. Thanks to my grandparents, Poppy, Papa Ray, and Nanny. You guys have stood up to replace Dad and I am forever thankful for your support.

Finally, I thank Chanelle Chua. You are my oldest and dearest friend and I can never express how grateful I am to have you in my life. Thank you for your endless support. I would not be here without you.

Vita

August 2012-May 2014.....Mary Baldwin University
May 2016.....Vanderbilt University
May 2018-August 2018.....Graduate Research Associate,
School of Earth Sciences,
The Ohio State University
August 2018-August 2019.....University Fellow,
School of Earth Sciences,
The Ohio State University
August 2019-December 2019.....Graduate Teaching Associate,
School of Earth Sciences,
The Ohio State University
January 2020-Present.....Graduate Research Associate,
School of Earth Sciences,
The Ohio State University

Fields of Study

Major Field: Earth Sciences

Table of Contents

Abstract.....	ii
Dedication.....	iv
Acknowledgments.....	v
Vita.....	vii
List of Tables	xi
List of Figures.....	xii
Chapter 1. Introduction.....	1
Microbialite Classifications	2
Formation of Microbialites from Microbial Mats.....	6
Calcium Isotope Systematics	14
Notation.....	14
Calcium Isotopic Fractionation.....	14
Study Goals and Hypotheses	18
Chapter 2. Study Site	23
Chapter 3. Previous Research on Storr’s Lake Microbialites.....	30
Microbialite Morphologies and Distribution	30
Microbial Mat Communities and Relationships to Calcification	33
Mineralogy of Storr’s Lake Microbialites	36
Carbon, Oxygen, and Magnesium Stable Isotopes	36
Chapter 4. Methodology	39
Microbialite Subsample Collection and Preparation	39
X-Ray Diffraction Methodology.....	40
Microbialite Sample Digestion.....	42
Elemental Concentration Methodology	42
⁸⁷ Sr/ ⁸⁶ Sr Sample Preparation and Analysis on TIMS	45

Column Chemistry for Calcium Purification.....	49
Ca Isotopic Measurement on MC-ICP-MS.....	51
Ca Isotopic Measurement on TIMS.....	55
Creation of the Double Spike.....	62
Double Spike Subtraction Procedure.....	64
TIMS $\delta^{44/40}\text{Ca}$ Standard Reproducibility.....	66
Chapter 5. Results.....	69
Microbialite Morphology.....	69
WN1A.....	69
WN2.....	70
WN3.....	72
WN4.....	74
WN5.....	75
WN7.....	76
WN8.....	77
SWN2.....	80
WS1.....	81
WS2.....	82
Mineralogy of Microbialite Subsamples.....	84
Elemental Compositions of Microbialite Subsamples.....	86
$^{87}\text{Sr}/^{86}\text{Sr}$ of Storr's Lake Water.....	89
$\delta^{44/40}\text{Ca}$ of Storr's Lake Water and Microbialites.....	93
MC-ICP-MS.....	93
TIMS.....	96
Chapter 6. Discussion.....	103
Morphology, Mineralogy and Elemental Concentrations.....	103
$^{87}\text{Sr}/^{86}\text{Sr}$ Groundwater Tracing.....	109
$\delta^{44/40}\text{Ca}$ Understanding of Microbialite formational processes.....	114
Chapter 7. Conclusions.....	126
Bibliography.....	128
Appendix A. X-Ray Diffraction Spectra.....	138
Appendix B. Microbialite Subsample Locations.....	151

Appendix C. Laboratory SOPs and checklists	160
C.1 Microbialite Carbonate Subsampling and Preparation Method	160
C.2 Microbialite Carbonate Digestion Method.....	162
C.3 Cation Exchange Column Method for Calcium Isotopes.....	163
C.4 Calcium Column Worksheet	165
C.5 MCI Gel Resin Cleaning Method for Calcium Isotopes	166
C.7 Sr-Spec Column Chemistry Method	167
C.8 Sr-Spec Column Worksheet.....	170
C.9 Loading Sr on Single Re Filaments.....	171

List of Tables

Table 2-1 Maximum reported depth in Storr's Lake for various studies	27
Table 4-1 $^{87}\text{Sr}/^{86}\text{Sr}$ external reproducibility	49
Table 4-2 MC-ICP-MS standards compared to literature values.....	55
Table 4-3 Manual Heating Method for Ca on TIMS	57
Table 4-4 TIMS Automatic Heating Method for Ca on TIMS.....	60
Table 4-5 TIMS Run Parameters	61
Table 4-6 Absolute Isotopes abundances for 43 and 42 Calcium single spikes as measured and as reported (ISOFLEX).....	63
Table 4-7 Creation of the Double Spike	63
Table 4-8 Double spike Ca isotopic ratios determined in this study	64
Table 4-9 Literature $\delta^{44/40}\text{Ca}$ values in comparison to measured values for IAPSO, 915b and Dim Bay seawater	67
Table 4-10 $\delta^{44/40}\text{Ca}$ external reproducibility (this study).....	68
Table 5-1 Elemental and mineralogy data for Storr's Lake microbialites measured in this study.....	85
Table 5-2 $^{87}\text{Sr}/^{86}\text{Sr}$ measured in Storr's Lake water, carbonate, and nearby locations.	91
Table 5-3 Sample description, column recovery and number of replicates for samples measured on MC-ICP-MS at Penn State (Summer 2018)	95
Table 5-4 Ca isotopic values (relative to SRM 915a) for samples measured on MC-ICP- MS at Penn State (summer 2018)	95
Table 5-5 $\delta^{44/40}\text{Ca}$ values measured in Storr's Lake water, carbonate, and local seawater	97
Table 5-6 Selected data from Li, 2017 for microbialite subsamples	101
Table 6-1 Conservative samples from Storr's Lake and surrounding water sources with the carbonate fraction and carbonate $^{87}\text{Sr}/^{86}\text{Sr}$	112
Table 6-2 Calculated lake water $\delta^{44/40}\text{Ca}$ for a range of groundwater influence	118
Table 6-3 Results of two endmember mixing for microbialite $\delta^{44/40}\text{Ca}$	120
Table 6-4 Calculated $\Delta^{44/40}\text{Ca}_{\text{carbonate-lake water}}$ for WN7 and WS1	122

List of Figures

Figure 1-1 Basic classifications for macroscale microbialite morphologies.	3
Figure 1-2 Mesoscale microbialite fabrics.....	4
Figure 1-3 Microscale stromatolite fabrics.	5
Figure 1-4 Alkalinity engine causing precipitation of carbonate within a microbial mat. .	8
Figure 1-5 Darby Island, Bahamas shallow subtidal marine stromatolites	9
Figure 1-6 Three microbial mat types cycling in open marine Bahamian stromatolites..	10
Figure 1-7 Pathway of organomineralization	13
Figure 2-1 Map of the Bahamas, San Salvador Island, and Storr’s Lake.....	25
Figure 2-2 Timing of hurricanes, tropical storms, and sampling trips on SSI.....	28
Figure 2-3 Map of Storr's Lake showing sampling locations	29
Figure 3-1 Ooids and ostracods in thin section from dense micritic lamina of WS1-6....	31
Figure 3-2 Northern Transect of Microbialite Morphologies.....	32
Figure 3-3 Representative images of microbialite morphologies from Storr's Lake	33
Figure 3-4 Dendrogram and relative bacterial abundance plot.....	35
Figure 3-5 Cross plot of $\delta^{18}\text{O}$ and $\delta^{13}\text{C}$ values from microbialites.....	37
Figure 4-1 Sr-spec columns in use for purifying samples.	46
Figure 4-2 Cation exchange columns with MCI gel resin for Ca separation.....	51
Figure 4-3 Sample processing flow for MC-ICP-MS samples.....	52
Figure 4-4 TIMS Cup Configuration and Dynamic Measurement Scheme for $\delta^{44/40}\text{Ca}$..	61
Figure 5-1 Field photo of WN1A and lab photo of dried WN1A.....	70
Figure 5-2 Field photos of WN2 showing fresh color and morphology.....	71
Figure 5-3 The 2 to 3cm scale laminae visible in WN2.	72
Figure 5-4 Field photo of full WN3 sample and inset lab photos.....	73
Figure 5-5 WN4 dried in the lab and side view of WN4 in the field.....	74
Figure 5-6 Field profile photo of WN5 and dried half section photos of WN5.....	75
Figure 5-7 Interior photo of WN7, whole dried microbialite, and field photo of WN7. .	76
Figure 5-8 Field photo of the top of WN8	77
Figure 5-9 Lab photos of WN8 showing full hand sample and half sectioned sample	78
Figure 5-10 Field photo of EN1 and EN1 after drying.....	79
Figure 5-11 Half-sectioned hand sample of SWN2.....	80
Figure 5-12 Interior of WS1 and the full size microbialite	81
Figure 5-13 Field and lab photos of WS2.....	83
Figure 5-14 Positive relationship between Sr:Ca molar ratio and wt% aragonite.....	87
Figure 5-15 Negative trend between Mg:Ca molar ratio and wt% aragonite	88
Figure 5-16 MC-ICP-MS samples plotted along the mass dependent fractionation line .	94
Figure 5-17 Variability of $\delta^{44/40}\text{Ca}$ in Storr’s Lake water relative to various parameters.	98
Figure 5-18 $\delta^{44/40}\text{Ca}$ depth profiles from WS1 and ES1 in Storr's Lake.....	99

Figure 5-19 $\delta^{44/40}\text{Ca}$ lateral transects from both sectors of Storr's Lake	100
Figure 5-20 $\delta^{44/40}\text{Ca}$ of carbonate subsample correlations with various measurements .	102
Figure 6-1 Aragonite and HMC crystal structures for different mole fractions of Mg ..	105
Figure 6-2 Sr distribution coefficient versus mineralogy	106
Figure 6-3 Mg distribution coefficient versus mineralogy	107
Figure 6-4 Chloride and salinity data from this study and Martin and Moore (2008)....	111
Figure 6-5 Calculated mixing lines from Martin and Moore (2008)	113
Figure 6-6 Sr distribution coefficient plotted against $\Delta^{44/40}\text{C}_{\text{carbonate-lake water}}$	122
Figure 6-7 Ca isotope values collated by Krause et al. (2018) with this study.....	124
Figure 6-8 Data from Blattler et al. (2012) with this study	125
Figure A-1 WN1A-i XRD Spectra	139
Figure A-2 WN1A-ii XRD Spectra	139
Figure A-3 WN2-i XRD spectra	140
Figure A-4 WN2-ii XRD Spectra	140
Figure A-5 WN2-iv XRD Spectra	141
Figure A-6 WN2-iii XRD Spectra	141
Figure A-7 WN3-i XRD Spectra	142
Figure A-8 WN3-ii XRD Spectra	142
Figure A-9 WN4-i XRD Spectra	143
Figure A-10 WN4-ii XRD Spectra	143
Figure A-11 WN5-I XRD Spectra	144
Figure A-12 WN5-VI XRD Spectra	144
Figure A-13 WN5-IX XRD Spectra	145
Figure A-14 WN8-i XRD Spectra	145
Figure A-15 WN8-ii XRD Spectra	146
Figure A-16 WN8-iii XRD Spectra	146
Figure A-17 EN1-i XRD Spectra.....	147
Figure A-18 EN1-ii XRD Spectra.....	147
Figure A-19 SWN2-i XRD Spectra	148
Figure A-20 SWN2-ii XRD Spectra.....	148
Figure A-21 WS2-t XRD Spectra	149
Figure A-22 WS2-b XRD Spectra	149
Figure A-23 WS1-i XRD Spectra	150
Figure A-24 WS1-6 XRD Spectra	150
Figure B-1 Subsamples Locations for WN1A	151
Figure B-2 Subsample locations for WN2.....	152
Figure B-3 Subsample locations for WN3.....	153
Figure B-4 Subsample locations for WN4.....	154
Figure B-5 Subsample locations for WN5.....	155
Figure B-6 Subsample Locations for WN8	156
Figure B-7 Subsample Locations for EN1	157
Figure B-8 Subsample Locations for SWN2	158
Figure B-9 Subsample Locations for WS2	159

Chapter 1. Introduction

Microbial mats are present within many environments on Earth and have been for the past 3 billion years, but only in select environments do they calcify into microbialites which can be studied in the fossil record (Dupraz and Visscher, 2005; Dupraz et al., 2009; Riding, 2011c). Microbialites are defined as “*organosedimentary deposits that have accreted as a result of a benthic microbial community trapping and binding detrital sediment and/or forming the locus of mineral precipitation*” (Burne and Moore, 1987). Studying modern microbialites provides detailed information about the range of environments where microbialites form today, whereas information about the environments forming ancient fossilized microbialites is inferred from measurements of the rock. With a better understanding of the types of modern environments that microbialites form in and their related morphologies and geochemistry, formation of fossilized microbialites can be understood with more accuracy. Sedimentary structures resembling microbialites could be used as signatures of extraterrestrial life if discovered on other planets and identified as biologically influenced (Russell et al., 1999; Brake et al., 2002; Riding, 2011c). Geochemical and microfabric analyses are the primary mechanisms for determining biological influence on carbonate structures resembling microbialites, but are not always diagnostic, especially in ancient systems (e.g., Choudhuri et al., 2016).

Many stable isotopic analyses are used to illuminate the lithification and early diagenetic processes occurring within modern microbialites with application to ancient samples (e.g., Dupraz et al., 2013). The objective for this research was to investigate the lithification and

organomineralization processes occurring in Storr's Lake microbialites, because of their similarity to Pre-Cambrian and Phanerozoic microbialites (Mann and Nelson, 1989). Calcium (Ca) stable isotopes have been utilized in other systems to explore the extent of biotic or abiotic control on carbonate precipitation (e.g., Gussone et al., 2003). A systematic approach to the study of stable Ca isotopes along with previous isotopic, elemental, and crystallographic information had not been done in Storr's Lake and its microbialites, nor in any other carbonate microbialite forming environment.

This thesis contributes to answering the following questions: *How does the Ca stable isotopic composition of microbialites reflect the likely biological influence on the precipitation of calcite and aragonite? How does the Storr's Lake system compare to other low temperature carbonate systems that have been studied with Ca stable isotopes?*

Microbialite Classifications

Stromatolites and thrombolites fall under the umbrella term microbialites and are differentiated by their internal structures (Riding, 2011b). Many morphologies can be present within the same environment, such as a lake, due to localized changes in environmental conditions like water depth (Paul et al., 2016).

Fabric classifications of microbialites are crucial for comparability of data between the literature and the rock record. At the scale of whole microbialites, here referred to as macroscale, external shape is used as the primary descriptor. Macroscale microbialite classifications vary widely (Figure 1-1). Energy level, water depth, relief of the microbialite above the sediment (controlled by sedimentation and accretion rates), and the primary phyla of microbes within the mat are thought to create different macroscopic morphologies (Hoffman, 1976; Mann and Nelson, 1989; Dupraz et al., 2011; Riding, 2011a).

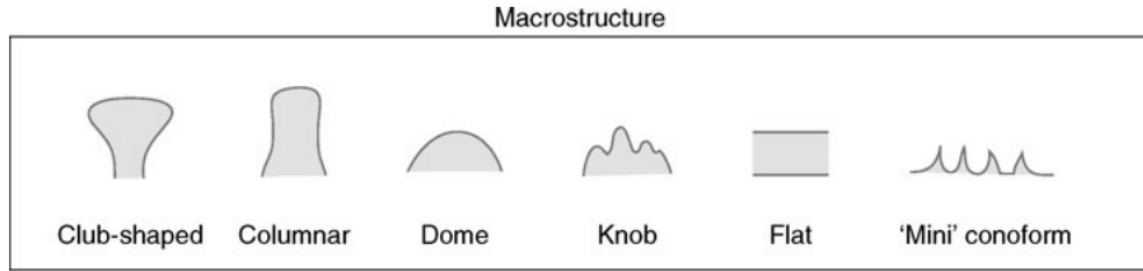


Figure 1-1 Basic classifications for macroscale microbialite morphologies (modified from Dupraz et al., 2011).

When describing the internal structure of microbialites, the structures visible to the naked eye, mesoscale structures, are identified first. There are four primary mesoscale structure classifications (Figure 1-2): stromatolites are laminated; thrombolites are clotted; dendrolites are dendritic; and leiolites are aphanitic (Burne and Moore, 1987; Dupraz et al., 2011; Riding, 2011c, 2011a).

Thrombolites and stromatolites are the primary microbialites identified in modern environments. There is a spectrum of fabrics between thrombolite and stromatolite exemplified by the microbialites in Storr’s Lake, San Salvador Island, Bahamas (this study; Dupraz et al., 2013; Paul et al., 2016; Li, 2017). Some of Storr’s Lake’s microbialites have fine stromatolitic laminations, others are wholly clotted, and many have clotted laminations (Mann and Nelson, 1989; Dupraz et al., 2013; Paul et al., 2016; Li, 2017). The microbialites with clotted laminations are known as thrombotic stromatolites (Riding, 2011b). Dendrolites are similar to thrombolites, except for the branching structure of the microbial carbonate clots. Dendrolites commonly formed in Cambrian reefs and can be difficult to differentiate from thrombolites in older literature (Riding, 2011b). In leiolites, the internal carbonate structure is aphanitic or

structureless, such as the grain-dominated, continuously sediment trapping leiolites discovered in late Miocene deposits within the Sorbas Basin, SE Spain (Braga et al., 1995).

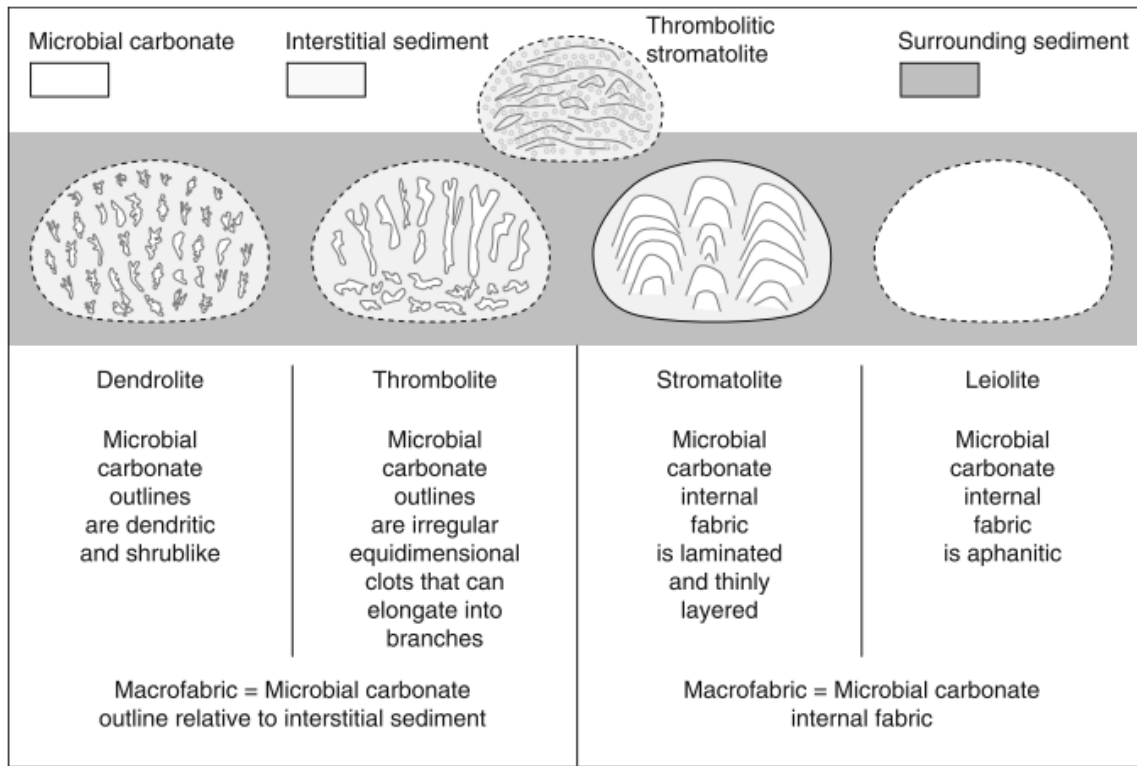


Figure 1-2 Mesoscale microbialite fabrics from Riding (2011b).

Microscale classifications of microbialites use microscopy to describe the grains and/or crystals present within microbialites and any-microscale continuations of mesoscale structures. The microscale classification endmembers for microbialites are coarse grained, fine grained (micritic), and sparry (crystalline) (Boggs, 2006; Riding, 2011a). The distribution of microscale fabrics are shown in the tertiary diagram below (Figure 1-3) (Riding, 2011a). The most renowned example of coarse grained stromatolites are those in Shark Bay, Australia (Hoffman,

1976). Sparry stromatolites are not technically microbialites because they are generally considered to be abiogenic in nature, like the sinters formed at hot springs (Riding, 2011c). Fine grained stromatolites include those found within Storr's Lake and can include peloidal and micritic fabrics or a mixture of the two (Riding, 2011a; Dupraz et al., 2013).

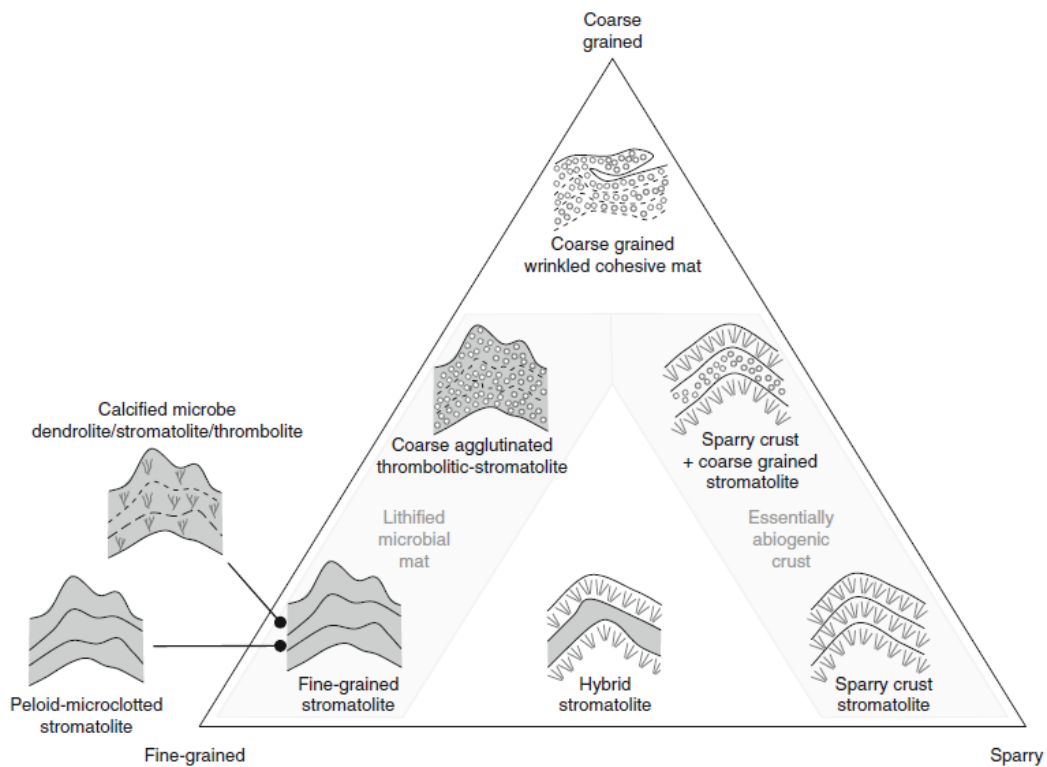


Figure 1-3 Microscale stromatolite fabrics from Riding (2011b).

With the large variety of morphologies within microbialites, specificity and clarity of utilized classifications are crucial to any discussion of microbialites both in the modern and within the rock record.

Formation of Microbialites from Microbial Mats

With the wide variety of microbes that make up microbial mats and build microbialites, researchers have studied multiple microbialite formational mechanisms. In general, microbial mats can form microbialites by trapping wind- or waterborne sediment and/or precipitating carbonate within microenvironments of the microbial mat through interactions of microbe metabolisms with the environment, though the proportion of each varies by locality (e.g., Burne and Moore, 1987; Dupraz and Visscher, 2005; Dupraz et al., 2011). However, even if microbial mats trap a significant amount of sediment and build coarse grained microbialites, preservation in the rock record is more likely if the sediment is lithified through mineral precipitation following the formation of coarse grained laminations (Dupraz and Visscher, 2005).

The specific microbial pathways that contribute to the development of microbialites and the reasons why not all microbial mats lithify is an active area of research (Dupraz et al., 2009). Multiple models have been created for microbialite lithification in specific environments (e.g., Glunk et al., 2011; Dupraz et al., 2013). By combining modern metagenomic and RNA sequencing and stable isotopic analyses (C, O), we can start to understand more about how microbialites form complex morphologies and which groupings of metabolic pathways induce calcification (Foster and Green, 2011; Paul et al., 2016). Carbon and oxygen stable isotopic analyses have also been used to illuminate lithification processes (e.g., Dupraz et al., 2013). Other carbon and oxygen stable isotope studies use the record provided by microbialites to interpret the paleoenvironmental history of a locality (e.g., Buongiorno et al., 2019). Buongiorno et al. (2019) used $\delta^{13}\text{C}$ to understand organic matter cycling within microbialites and $\delta^{18}\text{O}$ to reconstruct evaporation and salinity records for their study site (a closed basin lake).

Biogenic carbonate can be formed by microbes through either biomineralization or organomineralization. The primary difference between these two processes is the genetic intent of biomineralization (Perry et al., 2007; Dupraz et al., 2009). For example, in the phytoplankton *Emiliana huxleyi* the precipitation of coccoliths (biogenic calcite) is a genetically controlled intracellular process regulated through ion transport (MacKinder et al., 2011). Whereas carbonate precipitation through organomineralization is biologically influenced or induced by the microbial mat, but is not genetically controlled (Perry et al., 2007; Dupraz et al., 2009). Organomineralization creates “*minerals precipitated by interaction with organopolymers, bioorganic, and/or non-biological organic compounds, without evidence of direct skeletal, intracellular or extracellular biological control*” (Perry et al., 2007; Dupraz et al., 2009).

Under the umbrella of organomineralization, biologically influenced precipitation is the “passive mineralization of organic matter,” which influences the crystal structure and resulting geochemistry of the precipitate (Dupraz et al., 2009). Biologically induced precipitation results from metabolic changes to the environment which cause precipitation and also influence the structure and geochemistry of the resultant crystals (Dupraz et al., 2009). Calcium carbonate precipitation is controlled by the saturation state of the mineral, which is dependent on the ion activity product of the solution (activity of Ca^{2+} and CO_3^{2-} multiplied) and the solubility product of the mineral under the specific conditions (Stumm and Morgan, 1996). The alkalinity engine is thought to drive most organomineralization within a microbial mat through a change in saturation state caused by internal (e.g., sulfate reduction) or external (e.g., increased evaporation) stimuli to precipitate biologically influenced and/or induced carbonate (Figure 1-4; Dupraz et al., 2011). Within these systems, organic matter binds Ca^{2+} removing its ability to bind to carbonate ions and precipitate carbonate minerals (Glunk et al., 2011).

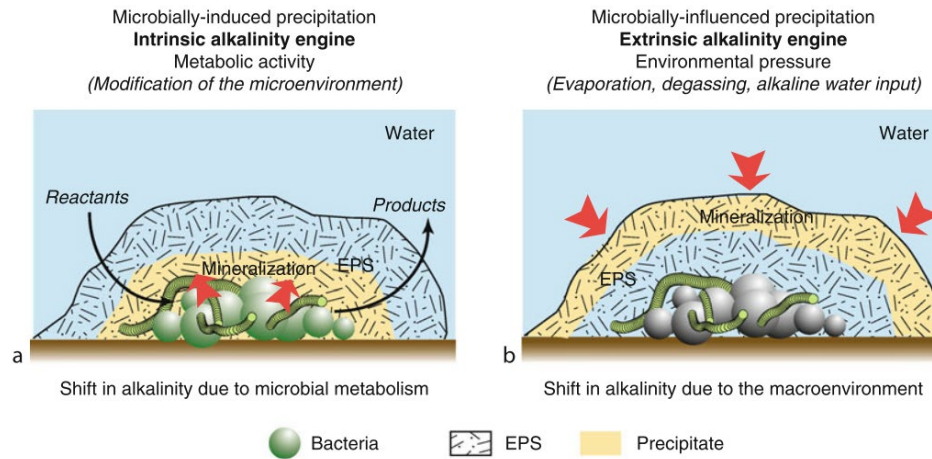


Figure 1-4 Alkalinity engine causing the precipitation of carbonate within a microbial mat from (A) internal stimulus of metabolic activity or (B) external stimuli from environmental pressures (Dupraz et al., 2011).

Open marine Bahamian stromatolites (Figure 1-5) grow in many different locations throughout the Bahamas within intertidal and subtidal environments characterized by high wave energy and strong tidal currents (Dupraz et al., 2011). The characteristic laminations seen in these stromatolitic microbialites are created through cycling of the microbes within the already laminated microbial mat (Dupraz et al., 2009). Due to environmental changes, different microbial metabolisms dominate the microbial mat at different times and in different locations within the mat. This laminae formation mechanism can be applied to other stromatolites and microbial mat cycling can occur on daily, seasonal, or annual scales in different environments.



Figure 1-5 Darby Island, Bahamas shallow subtidal marine stromatolites with inset showing distinct laminations (Dupraz et al., 2011).

Bahamian stromatolites are representative examples of modern marine stromatolite formational mechanisms. Within Bahamian stromatolites there are three distinct phases of microbial mat growth that produce different products (Figure 1-6), which can be identified in both a scanning electron microscope and thin section (Dupraz et al., 2011). Microbial mat types are characterized by the primary microbe present. The three mat types found in Bahamian marine stromatolites are characterized by the primary microbe present and mat cycling is primarily controlled by sediment influx (Figure 1-6; Dupraz et al., 2011). Mat type 1, dominated by *Schizothrix* (a filamentous cyanobacterium) forms unlithified grain layers by trapping ooid sand within sticky extracellular organic matter (EOM) and binding the ooids through upward growth of cyanobacteria (Dupraz et al., 2011; Bowlin et al., 2012). Mat type 2, a biofilm dominated by heterotrophic bacteria including sulfate reducing bacteria, consumes the EOM produced by type

1 and precipitates a thin layer of aragonitic micrite, which holds the bound ooids in place (Dupraz et al., 2011). Mat type 3, dominated by *Solentia* (an endolithic coccoid cyanobacteria), micritizes the trapped ooids and cements them together through the precipitation of aragonite within and between grains (Dupraz et al., 2011). In order for mat types 2 and 3 to colonize over type 1, there must be a cessation in sediment deposition. The longer sediments are not deposited, the more time type 3 has to thoroughly lithify the uppermost ooid layer (Dupraz et al., 2011). The environmental controls on these open marine Bahamian stromatolites provides an inconsistent seasonal record of the region due to the stochastic nature of weather patterns (Dupraz et al., 2011; Bowlin et al., 2012).

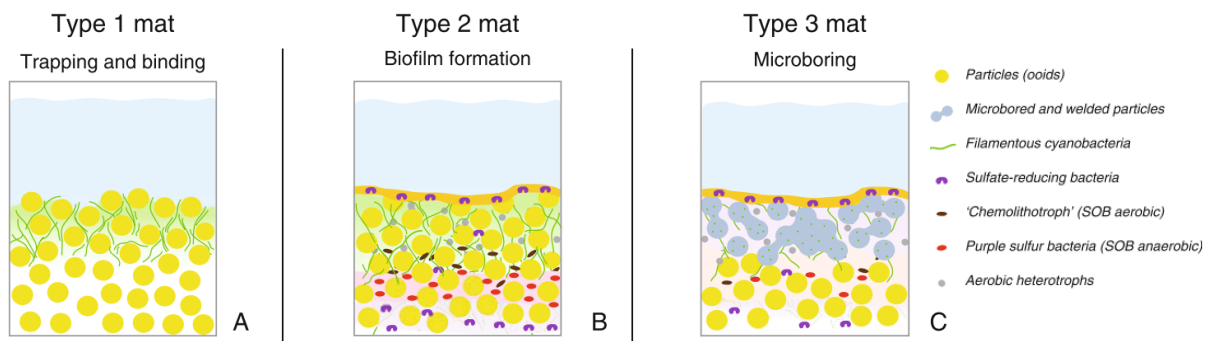


Figure 1-6 Three microbial mat types cycling in open marine Bahamian stromatolites; modified from Dupraz et al. (2011).

In hypersaline environments, the cycling of microbial mats is similar to that of marine environments. For example, Glunk et al. (2011) studied the specific pathways of microbially mediated carbonate precipitation occurring within microbial mats coating the bottom of the hypersaline lake, Big Pond on Eleuthera, The Bahamas. The microbial mats in Big Pond produce

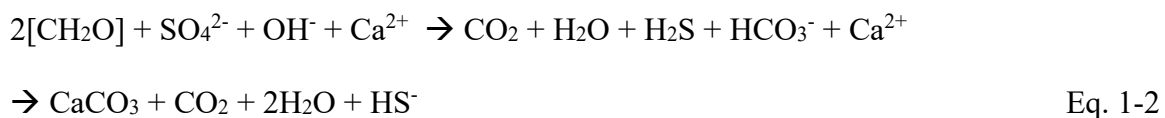
flat lying layers of micritic calcium carbonate alternating with organic layers in addition to stromatolitic heads deeper in the lake (Glunk et al., 2011). At the surface of the microbial mats cyanobacteria colored orange from UV degradation protects the healthy green phototrophic cyanobacteria below, followed by phototrophic purple sulfur bacteria and the first calcium carbonate layer (Glunk et al., 2011). Sulfur cycling within the mat has been qualitatively mapped using silver foil and the highest concentration of sulfate reducing activity was localized around the micritic layers within the microbialites (Glunk et al., 2011). Sulfate reducing bacteria were implicated as the primary inducer of carbonate precipitation (in this and other systems) through changes to the microenvironment of the microbial mat including the saturation index of carbonate and the removal of extracellular organic matter (EOM) inhibiting Ca^{2+} mobility (Braissant et al., 2007; Glunk et al., 2011; Krause et al., 2012).

In both marine and hypersaline environments, sulfate reducing bacteria plays an important role in the precipitation of calcium carbonate to form (and preserve) microbialites. Generally the surface of microbial mats is dominated by photosynthetic bacteria that produces an excess of organic matter (equation 1-1), including EOM (Dupraz and Visscher, 2005; Dupraz et al., 2009).



Extracellular organic matter is made up of extracellular polymeric substances (EPS), such as proteins and polysaccharides, and low-molecular weight organic carbon (LMWOC). Negatively charged functional groups on EOM, such as carboxyl groups, bind divalent cations like Ca^{2+} and Mg^{2+} and potentially prevent carbonate precipitation (Braissant et al., 2007; Glunk

et al., 2011). Below the photosynthetic bacteria all the oxygen within the microbial mat is rapidly consumed by heterotrophy, which allows anaerobic heterotrophic bacteria, primarily sulfate reducing bacteria (SRB), to dominate and consume EOM within the micro-environment of the microbial mats (equation 1-2) (Dupraz and Visscher, 2005; Dupraz et al., 2009; Glunk et al., 2011).



The consumption of EOM causes multiple changes to the microenvironment which lead to the precipitation of carbonate, and production of additional EPS by SRB is thought to influence the morphology of the carbonate minerals (Braissant et al., 2007). First and foremost, the alkalinity of the system is increased as SRB degrades EOM and produces bicarbonate (HCO_3^-) which drives the carbonate equilibrium to produce more carbonate ions and favors the precipitation of calcium carbonate (equation 1-2) (Dupraz et al., 2004, 2009; Glunk et al., 2011). Additionally, the degradation of EOM releases Ca^{2+} ions from the negative functional group metal complexes (e.g., aspartic acid- Ca^{2+}) (Dupraz and Visscher, 2005; Dupraz et al., 2009). This liberation of Ca^{2+} ions, increases the activity of Ca^{2+} , which subsequently increases the saturation state of calcium carbonate.

Some systems are thought to have incomplete degradation of EOM, where the LMWOC are preferentially consumed by the SRB. The Ca^{2+} ions remain bound to EPS, but are partially available for the nucleation of calcium carbonate (Dupraz et al., 2013). From there the mineralization of EPS can occur and/or continued EPS degradation occurs and calcium carbonate

precipitates on nucleation sites (Dupraz and Visscher, 2005; Dupraz et al., 2013). These processes are summarized in Figure 1-7.

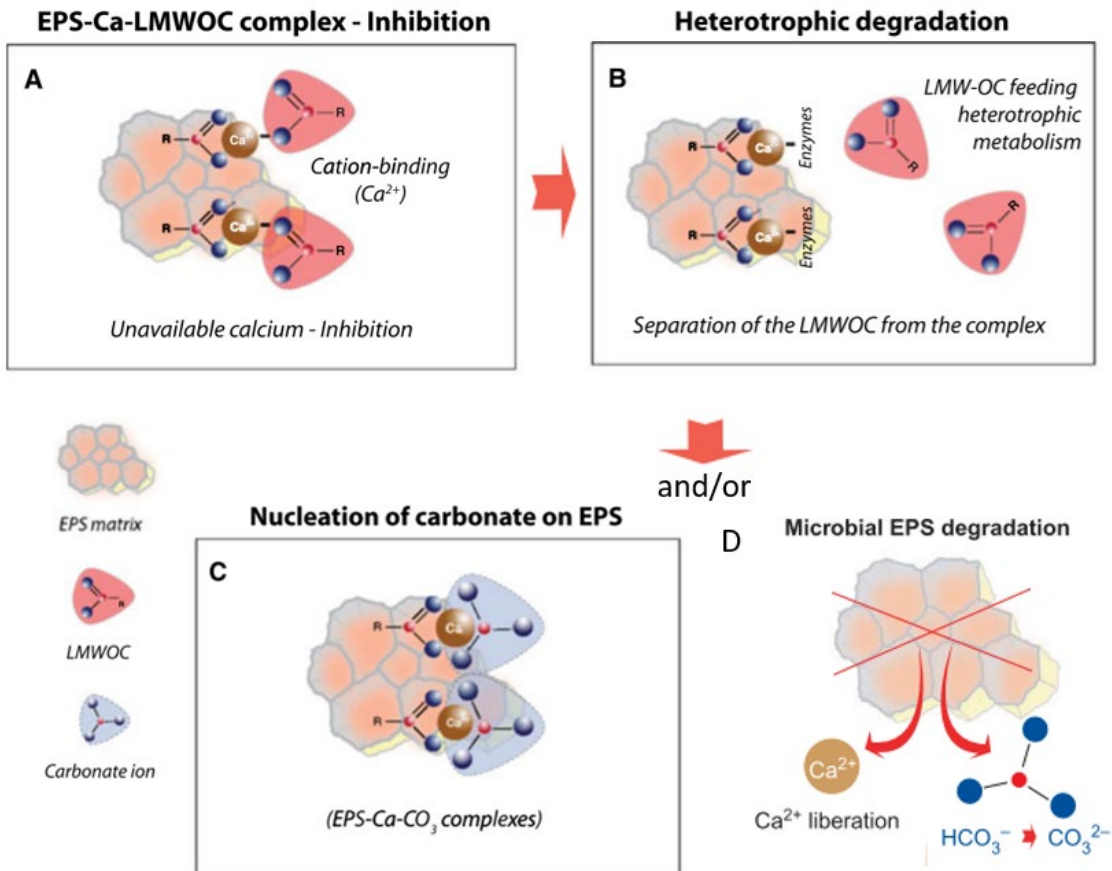


Figure 1-7 Pathway of organomineralization from (A) Ca^{2+} inhibition to (B) heterotrophic degradation to (C) carbonate nucleation on EPS and/or (D) Ca^{2+} liberation. Modified from Dupraz et al. (2013) and Dupraz and Visscher (2005).

Calcium Isotope Systematics

Notation

Stable isotopes, such as Ca, are usually reported in permil (per thousand) as a delta value. Delta values compare the isotopic ratio of interest between the sample and a standard (equation 1-3) (Heuser et al., 2002). The isotope ratio utilized is $^{44}\text{Ca}/^{40}\text{Ca}$ because these two isotopes of Ca are the most abundant with natural abundances of 96.97% for ^{40}Ca and 2.086% for ^{44}Ca (Gussone et al., 2016b, chap. 5). Additional standards are measured and reported in the same fashion as samples to ensure comparability between data sets.

$$\delta^{44/40}\text{Ca} = \left[\frac{(^{44}\text{Ca}/^{40}\text{Ca})_{\text{sample}}}{(^{44}\text{Ca}/^{40}\text{Ca})_{\text{standard}}} - 1 \right] \times 1000 \quad \text{Eq. 1-3}$$

Fractionation between phases or species A and B is described using $\Delta^{44/40}\text{Ca}_{\text{A-B}}$ (equation 1-4) (Sharp, 2017, pp. 2–10). Here, $\Delta^{44/40}\text{Ca}_{\text{A-B}}$ is used to discuss the fractionation between precipitate (A) and the precipitating solution (B).

$$\Delta^{44/40}\text{Ca}_{\text{A-B}} = \delta^{44/40}\text{Ca}_{\text{A}} - \delta^{44/40}\text{Ca}_{\text{B}} \quad \text{Eq. 1-4}$$

Calcium Isotopic Fractionation

Mass-dependent isotopic fractionation is the process through which, the isotopes of an element are distributed differently based on their masses between components of a system. This fractionation can occur during chemical reactions, phase changes, and/or diffusion. The lighter isotopes are preferred in reactions because bonds between lighter isotopes are easier to break and

form (Faure and Mensing, 2005, p. 694). There are two primary types of mass-dependent isotopic fractionation: kinetic and equilibrium (Young et al., 2002). Equilibrium fractionation is a quantum mechanical phenomena controlled by the small differences in vibrational bond energy and atomic mass of molecules in a system that has reached equilibrium (Shahar et al., 2017; Sharp, 2017, pp. 1–14). In crystalline phases, equilibrium isotopic fractionation concentrates the heavier isotope(s) within the stronger bonds (Shahar et al., 2017). Generally, the stronger bonds have higher oxidation state, higher covalent bond character, and lower coordination numbers (Shahar et al., 2017).

Kinetic fractionation is controlled by the small differences in the rate of a reaction for molecules with different masses (i.e., isotopes) and occurs with unidirectional reactions or phase changes, including biologically mediated reactions and diffusion (Faure and Mensing, 2005, p. 698). Temperature is usually the primary control on kinetic fractionation, such as the unidirectional evaporation of seawater into unsaturated air. Metabolic isotopic fractionation generally falls under kinetic fractionation because it is ultimately controlled by biological reactions, which are primarily unidirectional (e.g., fractionation during photosynthesis) (Smith and Ziegler, 1990; Sharp, 2017, pp. 1–13).

With Ca isotopes there is some debate over whether mass-dependent isotopic fractionation occurs largely due to kinetic or equilibrium processes, especially in disparate systems (Boulyga, 2010). When it comes to the precipitation of carbonate, the largest Ca isotopic mass-dependent fractionation effects are likely kinetic (Lemarchand et al., 2004; Gussone et al., 2005; Fantle and Depaolo, 2007). Natural systems may also have some spatial control on the isotopic composition ($\delta^{44/40}\text{Ca}$) of the carbonate due to variability in $\delta^{44/40}\text{Ca}$ of the precipitating

fluid, either from the isotopic evolution of the fluid or from differential fluid inputs (Holmden et al., 2012).

In environments where Ca^{2+} is not limiting, such as marine environments, precipitation rate is primarily controlled by the diffusion of CO_3^{2-} to the liquid-crystal boundary and any Ca^{2+} inhibitors that are present (e.g., EOM bonding, Mg^{2+} , sulfate) (Lemarchand et al., 2004; Gussone et al., 2005). Generally, with increasing precipitation rate the isotopic fractionation of Ca between the solid carbonate and the fluid decreases (Tang et al., 2008a). Increasing temperature increases precipitation rate, likely due to the increased concentration of CO_3^{2-} in warmer waters due to the effect of temperature on the carbonate equilibrium speciation and increased ion diffusion rates of Ca^{2+} (Millero, 1995; Gussone et al., 2005). Empirically, the Ca isotopic composition of both abiogenic and biogenic calcite and aragonite increases by 0.02‰ per 1°C increase, which represents a decrease in isotopic fractionation relative to the fluid (Gussone et al., 2005). The temperature effect on Ca isotopic fractionation could also be an equilibrium effect caused by increased vibrational bond energy of carbonate with increasing temperatures, thereby decreasing the isotopic fractionation occurring during precipitation from seawater at higher temperatures (and increasing the $\delta^{44/40}\text{Ca}$ value).

Given the temperature ranges recorded for Storr's Lake (21 to 38.5°C), the maximum temperature effect on the isotopic fractionation between lake water and CaCO_3 due to temperature is 0.35‰ (this study, Paull et al., 1992; Gussone et al., 2005; Dupraz et al., 2013; Paul et al., 2016). However, because of the large EOM-Ca complexes, which limit diffusion of complexed Ca^{2+} , I expect the temperature effect to be below 0.1‰ following the kinetic mechanism described by Gussone et al. (2003). More importantly, all of the measured microbialites yield a precipitation temperature of 25.1°C calculated from their measured $\delta^{18}\text{O}$

values using the equation of Craig (1965) and the $\delta^{18}\text{O}$ of the lake water (Paull et al., 1992). Recent microbialite $\delta^{18}\text{O}$ data from Li (2017) falls in the same range and suggests an even smaller temperature range in which the microbial mats precipitate carbonate. This recent data further indicates that there will not be any temperature effect on microbialite $\delta^{44/40}\text{Ca}$ in Storr's Lake (Li, 2017). Other studies of Ca isotopic fractionation during carbonate precipitation have not consistently reproduced the temperature controlled fractionation from Gussone et al. (2003); it seems to only exist under specific circumstances (Boulyga, 2010).

When comparing different calcium carbonate polymorphs (calcite and aragonite), Gussone et al. (2005) concluded that precipitation rate and temperature cannot explain the observed differences. They observed a distinct 0.6‰ difference between $\delta^{44/40}\text{Ca}$ values for biogenic calcite (including high-Mg calcite) and biogenic aragonite at all temperatures, which suggests a strong mineralogical control on Ca isotopic fractionation in marine-like environments (Gussone et al., 2005). This difference in isotopic fractionation between polymorphs could be caused by different bond strengths, coordination numbers, or interactions at the liquid-crystal boundary for different lattice structures all of which dominate equilibrium isotopic fractionation and impact kinetic isotopic fractionation (Gussone et al., 2005).

Furthermore, given the usage of Ca^{2+} in the production of EPS and in other microbial mat metabolisms, one would expect to see measurable biogenic isotopic fractionation between the $\delta^{44/40}\text{Ca}$ of the lake water and the carbonate in addition to mineralogical fractionation (Harouaka et al., 2016). Harouaka et al. (2016) found a distinct 0.3‰ $\delta^{44/40}\text{Ca}$ biological fractionation of gypsum precipitated in the presence of sulfur oxidizing bacteria. In carbonates, biological fractionation of $\delta^{44/40}\text{Ca}$ is less distinct. Gussone et al. (2005) studied the $\delta^{44/40}\text{Ca}$ biological fractionation in skeletal HMC and aragonite for various marine organisms and found distinct

temperature trends for biogenic carbonate and inorganic carbonate ($\sim 0.02\text{‰}$ per $^{\circ}\text{C}$). These ranges were used by Krause et al. (2018) to see if biological fractionation of $\delta^{44/40}\text{Ca}$ was observable in carbonate peloids precipitated in the presence of aerobic heterotrophic bacteria. However, they could not distinguish between inorganic carbonate and their biogenic carbonate, possibly due to mixed mineralogy of their carbonate samples (Krause et al., 2018).

Study Goals and Hypotheses

Understanding the formation of microbialites, with an extensive fossil record, will provide insight into our own planet's history and potentially help to find evidence of life on other planets. The primary goal of this study is to use Ca stable isotopes to understand organomineralization and lithification within the microbialites of Storr's Lake on San Salvador Island, The Bahamas. To do this I will interrogate: **(1) the mineralogy distribution within Storr's Lake microbialites; (2) the Ca isotopic composition of the lake water; (3) the primary controls on Ca isotopic fractionation within the microbialites.**

(1) The distribution of mineralogy within the microbialites needs to be characterized so the relationship between mineralogy and microbialite carbonate $\delta^{44/40}\text{Ca}$ can be quantified. *I hypothesize that microbialites with more accommodation space (i.e., deeper water; greater than $\sim 40\text{cm}$ depth in the water column at the time of collection) will all have a transition from high-Mg calcite to aragonite because they were able to grow tall enough that heterotrophy dominates within the interior of the microbialite and the transformation from high-Mg calcite to aragonite can start to occur.* Microbialites were collected in January 2016 following Hurricane Joaquin in October 2015. At the time of collection, the deepest depth measured in Storr's Lake was 125 cm at WS1 (Figure 2.3). Previous research showed that the primary carbonate phase in Storr's Lake microbialites was high-Mg calcite (HMC) except for those collected from deeper depths (>40

cm), with subsamples up to 96 wt% aragonite (Paul et al., 2016; Li, 2017). Li (2017) theorized that heterotrophic metabolisms deeper in the microbialite releases bound Mg which increases the Mg/Ca ratio in the microenvironment and promotes the transformation of HMC into aragonite, as observed in travertines by Greer et al. (2015).

(2) To compare microbialite $\delta^{44/40}\text{Ca}$ values from different parts of the lake (Hypothesis 3), the variability of lake water $\delta^{44/40}\text{Ca}$ needs to be understood. *I hypothesize that the Ca isotope budget within the lake will be dominated by seawater and uniform throughout Storr's Lake similar to that for Mg and Sr isotopes (Li, 2017; this study).* Geochemically, the major ion relationships of the lake water are indistinguishable from local seawater collected at the same time and are consistent throughout the lake (Li, 2017). The lake water samples collected from various locations and depths within Storr's Lake were filtered at the time of collection and most of the water samples were collected at the same locations and depths at which a microbialite was collected and measured to test Hypothesis 3.

I expect lake water to be indistinguishable from the median seawater $\delta^{44/40}\text{Ca}$ value of $1.90 \pm 0.18\text{‰}$ (relative to SRM915a) determined from 53 published values (Fantle and Tipper, 2014). Groundwater input to the lake could alter the $\delta^{44/40}\text{Ca}$ value since its estimated $\delta^{44/40}\text{Ca}$ value is 0.85‰ (relative to SRM 915a), which is very different from seawater (Neumann et al., 1989; Holmden et al., 2012). The Ca in groundwater on San Salvador is sourced from the Pleistocene or Holocene limestone it flows through and is estimated from groundwater measured in Florida Bay (Neumann et al., 1989; Holmden et al., 2012). Given the low Ca concentration in San Salvador Island groundwater (2 mmol/L) compared to the lake water (10 mmol/L), unless there was an excess of groundwater any perturbation to the $\delta^{44/40}\text{Ca}$ value of the lake water

would be masked by the high lake water (and seawater) Ca concentrations (Li, 2017). Future work should measure the $\delta^{44/40}\text{Ca}$ value of San Salvador Island groundwater.

The process of organic matter bonding with Ca^{2+} ions in the water column (Glunk et al., 2011) could also shift the $\delta^{44/40}\text{Ca}$ of Storr's Lake away from that of seawater. To estimate the isotopic fractionation of Ca between organic matter complexes and hydration spheres, bond lengths were used to determine the stronger bond, where the shorter bond is stronger and would preferentially contain more heavy isotopes (Shahar et al., 2017). Taking the difference of the ionic radius of Ca^{2+} (1.0 Å) and the hydrated radius of Ca^{2+} (4.12 Å) serves as a rough estimate of the bond length of the water- Ca^{2+} complexes (3.12 Å) (Nightingale, 1959). In comparison, the ion cavity of ligands that bind Ca^{2+} ranges from 1.3-1.6 Å and when the ionic radius of Ca^{2+} (1.0 Å) is subtracted, the estimated bond length is 0.3-0.6 Å, which is much smaller than the water- Ca^{2+} complex estimated bond length (Lehn and Sauvage, 1975). This relationship between bond lengths suggests that the EPS- Ca^{2+} complexes in the water column contain more of the heavier isotopes, decreasing the $\delta^{44/40}\text{Ca}$ value of the lake water. However, this is the same effect predicted by increases in groundwater to the lake. Without measurements of the amount of organic matter in the same water, any shift in lake water $\delta^{44/40}\text{Ca}$ to lower values could be from groundwater or formation of EOM complexes. Lake water organic matter content (dissolved and particulate) was not measured in this study and therefore cannot be correlated to $\delta^{44/40}\text{Ca}$.

Lake water $\delta^{44/40}\text{Ca}$ could alternatively be enriched in heavy Ca isotopes due the precipitation of carbonate from waters removing preferentially the lighter Ca isotopes. An enrichment of $\delta^{44/40}\text{Ca}$ of lake water at deeper depths could be from carbonate precipitation at depth. In these cases, I would expect lake water $\delta^{44/40}\text{Ca}$ to correlate significantly with $\text{SI}_{\text{calcite}}$

and $SI_{\text{aragonite}}$ or depth. However, this is probably unlikely because major cations are homogeneous in the lake and suggest it is well mixed by wind (Li, 2017).

(3) *I hypothesize that mineralogy (aragonite vs HMC) is the main control on the Ca isotopic composition of the microbialites.* Storr's Lake is similar enough to marine environments (where Ca is not limiting), that mineralogy would be the primary control on Ca isotopic fractionation occurring during microbialite formation. Furthermore, if hypothesis 2 is true and the $\delta^{44/40}\text{Ca}$ of lake water is homogeneous, then any variability in the microbialite's Ca isotopic composition that cannot be explained by mineralogy is likely caused by additional isotopic fractionation from the interaction of Ca^{2+} with organic matter within the microbial mats during carbonate precipitation.

Early diagenetic processes could alter the carbonate $\delta^{44/40}\text{Ca}$ through localized dissolution and re-precipitation in addition to the precipitation of carbonate cements. The effect of recrystallization and carbonate cementation on $\delta^{44/40}\text{Ca}$ is determined by the Ca^{2+} source of the carbonate, whether it is from lake water or an isotopically evolved microbialite pore water (potentially more enriched in heavy Ca from precipitation of carbonate or from the release of heavy Ca bound to EOM due to heterotrophic degradation).

With the assumption that mineralogy is the primary control on the isotopic fractionation of Ca during precipitation, I can use the difference between the $\delta^{44/40}\text{Ca}$ values of the precipitate and the precipitating solution to investigate additional impacts of biological processes occurring within the microbialites and during microbialite formation. The $\delta^{44/40}\text{Ca}$ values for different mineral phases within the microbialites will be compared to the values of the lake water to determine the relationship between the precipitate and bulk solution ($\Delta^{44/40}\text{Ca}_{\text{carbonate-lake water}}$). When compared to experimental data, the $\Delta^{44/40}\text{Ca}_{\text{carbonate-lake water}}$ in Storr's Lake might show

additional effects of biological fractionation on the different mineral phases. For example, the Ca could fractionate due to its bonds with EOM in the microbial mat. In HMC, the expectation is that Ca interaction with EOM will shift $\Delta^{44/40}\text{Ca}_{\text{HMC-lake water}}$ to reflect published values for biogenic HMC relative to its precipitation solutions (Gussone et al., 2005). However, it is possible that the lake water is not the precipitating solution for the carbonates deeper in the microbialite and that instead they are precipitating from a more isotopically evolved lake water within the pores of the microbialite.

Two primary possibilities exist for the $\delta^{44/40}\text{Ca}$ values of aragonite if it inorganically replaces HMC as the more stable phase in the lake following organic matter degradation within the microbialite, as suggested by Greer et al. (2015). If the pore spaces are in communication with the lake water (i.e., open system), the expectation is that $\Delta^{44/40}\text{Ca}_{\text{aragonite-lake water}}$ will reflect published values for inorganic aragonite relative to its precipitation solution. If pore spaces are instead closed to lake water Ca^{2+} , then the reservoir of Ca would be influenced by Ca from HMC. In this case, the aragonite would have a more negative value than expected if it had precipitated directly from Ca dissolved in lake water. Likely, the difference between HMC and aragonite would be less than the expected 0.6‰ from Gussone et al. (2005). However, it is unlikely that the pore spaces are not in communication with the lake water, because the $\delta^{18}\text{O}$ values are in equilibrium with the lake water throughout the microbialites previously studied (Paull et al., 1992; Li, 2017).

Chapter 2. Study Site

One of the most distinct modern microbialite mound forming environments is Storr's Lake on San Salvador Island in The Bahamas (Figure 2-1). Storr's Lake is a hypersaline and turbid, coastal lake located on the windward side of San Salvador Island (Paull et al., 1992). Separated from the sea by Pleistocene and Holocene eolian dunes on the eastern shore of the lake, Storr's Lake is about 7.3 km long and varies in width from 1.3 km to 50 m (Figure 2-1C) (Zabielski, 1991). The high salinity of the lake changes based on the amount of rainfall received and the amount of evaporation occurring (~37 PSU in winter and ~40-60 PSU in summer) (Dupraz et al., 2013; Paul et al., 2016; Li, 2017). The high turbidity is caused by suspended planktonic organisms and decaying plant matter (Dupraz et al., 2013; Paul et al., 2016; Li, 2017). Microbialites grow within the lake and have been studied for many years by multiple researchers due to their similarity to Pre-Cambrian and Phanerozoic thrombolites and stromatolites (Mann and Nelson, 1989; Neumann et al., 1989; Paull et al., 1992; Pinckney et al., 1995; Brigmon et al., 2008; Dupraz et al., 2013; Paul et al., 2016; Li, 2017). Transects from previous microbialite research utilized in this study are shown in Figure 2-1C.

San Salvador Island (SSI) lies east of the Great Bahamas Bank as the eastern most island in the Bahamas Archipelago on its own isolated platform (Figure 2-1A) (Myroie and Carew, 1995). The eastern shore of SSI drops off steeply into the Atlantic Ocean. The primary surface rock of SSI is recent carbonate deposits as Bahamian platform deposition was largely controlled by eustatic sea levels (Curran, 1997). Bedrock on SSI primarily consists of carbonate rich prograding sequences from the Upper Cretaceous and Tertiary periods separated by paleosols

and surface deposits representative of sea level low stands (Myloie and Carew, 1995; Martin and Moore, 2008). Many lakes and ponds populate SSI with a range of salinities and a large portion of them are connected to the ocean through tidal channels or karstic plumbing within the island (Martin and Moore, 2008).

Fresh water and salt water flow paths within SSI have been traced using radiogenic Sr and a mass balance model estimating the mineral contribution of Sr (Martin and Moore, 2008). The mineral Sr contribution was then used to estimate the radiogenic Sr value of the bedrock the water was flowing through, with which the age was determined using the McArthur seawater $^{87}\text{Sr}/^{86}\text{Sr}$ curve (Martin and Moore, 2008). Age of the bedrock was used to calculate the depth of flow within the island (Martin and Moore, 2008). From this analysis, Martin and Moore (2008) determined that the maximum depth of seawater flux within SSI was a few tens of meters. The age of the associated bedrock had a maximum age of 4.68 Ma (Martin and Moore, 2008). However, they did not study Storr's Lake, likely because its formational history and shallow depth suggests minimal groundwater influence.

Described as a high stand depression, Storr's Lake was created by the flooding of basins to create a lagoon, which was closed through sedimentation along the coast (Park Boush et al., 2014). The lagoon was thought to have formed through the flooding of three bedrock basins separated by sills around 4300 ± 70 ^{14}C years ago (Zabielski, 1991). Bedrock in Storr's Lake was exposed on the shallow edges of the lake and within the "Narrows" (Mann and Nelson, 1989). The northern basin was flooded first, and the central and southern basins followed in succession creating a tidally influenced lagoon. The basins were then closed off from the sea as a N-S spit grew southward and the lake became largely evaporative (Zabielski, 1991). Modern Storr's Lake is divided into two sectors, north and south, where the southern sector experiences slightly higher

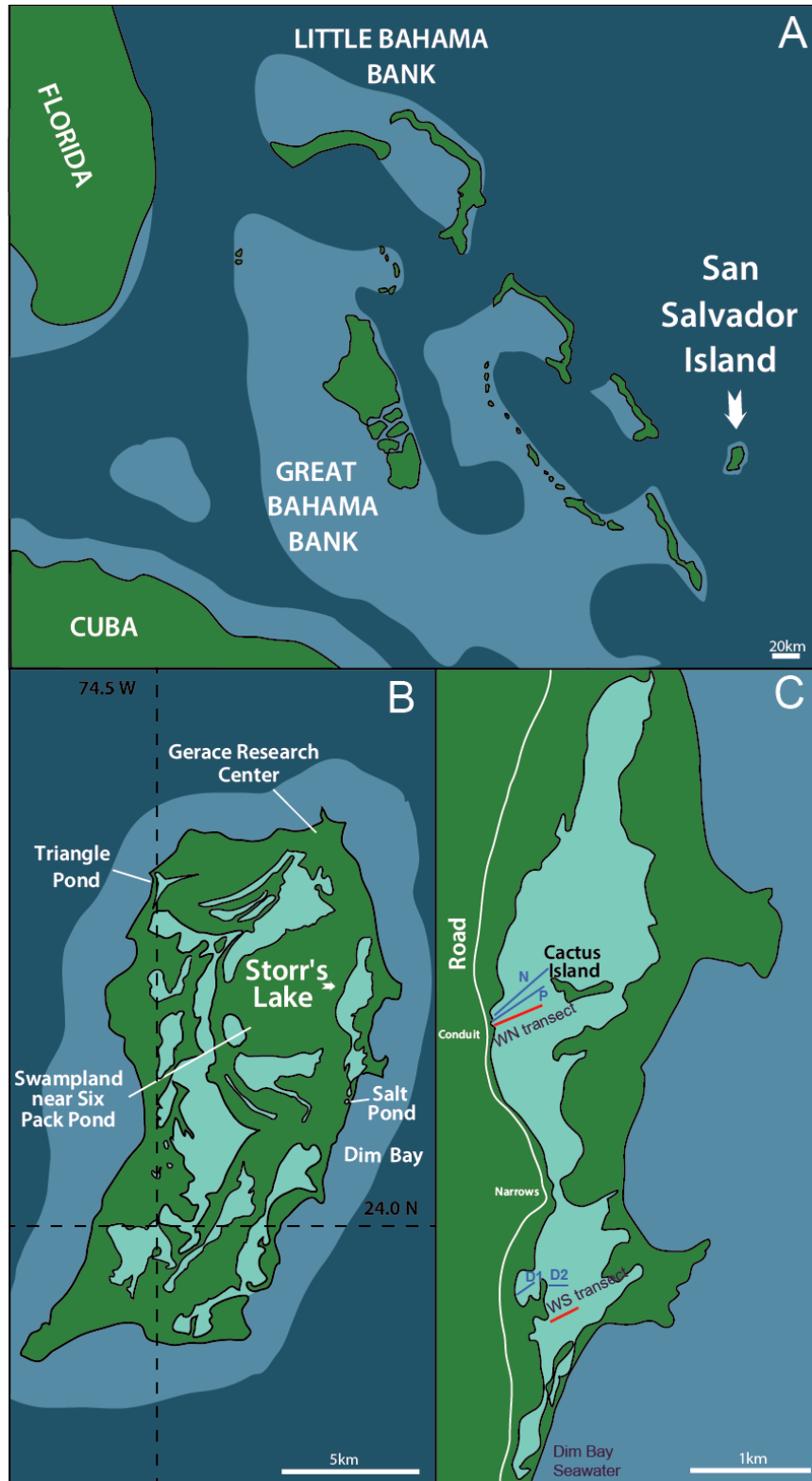


Figure 2-1 These maps show the Bahamas (A), San Salvador Island (B), and Storr's Lake (C) with the many transects from previous researchers in blue (Modified from Li, 2017). (P- Paul et al., 2016; N – Neumann et al., 1989; D – Dupraz et al., 2013). Transects in this study are shown in red.

salinities in the summer and the northern sector has brackish surface water inflow through several identified conduits which have caused a freshening of the lake water near the labeled conduit at times in the past (Figure 2-1, e.g., Paul et al., 2016). The labelled conduit was sampled for this study on either side of the road it flows under, where conduit-N is on the west side of the road and conduit-S is on the east side of the road, closer to Storr's Lake. During some periods this conduit has been completely dry (Elizabeth Griffith, personal communication).

The water chemistry of Storr's Lake has been studied for many years with an observed temperature range from 21 to 38.5°C, where the highest values were measured in the shallower southern sector of the lake during the summer (Paull et al., 1992; Dupraz et al., 2013). Water depth has inferred fluctuations of up to 26 cm using the extent of microbial mats on the shoreline during the dry season and the water level has increased as much as 14 cm after a moderate rain event (Mann and Nelson, 1989). Documentation of yearly lake water fluctuations showed a depth change of about 16 cm annually between 1985-1986 and about 30 cm between 2011-2013 (Mann and Nelson, 1989; Paul et al., 2016). The salinity of the lake water is highly dependent on the precipitation input, because SSI is an arid environment and there is no riverine influx except the tenuously flowing conduits.

The deepest depths in the lake are reported from the northern sector, above Cactus Island. A selection of the deepest lake depths measured by researchers is shown in Table 2-1. From this collection of data, I can estimate that a roughly 50 cm change in lake water is possible between sampling trips with extended time gaps and during different seasons. For more comparability between future studies related to depth relationships, a specific spot for measuring the maximum depth of Storr's Lake should be agreed upon and utilized on every sampling trip.

Table 2-1 Maximum reported depth in Storr's Lake from various studies

Data Set	depth	Date of measurement
<i>This Study/ Li, 2017</i>	125 cm	January 2016
<i>Paul et al., 2016</i>	~1.3 m	May 30-June 3, 2013
<i>Paull et al., 1992</i>	~1 m	1987
<i>Mann and Nelson, 1989</i>	~1.5 m	1985

In addition to the conduit discussed in this study, previous researchers have witnessed tidal fluctuations in conduits on the far north lake shore (Mann and Nelson, 1989). The color difference between the inflowing and the outflowing water allowed the researchers to keep track of the flow direction and the seawater-like salinity of the inflowing water may indicate tidally influenced local groundwater influx into the lake (Mann and Nelson, 1989). However, no tidal fluctuations were detected in the lake level, likely because of the small volume of water exchanged (Mann and Nelson, 1989).

Rainfall on the island is highly variable (annual range from 920 mm to 1210 mm) and large storm systems can contribute an appreciable portion of the yearly rainfall if they pass over San Salvador Island (Gamble and Jordan, 2004). Despite the decrease in lake water salinity associated with rainfall events, the lake water is constantly supersaturated in calcite and aragonite (Paul et al., 2016). Large rainfall events such as hurricanes passing over the lake can freshen the water enough for mollusks, gastropods, and ostracods to survive in the lake (Sipahioglu, 2008). The timing of hurricanes passing over SSI and the timing of sampling for this research and other studies utilized is shown in Figure 2-2 (Gaines, personal communication).

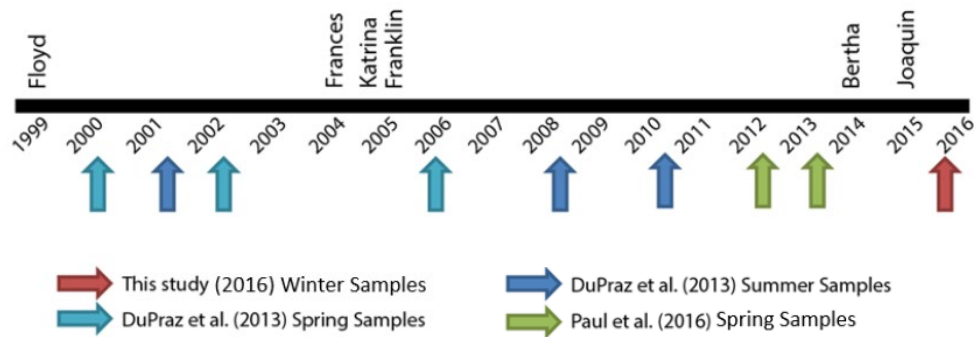


Figure 2-2 Timing of hurricanes and tropical storms hitting SSI and timing of sampling for this study and others discussed herein. Modified from E. Gaines (personal communication) with data from NOAA (National Hurricane Center, 2016).

Water and microbialite samples for this study were collected in January 2016 following Hurricane Joaquin in October 2015. Some fish were seen in lake during sample collection. Most of the microbialites collected had microbial mats on their surface. Transects and locations of sampled microbialites and waters are shown in Figure 2-3. Filled circles represent locations where microbialites and waters were collected. Additional waters were collected in May 2017 by Dr. David Wronkeiwicz from the Missouri University of Science & Technology.

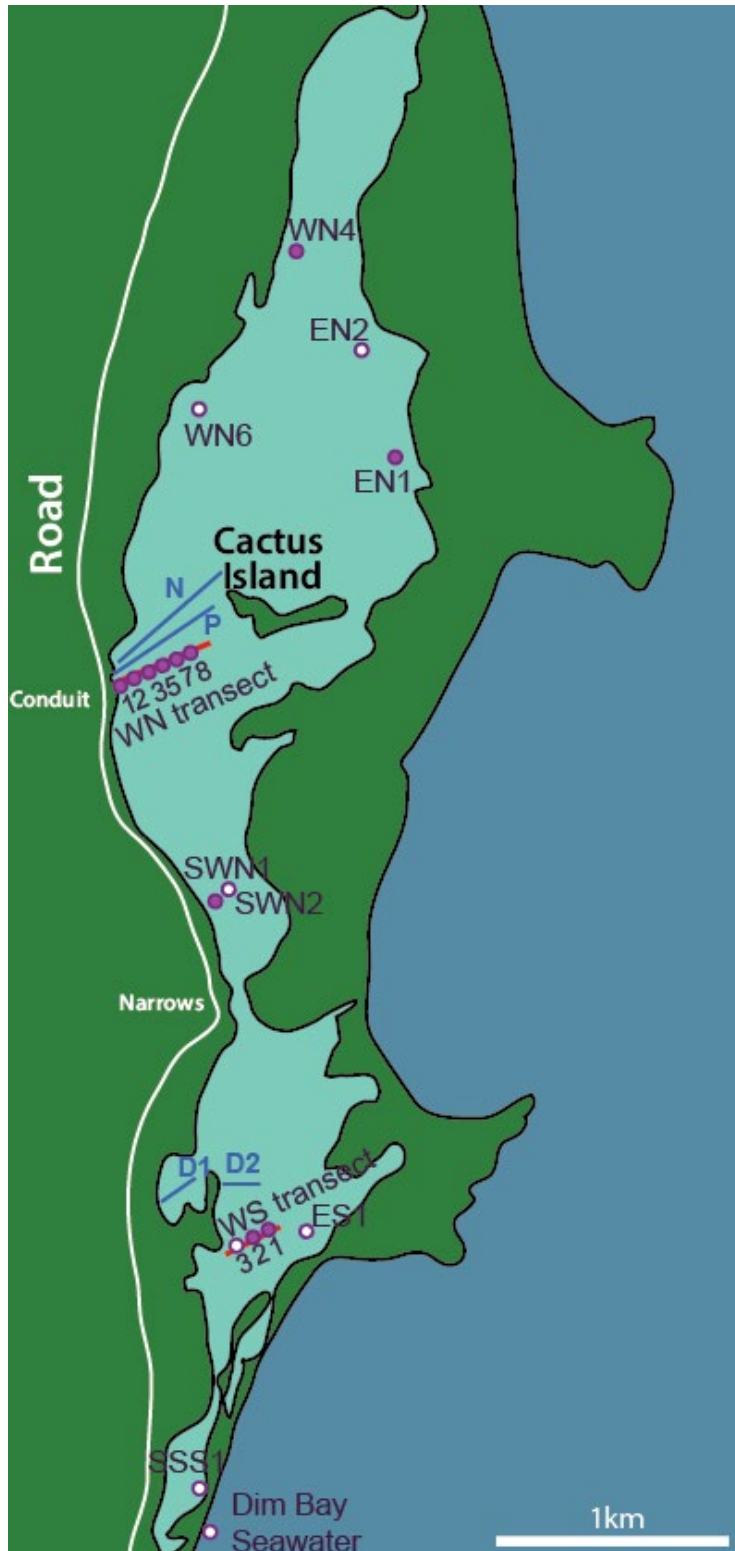


Figure 2-3 Map of Storr's Lake showing sampling locations for waters (open circles) and waters and microbialites (filled circles). Modified from Li, 2017.

Chapter 3. Previous Research on Storr's Lake Microbialites

Microbialite Morphologies and Distribution

Historically, the average Storr's Lake microbialite growth rate was determined to be 16 cm per 1,000 years (Paull et al., 1992). The base of the oldest microbialite dated in the lake was 2310 ± 70 ^{14}C years before present and is thought to be indicative of the beginning of microbialite growth in the lake (Neumann et al., 1989; Paull et al., 1992). Microscopy on Storr's Lake microbialites indicates precipitation of carbonate within the microbial mats and very little sediment trapping (Dupraz et al., 2013; Paul et al., 2016; Li, 2017). This is in contrast to other Bahamian microbialites which trap large quantities of sand (Neumann et al., 1989; Reid et al., 2011). Within Storr's Lake, various microbialite morphologies grow at different localities: water depth, lake level fluctuations, and high turbidity have been implicated as the primary morphological controls (Mann and Nelson, 1989; Neumann et al., 1989; Dupraz et al., 2011). These microbialites have micritic laminations and numerous micro-unconformities with an unknown amount of time lost between accretion and dissolution periods (Neumann et al., 1989; Paull et al., 1992; Li, 2017). Li (2017) found sparse ooids and ostracods within the dense micritic laminae using light microscopy (Figure 3-1).

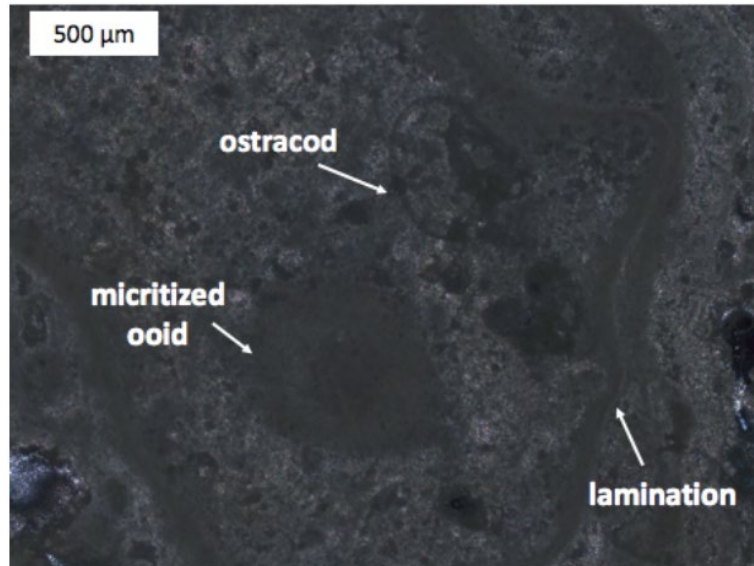


Figure 3-1 Ooids and ostracods in thin section from dense micritic lamina of WS1-6 (Li, 2017).

Paul et al. (2016) characterized the changing microbialite morphologies (Figure 3-2) along the “P” transect within the northern sector of the lake shown above in Figure 2-1. They identified five types of microbialites and a “Cheesecake mat,” which is non-lithified layered organic and carbonate ooze covering the central bottom of the lake (Paul et al., 2016). I will be using the Paul et al. (2016) morphology descriptions to categorize the microbialites collected from Storr’s Lake in this study because they are concise and combine previous morphological descriptions well. Representative samples of their morphology descriptions are shown in Figure 3-3.

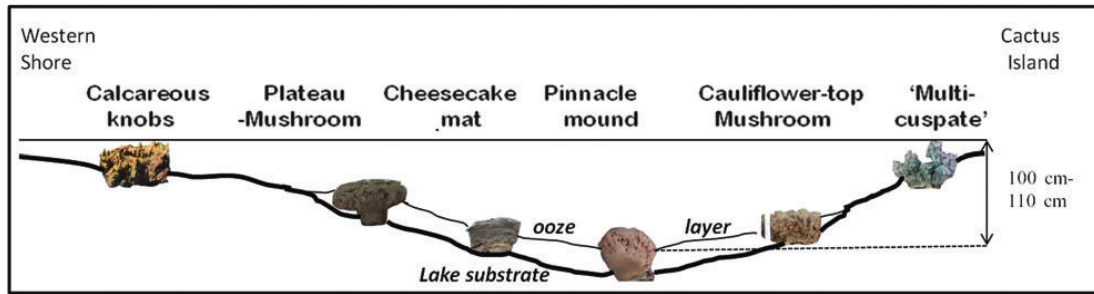


Figure 3-2 Northern Transect of Microbialite Morphologies from Paul et al. (2016)

In the shallow water on the western shore are calcareous knobs, which have two primary characteristics: smooth, continuous, and light colored carbonate on the upper half; darker, “fused-granular” carbonate on the lower half where the microbialite attaches to the lake bottom (Paul et al., 2016). Moving into deeper water, plateau-mushrooms have a branching network structure on their upper crust with a strongly cemented and prominent “stalk” connecting them to the lake bottom. In addition, plateau-mushrooms lack laminations on their interior and have a cloud-like structure above the stalk (Paul et al., 2016). In the deepest part of the lake are pinnacle mounds, with a continuous surficial crust, a thrombolitic zone below that, followed by compacted stromatolitic millimeter scale layering at the bottom of the microbialite (Paul et al., 2016).

Moving east, cauliflower-top mushrooms have bulging and knobby tops with continuous centimeter scale laminations throughout the central portion. Some of the laminations have thrombolitic nodes and where the microbialite connects to the lake floor is a fragile and fissile “stalk” (Paul et al., 2016). Closest to the shore of Cactus Island at similar depths to the calcareous knobs are multi-cuscate microbialites, which are well

lithified with sharp, distinguished protrusions and some layering within the bottom ~2 cm (Paul et al., 2016).

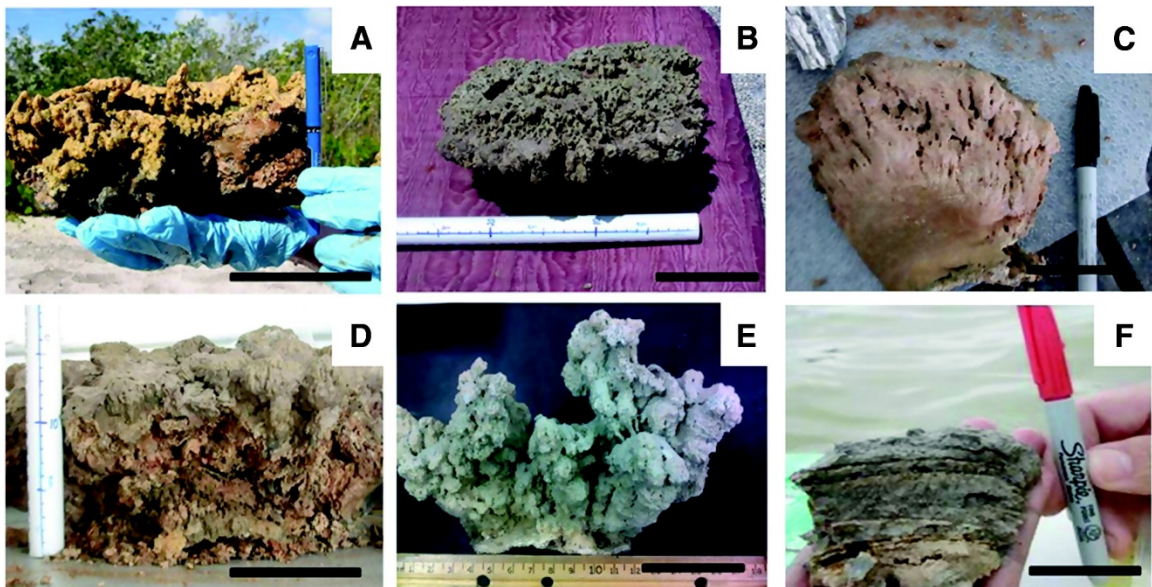


Figure 3-3 Representative images of microbialite morphologies from Storr's Lake (Paul et al., 2016). (A) Calcareous knob microbialite (bar: 12cm); (B) top view of the plateau-mushroom microbialite (bar: 10cm); (C) Pinnacle mound microbialite (bar: 7.5cm); (D) Cauliflower-top mushroom microbialite (bar: 10cm); (E) Multi cusped microbialite (bar: 5cm); (F) Cheesecake mat profile view (bar: 7.5cm).

Microbial Mat Communities and Relationships to Calcification

The high turbidity rapidly attenuates sunlight and likely limits cyanobacteria activity on the microbialites themselves (Paul et al., 2016). Instead, sulfur cycling through sulfate reducing bacteria (SRB) has been linked to calcification within the Storr's Lake microbial mats, similar to microbial mats in Big Pond, Eleuthera, Bahamas (Glunk et al., 2011; Dupraz et al., 2013). The SRB consumes organic carbon produced by

photosynthesizing microbes to produce inorganic carbon which then increases the local alkalinity and promotes calcification (equation 1-2) (Dupraz and Visscher, 2005). This so-called alkalinity engine is illustrated in Figure 1-4 and is influenced by other metabolic reactions besides sulfate reduction, including anoxygenic photosynthesis, aerobic heterotrophy, sulfide oxidization, and fermentation (Dupraz et al., 2009, 2011). Within Storr's microbialites, given the microbial community present, anoxygenic photosynthesis is also inferred to induce calcification (Paul et al., 2016).

Paul et al. (2016) performed 16S rRNA gene sequencing of the microbes present within the mats they sampled and used a jackknifed UPGMA clustering method to make a dendrogram showing evolutionary distance between microbial mat communities. Additionally, the relative abundance of 12 major bacterial taxa were identified within the microbialites studied and a large amount of unclassified bacteria were detected (Paul et al., 2016; Figure 3-4). The primary photosynthetic phyla were Chloroflexi (green, nonsulfur) and Gammaproteobacteria (purple, sulfur) (Paul et al., 2016). Even though cyanobacteria were not the primary bacterial genus (~0.01-3.2%), they are much larger than the other microbes present and can still play a large part in fabric formation (Paul et al., 2016).

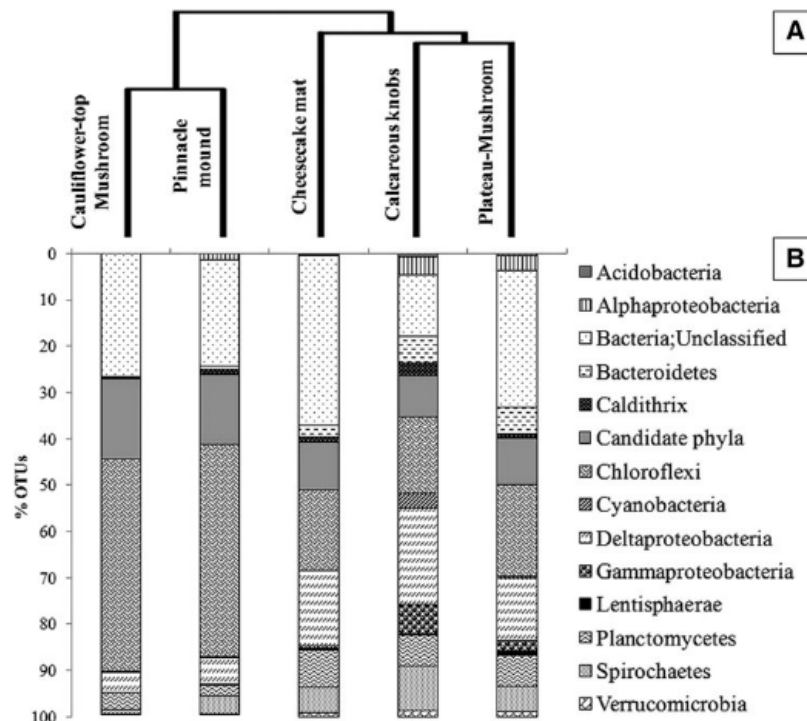


Figure 3-4 (A) Dendrogram and (B) relative bacterial abundance plot from Paul et al. (2016).

Dupraz et al. (2013) interpreted the fabric of Storr's Lake microbialites as two successive stages of filamentous cyanobacteria alternating between being perpendicular and parallel to the laminae surface. This hypothesized cycling of mat bacteria is similar to that likely occurring in the open marine Bahamian stromatolites, however, the open marine stromatolites have well developed laminations, more oxygenic photosynthetic activity, and trap large quantities of sediment (Dupraz et al., 2011, 2013). In Storr's Lake, calcification is most likely induced by degradation of photosynthetically produced EOM and heterotrophic respiration (SRB), releasing previously inhibited Ca^{2+} and Mg^{2+} which then precipitate as high-Mg calcite (HMC) (Dupraz et al., 2013; Figure 1-7).

Mineralogy of Storr's Lake Microbialites

Studies of Storr's Lake microbialites discovered aragonite using x-ray diffraction (XRD), but the origin of the aragonite is as yet unclear (Paul et al., 2016; Li, 2017). Likely, the aragonite is either a primary precipitate within the microbial mat or is a secondary precipitate produced through early diagenetic and/or recrystallization processes. Li (2017) suggests a phase transformation process, where aragonite crystallizes from within the HMC crystals (Greer et al., 2015), to describe the transition from HMC to aragonite seen in Storr's Lake microbialites. In this process, first the microenvironments of the outer microbial mat favor the precipitation of metastable HMC, due to a low Mg/Ca ratio, which is the result of the preferential binding of Mg^{2+} to EOM and sulfate (Greer et al., 2015; Li, 2017). Then, deeper in the microbialite, heterotrophic degradation releases Mg^{2+} and increases the Mg/Ca ratio to favor aragonite recrystallization from HMC (Greer et al., 2015; Li, 2017). Concentrations of Mg^{2+} greater than 10 mmol/L have been shown to precipitate aragonite at room temperature (Arp et al., 2001). Altering the local concentrations of ions to precipitate a metastable form that then transitions to a more stable crystal is quite similar to the mechanism used to precipitate bones, which differs in the genetic determination of structure and active ion pumping within organisms compared to the microbes forming microbialites (e.g., Beniash, 2011).

Carbon, Oxygen, and Magnesium Stable Isotopes

Carbon (C) stable isotopic analyses of the laminations in the Storr's Lake microbialites and their surrounding lake water suggest both photosynthesis and EOM

degradation are occurring during lithification (Dupraz et al., 2013; Li, 2017; Figure 3-5). New data by Li (2017) does not show the relationship between the C isotopes for the top and the bottom of the microbialites that Dupraz et al. (2013) reports (Figure 3-5). However, the lack of a relationship is congruent with data from Paull et al. (1992) (not shown). Oddly, Dupraz et al. (2013) found no evaporitic character in the $\delta^{18}\text{O}$ value for the lake water and the stromatolites, in contrast to Li (2017) and Paull et al. (1992). These differences could be due to the different morphologies studied and their locations in Storr's Lake. Dupraz et al. (2013) examined nearshore microbialites from the southern sector of the lake, whereas Paull et al. (1992) studied northern sector microbialites, and Li (2017) examined northern and southern sector deeper water microbialites.

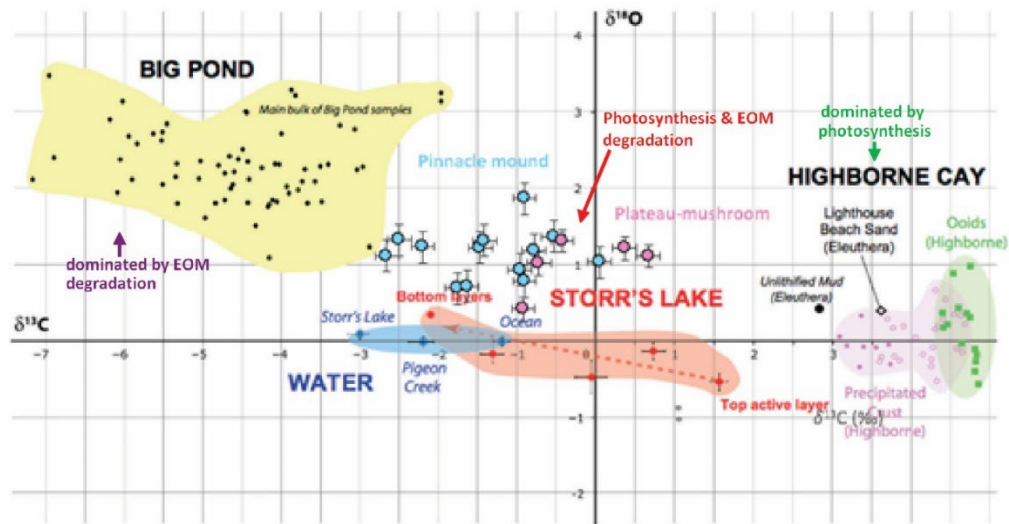


Figure 3-5 Cross plot of $\delta^{18}\text{O}$ and $\delta^{13}\text{C}$ values from microbialites (Dupraz et al., 2013) with data from Li (2017) represented by the large pink and blue dots. Each sector represents different biological processes inducing the carbonate precipitation.

The primary influence of the stable Mg isotopic composition ($\delta^{26}\text{Mg}$) of Storr's Lake was previously determined to be seawater (Li, 2017). Additionally, $\delta^{26}\text{Mg}$ is spatially homogeneous in Storr's Lake (Li, 2017). The Mg isotopes measured in two microbialites from Storr's Lake co-varied with mineralogy and Sr content, but not C or O isotopes (Li, 2017). Due to differences in the bond energy (equilibrium fractionation), it is expected that aragonite will be more enriched in the heavier isotopes compared to calcite (Finch and Allison, 2008; Wombacher et al., 2011). In a comparison of the microbialite and lake water $\delta^{26}\text{Mg}$, the difference between the carbonate and the lake water was consistent with published values for biogenic HMC and abiogenic aragonite (Li, 2017). This is consistent with biologically influenced calcification (organomineralization) and the transformation process of HMC to aragonite described above (Li, 2017). However, this may not be a unique interpretation of the data.

Chapter 4. Methodology

Microbialite Subsample Collection and Preparation

Subsamples from each of nine microbialites, except two previously analyzed (Li, 2017), were collected for analysis at 3-5 cm spacing or from the exterior and interior of the microbialite as inferred from field photos and morphology. Gastropod shells found in some of the sample interiors were not included in analysis, because the characterization of microbial mat precipitated carbonate was the goal. Microbialites WN8, WN5, WN7, and SWN2 were cut in half vertically using a cleaned hack saw. The blade was rinsed with ultrapure water and wiped down in between samples. Subsamples were collected with clean tweezers, and a knife was used in some cases to score the surface. Enough of each subsample was collected for X-ray diffraction (~0.2 g) and for digestion and subsequent elemental and isotopic analyses (6 mg). The location for each subsample within each microbialite is shown in Appendix B.

A clean mortar and pestle gently, but thoroughly, crushed each sample. The powder was transferred to an acid cleaned 15 mL centrifuge tube and vortexed for up to 2 minutes with 2-7 mL of ultrapure water, until the whole sample was suspended, to remove soluble salts and low-density organics. The samples were then centrifuged (for 10 minutes at 5000 rpm) and carefully decanted. Each sample was rinsed thrice with ultrapure water following the above method before being dried overnight at 55°C. Dried

samples were ground again and homogenized using the mortar and pestle. Separate aliquots of the powdered and washed samples were then used for XRD and elemental and isotope analysis.

X-Ray Diffraction Methodology

Subsamples were powdered again if necessary, before mounting onto zero background sample holder disks: silicon crystal disk with diameter 32 mm and thickness 2 mm; one side has a 0.2 mm deep cavity with diameter 15 mm (Malvern Panalytical product #943 018 17321). Powders were transferred to the cavity with a metal spatula and leveled by pressing with a clean glass slide. The glass slide, spatula, and disc were wiped with isopropyl alcohol between analyses. The samples were then analyzed for bulk mineralogy using the Malvern PANalytical X-Pert Pro X-ray diffractometer at the Subsurface Energy Materials Characterization and Analysis Laboratory (SEMCAL), School of Earth Sciences, The Ohio State University. Scans were acquired using $\text{CuK}\alpha$ radiation (tube voltage and current 45 keV, 40 mA) from 4 to 70 degrees 2-theta, 0.02 degree 2-theta step size, and a PANalytical high speed X'celerator detector. The HighScore Plus software and PDF 4+ mineral database were used for mineral identification and Rietveld quantitative analysis was used to determine the weight percent of mineral phases.

For phase identification, the HighScore Plus software was used to search for matches within PDF 4+ mineral database. After the background (Pseudo-Voigt) was established and all peaks selected, the software searched for matches and from the

matching patterns I chose the most reasonable one(s). Reasonable here means the reference phase for the pattern had not been drastically altered in anyway (i.e., from being heated) and that the largest peaks matched with the experimental pattern. For high-Mg calcite, a consistent pattern was utilized across all the samples with the chemical formula $\text{Ca}_{0.9}\text{Mg}_{0.1}(\text{CO}_3)$ (pattern number: 04-008-8067) (Althoff, 1977). Two primary matches were used for the aragonite phase: pattern numbers 01-075-9987 and 04-008-5421 (Jarosch and Heger, 1986; Pokroy et al., 2007). The former, 01-075-9987, is a biogenic phase from a mollusk shell (Pokroy et al., 2007). A manual background was utilized for phase identification and Rietveld quantitative analysis for samples containing both aragonite and high-Mg calcite, because the large high-Mg calcite peaks tended to skew the automatic background upwards and mask the smaller aragonite peaks. The manual background was selected to cut through the center of the noise and was necessary to reproduce data previously reported on two samples analyzed by Li (2017). Li (2017) measured these samples on a Shimadzu MAXima X XRD-700 X-Ray Diffractometer with a $\text{CuK}\alpha$ radiation source and a rotating sample stage in the Shimadzu Center for Environmental Forensics and Material Science at the University of Texas at Arlington and used MDI Jade 9 for mineral identification and semi-quantitative analysis.

Two powders previously analyzed by Li (2017) were run in this study on the PANalytical and Rietveld analysis performed. Both new analyses were within ± 0.4 wt% of the previous values for each mineral phase. Error on the Rietveld analysis was not quantified, because no internal standard was used. In addition, specialized equipment was not used to guarantee ideal grain size (~ 10 μm) and equality. However, the

reproducibility of values measured previously using a different instrument and software suggests high accuracy of the values measured (within ± 0.4 wt%).

Microbialite Sample Digestion

In The Ohio State University School of Earth Sciences Clean Lab, roughly 6 mg of each microbialite sub-sample was weighed into clean Teflon vials and dissolved in 1 mL 2N Teflon distilled hydrochloric acid (HCl). The vials were capped, sonicated for 30 minutes, and dried on a Teflon coated hot plate ($\sim 90^{\circ}\text{C}$) in a dedicated hood. Twice over, to ensure the removal of organic carbon from the sample, each vial was sonicated for 5 minutes with roughly 1 mL of 30% certified ACS hydrogen peroxide (H_2O_2) and then refluxed at 90°C for 30 minutes before the lids were removed and samples dried on the hot plate. After each drying step the hood and hot plate were wiped down with ultrapure water. Finally, samples were dissolved in 3 mL 2% Teflon distilled nitric acid (HNO_3) and sonicated for 10 minutes. From this point, 1 mL of each sample was diluted to 5 mL with the Teflon distilled HNO_3 and used for elemental analyses. The remaining 2 mL was used for Ca isotopic analysis and stored for future use.

Elemental Concentration Methodology

Following digestion, a dilution from each dissolved microbialite sample was analyzed on a Perkin Elmer Optima 4300 DV ICP-OES within the Trace Element Research Laboratory (TERL) at The Ohio State University to measure Mg, Sr, and Ca concentrations. Four-point calibration curves were created from three dilutions of 1000

ppm plasma standards for each element and an acid blank. Concentrations from previously measured microbialites were used as the reference range for the calibration curve. Quality control (QC) checks were used to qualify any drift that occurred over the course of the measurement and calculate the external error. Every five samples, one of each element standard and a blank were analyzed as unknowns for the QC checks. No auto-sampler was available so, each sample was measured manually. Mixed element standards were not made because the Ca plasma standard had a significant Mg blank that could impact the data. Manufacturer information for each element standard utilized are as follows:

- Magnesium ICP-MS Standard, 1000 ppm Mg in 3% HNO₃, Ricca Chemical Company, cat# MSMG1KN
- Strontium ICP Standard, 1000 ppm Sr in 3% HNO₃, Ricca Chemical Company, cat# PSR1KN
- Calcium, 1000 µg/mL Ca in 2% HNO₃, for ICP, SPEX CertiPrep, cat# PLCA2-2X.

Multiple wavelengths were measured for each element including axial measurements, but only one wavelength is reported for each element as discussed here. For Sr, the axial measurement of wavelength 460.733 is reported, because the relative standard deviation (RSD) of the QC checks was the lower (RSD=5.61%) and the calibration curve had a better correlation coefficient ($R^2= 0.99996$ calculated from a linear trend line in Excel) than the other wavelengths measured. For each Sr sample

measurement, the RSD of the QC checks (RSD=5.61%) was multiplied by the reported concentration to determine the error of the sample value.

For Mg measurements, the wavelength 280.271 is reported because it had the best correlation coefficient for the calibration curve ($R^2=0.9998$ calculated from a linear trend line in Excel) and the smallest amount of drift in the QC checks (less than 1.6 ppm). Error is reported the same as for the Sr measurements above (Mg 280.271 RSD=6.48%).

For Ca, the wavelength 315.887 is reported because it had the lowest drift in the 100 ppm standard QC checks (less than 11.2 ppm) and the best correlation coefficient ($R^2=0.9979$ as calculated from a linear trend line in Excel) for the calibration curve. Part way through analysis the QC standard for Ca was switched from 150 ppm to 100 ppm, so the relative error for each sample was calculated slightly differently from Mg and Sr. The relative standard deviation of the difference between the measured and reported values for the Ca QC checks was multiplied by each measured sample value to get the error (Ca 315.887 RSD=6.72%).

Elemental data is reported as ratios of the trace element to Ca and as mol% Mg. The errors on the elemental ratios were calculated using analytical error propagation from the errors on the ppm measurements (Harvey, 2016, chap. 4). Mol% Mg was calculated as the percent of Mg relative to the total amount of cations in the system (Mg and Ca), where Sr is assumed to be negligible. Error on mol% Mg was calculated using the same error propagation technique as used with the elemental ratios. The resultant errors were $\pm 0.01\%$ for all samples.

$^{87}\text{Sr}/^{86}\text{Sr}$ Sample Preparation and Analysis on TIMS

To separate Sr from the waters and digested carbonates, Eichrom Sr-specific resin was utilized. All sample preparations were done in the Clean Lab. Aliquots of samples equal to about 3 μg of Sr were dried down at $\sim 90^\circ\text{C}$ then dissolved in 100 μL 8N Teflon distilled HNO_3 for loading onto the column and sonicated for at least 10 minutes to ensure dissolution. The columns used were made in house through the shrinking of Teflon tubing around a mold. The columns have a volume of 100 μL and a capillary length of 22.1 mm with a diameter of 2.4 mm. After loading, each vial was rinsed with 100 μL 8N Teflon distilled HNO_3 , which was also loaded onto the column. In general, each column passed about 1 mL per hour and care was taken to prevent the resin from ever getting dry. At every change in normality or the addition of sample, the liquid reached the resin bed before the next solution was added to reservoir.

Before loading the samples, each column was removed from its storage container in 8N Teflon distilled HNO_3 and rinsed thrice with ultrapure water (MilliQ). Any air bubbles were pushed or pulled out using a pipette. Clean Eichrom Sr-Spec resin suspended in MilliQ was added to all columns including a column for a method blank and leveled out just at the reservoir bottom. Excess water was removed from the reservoir and the columns were washed with 600 μL of 0.005N distilled HNO_3 . 200 μL of 8N distilled HNO_3 conditioned the resin. The entire dissolved sample was then pipetted against the bottom side of the reservoir to minimize resin agitation and a 100 μL 8N distilled HNO_3 vial rinse was subsequently loaded. Two consecutive milliliters of 8N distilled HNO_3 washed through the column. Finally, two milliliters of 0.05N distilled

HNO₃ was loaded to release Sr from the resin. The waste vial was replaced with the Sr collection Teflon vial immediately after the 2 mL 0.05N distilled HNO₃ was added. The dilute acid drained into the resin bed and through the column for at least an extra half hour. The columns were cleaned by removing the resin to the dirty resin bottle, rinsing three times with MilliQ, and returning them to their 8N distilled HNO₃ filled storage container. A pipette was used to pull acid into the columns to ensure they were completely submerged. The laboratory protocol and checklist utilized for these columns can be found in Appendix C. The column set-up is shown in Figure 4-1.



Figure 4-1 Sr-spec columns used for purifying samples.

For Sr isotopic ($^{87}\text{Sr}/^{86}\text{Sr}$) analyses, 1 μg of Sr was removed from the purified sample (i.e., after column chemistry) to separate Teflon vials for each sample and dried down for loading onto the thermal ionization mass spectrometer (TIMS). At a clean HEPA filtered laminar flow work station in the TIMS Lab at The Ohio State University, handmade outgassed rhenium single filaments were loaded with each sample and Ta_2O_5 activator using the sandwich method and acid cleaned pipette tips. With the filament heated to 0.6A, 0.5 μL of the activator solution was placed in the center of the filament. The sample, dissolved in 1 μL of 1N distilled HNO_3 , was loaded onto the almost dry activator. The filament dried and then another 0.5 μL of the activator solution was placed on top of the sample. After reaching dryness, the filament was slowly heated to 1.8A and held there for one minute. Then the filament was carefully heated until it glowed a dull red before being immediately switched off. Filaments were then loaded on to the sample wheel, which was in turn loaded in the TIMS.

Samples were gradually heated over a 15 min period using an automatic heating method on the TIMS and the data was collected over ten blocks of 20 cycles per block. One analysis of SSI-SW lost signal after 120 cycles, so the remaining 60 cycles of erroneous data were removed to improve the accuracy and error on the final ratio. The values were normalized to the average of three analyses of NBS 987 shifted to 0.710250 for the specific wheel of each sample as suggested by Paull et al. (1995). Long term reproducibility of NBS 987 was calculated by normalizing each NBS 987 run using the normalization factor for each specific wheel, then taking two times the standard deviation of every normalized NBS 987 value since installation of the Thermo-Scientific Triton

Plus Multicollector TIMS at Ohio State in February 2018 ($\pm 0.000009 = 2SD$ of NBS 987, $n=114$, January 2020). To correct for instrumental fractionation during analysis the ratios were normalized to 8.375209 on $^{88}\text{Sr}/^{86}\text{Sr}$ and corrected for rubidium on the 87/85 mass ratio, correction value 0.386. Target signal intensity was 4V on ^{88}Sr with inter-block heating keeping the signal within 80-120% of 4V.

To examine external reproducibility of the Sr column and TIMS methods, multiple duplicates and replicates were analyzed. Both carbonate samples analyzed were replicated with two separate analyses on different TIMS sample wheels. Multiple water samples were replicated in the same way (GRC well, Conduit S, and ES1-50cm). Local seawater (SSI-SW) was replicated with two separate TIMS analyses on the same sample wheel and duplicated by preparing the water twice on separate columns analyzed on different sample wheels. Lake water (WS1-111cm) was also duplicated with separate column separations analyzed on different TIMS sample wheels. Overall, external reproducibility of the column separation and TIMS analyses is typically less than the long term external reproducibility of SRM 987 as shown in Table 4-1. WS1-111cm and SSI-SW did not reproduce as well as SRM 987, potentially due to matrix effects from the waters. The difference between duplicates of WS1-111cm was 0.000015 and the difference between three duplicates of SSI-SW ranged from 0.000003 to 0.000012.

Table 4-1 $^{87}\text{Sr}/^{86}\text{Sr}$ external reproducibility

Sample Name	$^{87}\text{Sr}/^{86}\text{Sr}$	Difference	Description
<i>GRC well</i> (<i>water</i>)	0.709172	0.000001	same column, different sample wheels
	0.709173		
<i>WSI-i</i> (<i>carbonate</i>)	0.709176	0.000003	same column, different sample wheels
	0.709179		
<i>WSI-6</i> (<i>carbonate</i>)	0.709174	0.000002	same column, different sample wheels
	0.709172		
<i>WSI-111cm</i> (<i>water</i>)	0.709155	0.000015	different column, different sample wheels
	0.709170		
<i>Conduit S</i> (<i>water</i>)	0.709170	0.000002	same column, different sample wheels
	0.709167		
<i>ESI-50cm</i> (<i>water</i>)	0.709181	0.000007	same column, different sample wheels
	0.709173		
<i>SSI-SW</i> (<i>water</i>)	0.709180	0.000009,	different column, different sample wheel
		0.000012	
		0.709171	0.000003
	0.709169		

Column Chemistry for Calcium Purification

For Ca isotopic analyses, a 7 μg Ca aliquot of each sample was mixed with an aliquot of the ^{43}Ca - ^{42}Ca double spike (equivalent to 3 μg of Ca) to achieve the target spike-sample ratio of 0.428 moles of spike per mole of sample, following the statistical testing for ideal spike-sample ratios of Lehn et al. (2013). Each spike-sample mixture was sonicated for 10 minutes to facilitate complete mixing and then dried down at ~ 90 - 120°C .

The dried mixtures were sonicated for at least 10 minutes in 75 μL 1.8N calibrated Teflon distilled hydrochloric acid (HCl) in preparation to load onto columns filled with MCI gel CK08P cation exchange resin (Mistubishi Chemical Company code

number 1-014-01; ion exchange capacity >1.8 meq/mL; mean particle size 120 μm). These columns are used to isolate the Ca fraction following the method of Griffith et al. (2008). Acid cleaned columns (6mL Teflon microcolumns; Savillex catalog number - 220-006-024-040-15) were filled with ultrapure water and air bubbles forced out with a pipette. Columns were washed with 10 mL 6N distilled HCl then at least 10 mL ultrapure water before loading the cleaned MCI gel resin in ultrapure water onto the columns. The resin bed should be leveled just above the reservoir bottom and excess water removed from the reservoir. Resin was cleaned in bulk before loading onto the columns by rinsing three times with ultrapure water, three times with 8N distilled HCl, and then with ultrapure water until the pH reached 5 or 6. Once loaded on the columns, the resin was washed once more with 3 mL of 6N HCl and then 3 mL of ultrapure water. If necessary, resin height was adjusted after the ultrapure water wash. Columns were conditioned with 2 mL of calibrated 1.8N HCl prior to loading the sample and pre-conditioned resin was used to adjust resin height if necessary.

The dissolved samples were then loaded directly onto the resin after the final drop of 1.8N HCl breached the resin bed. Each Teflon sample vial was rinsed with 1.8N HCl after loading: twice with 50 μL , twice with 100 μL , and finally once with 200 μL . After the whole sample reached the resin bed, 3 mL of 1.8N HCl washed through the column. Then 1.5 mL of 1.8N HCl was collected as the calcium fraction in clean Teflon vials (Figure 4-2). Finally, 3 mL of 6N HCl was washed through the columns and collected in separate Teflon vials as safety fractions. The acid flowed past the reservoir base for at least an extra 30 minutes. The Ca fraction for each column was chosen to prevent Sr

contamination, which interferes with ^{44}Ca measurement, because 100% recovery is not necessary on the TIMS with the double spike. The columns were calibrated by a previous graduate student with a Ca load of $\sim 20\ \mu\text{g}$ (E. Gaines, personal communication). The location of the Ca fraction was modified using her data to get minimal Sr contamination with approximately 83.5% recovery of Ca (E. Griffith, personal communication).

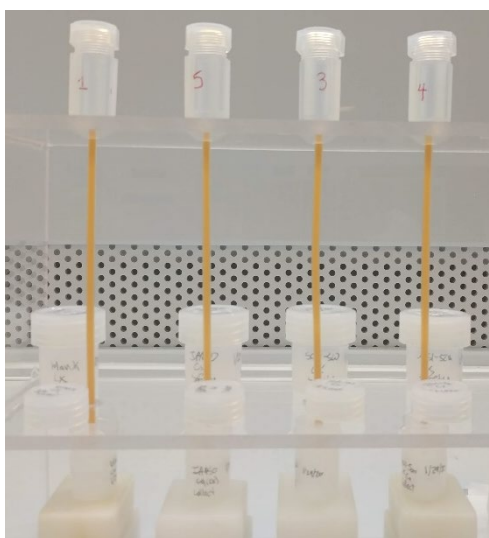


Figure 4-2 Cation exchange columns with MCI gel resin for Ca separation

Ca Isotopic Measurement on MC-ICP-MS

Before the double spike method was set up on the TIMS at The Ohio State University, select samples were analyzed using multi-collector inductively coupled plasma mass spectrometry (MC-ICP-MS). Samples were analyzed on the Thermo-Scientific Neptune Plus MC-ICP-MS at Laboratory for Isotopes and Metals in the

Environment (LIME) in the Energy and Environmental Sustainability Laboratories at Pennsylvania State University (Penn State) with the assistance of Prof. Matthew Fantle and Matthew Gonzales. Due to the nature of the MC-ICP-MS, samples underwent both Sr-spec and cation exchange columns to remove Sr and isolate Ca. Because a double spike was not used, 100% ($\pm 10\%$) recovery of Ca was required from both sets of columns or the measurement would be influenced by mass dependent fractionation occurring during sample processing. Recovery and removal of Sr was verified using the ICP-OES in the TERL at The Ohio State University. The sample processing flow is shown in Figure 4-3. Error in recovery was calculated by propagating measurement error through the calculations shown below using standard analytic error propagation techniques (Harvey, 2016).

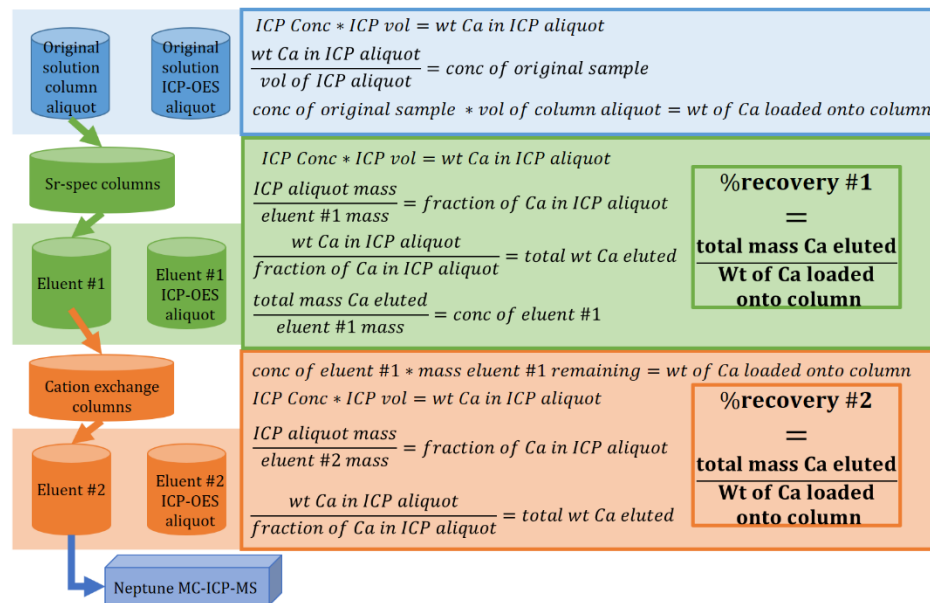


Figure 4-3 Sample processing flow and explanation of recovery calculations for the column chemistry purification of samples for MC-ICP-MS.

First, 30 μg of Ca was dried down from each sample solution (water sample or digested carbonate sample) and run through Sr-spec columns as described above. However, the first wash step after loading the sample was collected for Ca isotopes. The change in normality to pull Sr off the column was also collected for analyses of $^{87}\text{Sr}/^{86}\text{Sr}$. One third of the Ca fraction and an aliquot of the unprocessed sample were both measured on ICP-OES to verify Ca recovery and Sr separation. The same Sr and Ca elemental standards described above were used, just at lower concentrations. Column yield was carefully calculated before performing the next set of columns.

The remaining two thirds of the Ca fraction ($\sim 20 \mu\text{g}$) were dried down and run through the cation exchange columns described above to isolate Ca. However, the collection window was shifted to collect 100% of the sample Ca. After sample loading, the column was washed with 3 mL of 1.8N HCl. The next 3 mL of 1.8N HCl were collected as the complete Ca fraction. Half of the Ca fraction was run on ICP-OES to verify recovery. This left $\sim 10 \mu\text{g}$ of Ca remaining for isotopic analysis on the MC-ICP-MS. Sample yield was calculated before samples were dried down and transported to Penn State.

At Penn State, samples were prepared for analysis on the MC-ICP-MS using 2 drops of hydrofluoric acid (HF) to break down any resin residue before drying down and reconstituting the processed samples in 0.3M HNO_3 to 3ppm and refluxing for ~ 10 minutes at 80°C to ensure dissolution. All preparations were performed in the clean lab at Penn State, which is adjacent to the MC-ICP-MS laboratory space. The samples were parafilmmed and stored to be measured by Matthew Gonzales within two weeks.

Samples were analyzed following Harouaka et al. (2016) (method summarized here) and reported in delta notation, $\delta^{44/42}\text{Ca}$ SRM 915a. Each sample was introduced into the MC-ICP-MS as a dry aerosol using the Cetac Aridus II and analyzed using sample-standard bracketing with SRM 915a. To refine the beam, a Thermo Scientific sampler Jet cone and a Spectron Skimmer H cone were used. Three replicates were analyzed for each sample and 8 replicates for two standards, SRM 915a and 3109a, with signal intensities ranging from 5V to 9V on ^{44}Ca . Ratios were collected in a single block of 40 cycles with a 2 min rinse and 5 min wash in 1% HNO_3 between analyses. The data were transformed to $\delta^{44/40}\text{Ca}$ using the conversion equations provided by Heuser et al. (2016) and assuming Ca fractionation is primarily kinetic: $\delta^{44/40}\text{Ca} \approx \delta^{44/42}\text{Ca} * 2.05$. External error for each sample or standard was calculated as the standard deviation of the replicate measurements (analyses of the same solution). Alongside the samples, two standards were measured as unknowns, SRM 915b and 3019a, and 8 replicates were measured for each. The $\delta^{44/40}\text{Ca}$ and $\delta^{44/42}\text{Ca}$ relative to SRM 915a for each measured standard along with the external error (2SD) and published values are shown in Table 4-2. The one available published 3109a value was measured on the exact same instrument and using the same method (Harouaka et al., 2016).

Table 4-2 MC-ICP-MS standards compared to literature values

<i>Standard</i>	$\delta^{44/42}\text{Ca}$ (‰, rel. to 915a)	External 2SD (‰)	n	Instrument
<i>915b (this study)</i>	0.28	0.03	8	Neptune at Penn State
<i>915b (Harouaka et al. 2016)</i>	0.34	0.06	15	Neptune at Penn State
<i>915b (Hindshaw et al., 2011)</i>	0.35	0.02	79	TIMS
<i>915b (Morgan et al., 2011)</i>	0.30	0.12	47	Neptune
<i>3109a (this study)</i>	0.31	0.02	8	Neptune at Penn State
<i>3109a (Harouaka et al., 2016)</i>	0.42	NA	1	Neptune at Penn State

Compared to published values, SRM 915b is a bit lower than expected but is still within error for measurements made on the MC-ICP-MS (Morgan et al., 2011; Harouaka et al., 2016). However, SRM 915b is outside the margin of error for the published value from TIMS (Hindshaw et al., 2011). The different values on each instrument could be due to differences in the methods, data processing, and/or the non-trivial amount of Sr in SRM 915b (Fantle and Tipper, 2014).

Ca Isotopic Measurement on TIMS

For Thermo Fischer Scientific Triton Plus TIMS Ca isotopic analyses the entire cation exchange column eluent (~10 μg Ca) was dried down with 5 μL of 3.2N ultrapure phosphoric acid (ULTREX II Ultrapure Reagent, manufacturer J.T. Baker; Fischer Scientific catalog number - 02-003-606). Samples were loaded onto tantalum (Ta) single filaments that I manufactured in house using Ta ribbon (0.001" x 0.030") from The Rembar Company. The samples were dissolved in 1 μL 1.8N distilled HCl and loaded

onto the outgassed filaments at 0.8 A in a clean HEPA filtered laminar flow work station in the TIMS Lab at The Ohio State University. After the sample dried completely (~10 minutes), 2.5 μ L of 3.2N ultrapure phosphoric acid was loaded onto the filament and dried for 20 minutes (Skulan et al., 1997; Fantle and Depaolo, 2007). Then, the filaments were heated slowly to 1.2 A and remained there for 1 minute. Very slowly the current was increased until the filaments glowed a dull red (around 2.2 A) and then the current was immediately shut off.

Due to the variability of Ca evaporation and ionization, the filament heating method shown in Table 4-3 was devised as a manual heating method that generally works for Ca loads of 10 μ g. This heating method is for heating samples/standards to be run on the TIMS using the sample preparation method described above. Due to the variability of Ca ionization, I found that changes in the loading method generally required changes to the heating method. The 30 second pauses were used as needed. If it took an increase of less than 12°C to reach the next target signal, a pause was not needed. The pauses were also useful for keeping an eye on how the filament responded to the heating. The goal was for the signal to be slowly increasing and to carefully jump the same slope up to the next target voltage.

To begin, the filament was heated to 1200°C at a rate of 250 mA/min with the analyzer gate closed, this took about 10 minutes. During this time, it was important to open a previously saved low temperature tune for a similar load of Ca. The tune appeared to be quite sensitive to temperature and load, so if a saved tune was not reopened, then the sample could heat up too quickly before the system was able to perform the first tune

(at a minimum signal of 0.001 V on ^{40}Ca). Generally, the first tune of the first sample for each day of analysis was saved and used for the remainder of the day's runs. Overall, consistency in loading was very important, as was tuning regularly.

Table 4-3 Manual Heating Method for Ca on TIMS

Speed	Temp/Signal	Notes
250 mA/min	1200°C	Gate closed, open saved tune
80 mA/min	0.0015 V	Tune (save every few days)
40 mA/min	0.05 V	30 second pauses every 10°C; peak center; tune
Wait 10 minutes		If signal is not decreasing rapidly
20 mA/min	0.2 V	30 second pauses every 10°C; tune
Wait 10-15 minutes		If signal is increasing
20 mA/min	0.5 V	30 second pauses every 10°C; tune
Wait 10 minutes		
20 mA/min	1 V	30 second pauses every 10°C; tune
Wait 10 minutes		
20 mA/min	2 V	30 second pauses every 10°C; tune
Wait 10 minutes		
20 mA/min	3 V	30 second pauses every 10°C; tune
Wait 10 minutes		Start method if at 4 V
20 mA/min	4 V	30 second pauses every 10°C

At 1200°C the analyzer gate was opened, and any potassium signal was recorded, usually there was a very low Ca signal by this point. I also recorded the current of the filament. To get to the first tuning point (0.0015 V on ^{40}Ca) the filament was heated at 80

mA/min. Immediately following the tune and after noting the starting temperature, the filament was heated at 40 mA/min to 0.05 V ^{40}Ca with 30 second pauses every 10°C. This allowed the sample time to grow on its own and prevented it from heating up too quickly. During these pauses I recorded: current, temperature, signal, and whether the signal and temperature were increasing or decreasing autonomously. At 0.05 V ^{40}Ca a peak center was performed, and the signal was tuned again. If the signal was increasing at this point it was important to wait for 10 minutes, however, provided the signal was not dropping too rapidly it would generally even out and start to increase over the ten-minute wait. Next, the filament was heated at 20 mA/min to 0.2 V ^{40}Ca with the same 30 second pauses every 10°C as needed. Another tune was performed at 0.2 V ^{40}Ca and if the signal was increasing then the 10 minute wait step commenced. If the signal was not increasing, I cautiously stepped it up at the same speed another 10°C at a time until the signal was increasing, then tuned again and began the 10 minute wait.

Each subsequent signal level was reached in the same fashion with the 30 second pauses every 10°C and a 10 minute wait period including the tune. At 3 V the filament was given 10 minutes to sit and if 4 V was reached by that time the method was begun. If not, then the filament was heated at the same speed to 4 V and the method was started immediately.

After the consistent Ca load method described above was devised and implemented, some samples and standards were heated for measurement using an automatic heating method following the manual heating method previously derived (Table 4-4). This heating method was built through trial and error from the starting point

provided by Farkaš et al. (2007) and allowed for the slow automated heating of each filament without needing to painstakingly heat each filament by hand. However, the first sample every day needed to be heated manually to ensure an accurate tune file to use with the other samples. In addition, any particularly precious samples or samples with unconventional loading methods (e.g., less Ca) were also heated manually. Over the course of this study, all carbonate samples were heated manually and only waters and standards were heated using the automated sequence.

While running TIMS, the ^{40}Ca beam intensity was kept below 10V, heating to 4V before starting analysis and allowing the beam to grow on its own during blocks. Signal growth was restricted to 130% and signal loss was restricted to 90%. The signal was checked between blocks and corrected as needed by the inter-block heating commands of the Triton/Triton *Plus* software (Holmden and Bélanger, 2010). Inter-block heating was important to keep the signal from increasing or decreasing too quickly. Letting the signal increase too high, too fast seemed to destabilize the signal causing it to die off more rapidly. The cup configuration used is shown in Figure 4-4 below and provides axial symmetry for all three measurement hops used in the dynamic measurement method, which lowers the error of the analysis because it limits ion optic effects and beam clipping within the collector (Holmden and Bélanger, 2010). No measurements were recorded for ^{46}Ca or ^{48}Ca . General TIMS run parameters are shown in Table 4-5 below as modified from Lehn et al. (2013).

Table 4-4 TIMS Automatic Heating Method for Ca on TIMS

Valve	Function	Value	Slope (mA/min)	Steps	Actions
Closed	TEMC	1200°C	250	5	
Open	IONC	0.002 V	80	15	automatic focus
Open	IONC	0.009 V	40	20	
Open	WAIT	30 seconds	-	-	
Open	IONC	0.015 V	40	20	
Open	WAIT	30 second	-	-	
Open	IONC	0.025 V	40	20	
Open	WAIT	30 seconds	-	-	
Open	IONC	0.035 V	40	20	
Open	WAIT	30 seconds	-	-	
Open	IONC	0.05 V	40	20	peak center; automatic focus
Open	WAIT	10 minutes	-	-	
Open	IONC	0.15 V	20	20	
Open	WAIT	30 seconds	-	-	
Open	IONC	0.2V	20	20	automatic focus
Open	WAIT	10.5 minutes	-	-	
Open	IONC	0.4 V	20	20	
Open	WAIT	30 seconds	-	-	
Open	IONC	0.5 V	20	20	automatic focus
Open	WAIT	10.5 minutes	-	-	
Open	IONC	1 V	20	20	automatic focus
Open	WAIT	10.5 minutes	-	-	
Open	IONC	2 V	20	20	
Open	WAIT	10 minutes	-	-	
Open	IONC	3 V	20	20	automatic focus
Open	WAIT	10 minutes	-	-	
Open	IONC	4 V	20	20	END

TEMC: heating to a specific temperature goal; IONC: heating to a specific signal goal

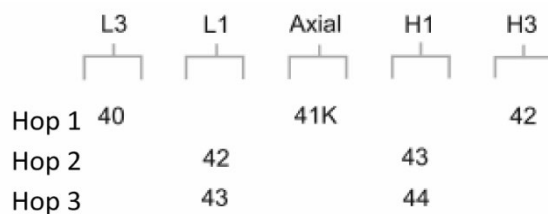


Figure 4-4 TIMS Cup Configuration and Dynamic Measurement Scheme for $\delta^{44/40}\text{Ca}$ (Holmden and Belanger, 2010)

Table 4-5 TIMS Run Parameters

METHOD PARAMETER	SETTING
Filament Assembly	Single Ta (thickness 0.001"; width 0.030")
Ca load total	10 μg
^{40}Ca ion beam intensity	4-9 V
Accelerating voltage	10 kv adjustment during run/between blocks
Resistors	$10^{11} \Omega$
Source Vacuum	5.9070E-08 mbar to 8.0139E-08 mbar during analysis with liquid nitrogen in cold trap
Analyzer Vacuum	3.4595E-09 mbar to 4.1183E-09 mbar during analysis with liquid nitrogen in cold trap
Hop 1	4.194 second integration time
Hop 2	16.776 second integration time
Hop 3	8.388 second integration time
Idle Time	4 second after each hop
Duty Cycles	100
Blocks	10 (1 block=10 duty cycles)
Gain Calibration	every 24hrs
Focus	warm-up and at start of method
peak center	warm-up and at start of method
baseline; defocused	before each block, 30 cycles at 1.05 s/cycle
Amplifier rotation	left after each block
total analysis time/sample	~3.5 hours (1.75 hrs heating; 1.75 hrs measurement)

Creation of the Double Spike

The double spike prepared for this work was mixed from two ISOFLEX carbonate single spikes, ^{42}Ca enriched and ^{43}Ca enriched, at Penn State by Matthew Gonzales. First, the ISOFLEX isotopic assays of each single spike were verified. Spikes arrived as a CaCO_3 solid powder and required dissolution. The powders were weighed multiple times to precisely determine the amount of calcium dissolved. Approximately 50 mg of each powders was dissolved in pre-weighed and cleaned PTFA bottles containing double distilled 0.5 N nitric acid and allowed to equilibrate for at least 24 prior to analysis on TIMS and later mixing. TIMS measurements (at Penn State) of both single spikes alone and each spike gravimetrically mixed with gravimetrically prepared SRM 3109a were used to calculate the absolute isotopic abundances for the single spikes. Masses and calculated concentrations are shown in Table 4-6. Following the characterization of the single spikes, the solutions were carefully mixed to a mass ratio of 0.9 (42spike/43spike). Weighed volumes of the singles spike solutions were mixed together into a pre-weighed and cleaned PTFA bottle. The volumes and concentrations of the singles spikes mixed together are shown in Table 4-7. The mixed single spikes were shaken for 24 hrs to ensure homogeneity of the double spike before approximately half was brought to Ohio State.

Table 4-6 Absolute Isotopes Abundances for ⁴³Ca and ⁴²Ca Single Spikes as Measured (TIMS) and Reported (ISOFLEX)

Calcium Isotope	⁴² Ca spike measured	⁴² Ca spike ISOFLEX assay	⁴³ Ca spike measured	⁴³ Ca spike ISOFLEX assay
⁴⁰ Ca	0.030179	0.0303	0.0695	0.0695
⁴² Ca	0.963	0.963 ± 0.003	0.00247	0.0023
⁴³ Ca	0.001066	0.001	0.869	0.869 ± 0.008
⁴⁴ Ca	0.005555	0.0055	0.058883	0.0583
⁴⁸ Ca	0.0002	0.0002	0.0009	0.0009

Table 4-7 Creation of the Double Spike

Quantity	⁴² Ca spike	⁴³ Ca spike	⁴² Ca - ⁴³ Ca double spike
<i>Single spikes</i>			
Concentration of Ca, ppm*	56.3512	49.76089	-
<i>Double spike</i>			
Weight 42 spike solution added, g*	-	-	300
Weight 43 spike solution added, g*	-	-	385
Isotopic mass ratio 42 spike/43 spike	-	-	0.900936
*0.5N nitric acid			

The mixed double spike was then characterized using the TIMS at Ohio State. To get the double spike ratios (Table 4-8), gravimetrically prepared 3109a was spiked gravimetrically and run on the TIMS at Ohio State. From the measured ratios of spiked 3109a, the Ca isotope ratios in the double spike were back calculated using the amounts of 3109a mixed with double spike and assumed ratios of SRM 3109a.

Table 4-8 Double spike Ca isotopic ratios determined in this study

Isotope ratio	Value
$^{42}\text{Ca}/^{40}\text{Ca}$	8.65519
$^{43}\text{Ca}/^{42}\text{Ca}$	1.052641
$^{44}\text{Ca}/^{43}\text{Ca}$	0.073489
$^{44}\text{Ca}/^{40}\text{Ca}$	0.669541
$^{43}\text{Ca}/^{40}\text{Ca}$	9.110812

Double Spike Subtraction Procedure

With the utilization of a double spike, a mathematical iterative procedure must be used after data collection on the TIMS to subtract the double spike from the measured ratios and calculate the delta value for standards and samples. The spike subtraction routine used at Ohio State was created in collaboration with Prof. Matthew Fantle at Penn State. He created the initial script using the program R and we modified it using experimental data to produce the most accurate results for measured Ca isotopic standards (SRM 915a and SRM915b).

To calculate the Ca isotopic ratios of each sample, the program starts with ratios measured for the double spike and ‘normal’ ratios input by the user. At Ohio State the normal ratios utilized were the natural Ca isotopic abundance ratios measured by Russell et al. (1978) because they were well quantified and have been used widely by the community in Ca double spike subtraction routines (Heuser et al., 2002; Farkaš et al., 2007a; Lehn et al., 2013; Mondal and Chakrabarti, 2018).

After the script reads the data file, it extracts the necessary measured ratios from the user determined number of cycles and calculates the average ratios. Then the iterative double spike subtraction routine, as outlined below, continues for 20 iterations before completion. In general, the calculated double spike subtracted ratios did not change after the first 10 iterations, but 20 iterations were used for a guarantee of convergence. The measured sample ratios and 'normal' ratios are used as initial values within the iterative loop. These initial values are used to calculate the ratio of tracer (i.e., double spike) to the measured sample. From there the calculated tracer ratio is used to determine the exponential mass fractionation exponent (p). The exponent p is used to calculate discrimination corrected ratios from the measured data. Discrimination corrected ratios and the 'true' double spike ratios are used to calculate the double spike subtracted $^{44}\text{Ca}/^{40}\text{Ca}$ ratio. A second exponential mass fractionation exponent (p_{40}) is calculated using the double spike subtracted $^{44}\text{Ca}/^{40}\text{Ca}$ ratio and the normal $^{44}\text{Ca}/^{40}\text{Ca}$ ratio. This p_{40} is then used to calculate double spike subtracted ratios for the other sample ratios of interest: $^{43}\text{Ca}/^{40}\text{Ca}$ and $^{42}\text{Ca}/^{40}\text{Ca}$. As the conclusion of this iteration of calculations, the measured ratios are replaced with the calculated discrimination corrected values and the sample ratios are replaced with the spike subtracted ratios. The calculation starts again with the calculation of a new p value and continues for 19 more iterations.

Following the calculation of the double spike subtracted ratios, delta values are calculated as described above using the final spike subtracted ratios and the 'normal' ratios. The spike subtraction is performed on every sample and standard measured on a sample wheel. For ease of analysis, sample names for each wheel were inputted using an

excel sheet with the number of cycles to be used for each sample and then the whole wheel was double spike subtracted at the same time. The code outputs a csv file with the delta values and other user defined variables. The delta values were then translated to delta values relative to the average measured SRM 915a on that wheel for reporting. A second isotope standard (SRM 915b) is also measured on each sample wheel to ensure the difference in measured delta values are consistent with published values during each measurement period on the TIMS (i.e., each sample wheel).

TIMS $\delta^{44/40}\text{Ca}$ Standard Reproducibility

IAPSO seawater, Dim Bay seawater, and SRM 915b were measured alongside the samples and are compared to published values in Table 4-9. Dim Bay seawater is local to San Salvador Island. Florida Bay was used as a comparison seawater, because of its proximity. Both Dim Bay and Florida Bay seawaters are within error of each other and very close together. IAPSO and SRM 915a are both within error of other published values. Small differences in $\delta^{44/40}\text{Ca}$ could be caused by different loading and sample preparation techniques, especially for seawater, which has to undergo column chemistry before analysis (Fantle and Tipper, 2014).

Replicates were measured for IAPSO and Dim Bay seawater and duplicates were measured for WS1-5cm, WS1-111cm, and Dim Bay seawater. From the observed differences between replicates and duplicates (Table 4-10), the largest (WS1-111cm) was used as the external 2SD for this study's TIMS Ca isotope analysis. This external 2SD (\pm

0.08 ‰) is similar to published external reproducibility of Ca stable isotopic analyses (Table 4-9).

Table 4-9 Literature $\delta^{44/40}\text{Ca}$ values in comparison to measured values for IAPSO, 915b and Dim Bay seawater

Standard	$\delta^{44/40}\text{Ca}$ (‰, rel. 915a)	External 2SD (‰)	n	Instrument, Location Analyzed
<i>915b (this study)</i>	0.71	0.08	9	Triton TIMS, Ohio State
<i>915b (Lehn et al., 2013)</i>	0.731	0.036	37	Triton TIMS, Saskatchewan
<i>915b (Mondal and Chakrabarti, 2018)</i>	0.73	0.08	10	TIMS, Bangalore
<i>915b (Heuser and Eisenhauer, 2008)</i>	0.72	0.04	56	TIMS, Kiel
<i>915b (Harouaka et al., 2016)</i>	0.714	0.13	15	Neptune MC-ICP-MS, Penn State
<i>915b (Hindshaw et al., 2011)</i>	0.735	0.15	79	Triton TIMS
<i>IAPSO (this study)</i>	1.89	0.08	2	Triton TIMS, Ohio State
<i>IAPSO (Farkaš et al., 2007a)</i>	1.86	0.20	5	TIMS, Ottawa and Carleton
<i>IAPSO (Farkaš et al., 2007a)</i>	1.89	0.1	20	TIMS, Kiel
<i>IAPSO (Tang et al., 2008b)</i>	1.84	0.08	13	Triton TIMS
<i>IAPSO (Hippler et al., 2003)</i>	1.88	0.04	24	TIMS, weighted mean of Bern, Kiel, and Strasbourg
<i>IAPSO (Farkaš et al., 2007b)</i>	1.86	0.1	5	TIMS, Carleton
<i>IAPSO (Lehn et al., 2013)</i>	1.865	0.040	62	Triton TIMS, Saskatchewan
<i>Dim Bay (this study)</i>	1.82	0.08	3	Triton TIMS
<i>Florida Bay (Holmden et al., 2012)</i>	1.81	0.08	2	Triton TIMS, Saskatchewan

Table 4-10 $\delta^{44/40}\text{Ca}$ external reproducibility (this study)

Sample name	$\delta^{44/40}\text{Ca}$ (‰)	Difference	Description
<i>WSI-5cm (water)</i>	1.76	0.03	different column, different sample wheel
	1.73		
<i>WSI-111cm (water)</i>	1.68	0.08	different column, different sample wheel
	1.77		
<i>Dim Bay (seawater)</i>	1.84	0.003, 0.02	different column, different sample wheel, collected in 2017
	1.84	0.02	same column, same sample wheel
	1.86		
<i>IAPSO (seawater)</i>	1.92	0.05	same column, same sample wheel
	1.87		

Chapter 5. Results

Microbialite Morphology

WN1A

From the westernmost extent of the northern transect, nearest to the brackish conduit, a small calcareous knob (nomenclature following Paul et al., 2016) was collected from a water depth of 40 cm. The whole microbialite (~8 cm long, ~5.5 cm wide, and ~3.5 cm tall) was collected as a hand sample (WN1A). WN1A has centimeter scale laminations that were visible in the field due to the color differences of the microbial mat and were still visible after the sample had been dried when looking at the interior (Figure 5-1). The upper half of the sample is largely smooth, knobby carbonate with a greenish gray color after drying. The underside is granular where it was connected to the lake bottom and has a tan color after drying.

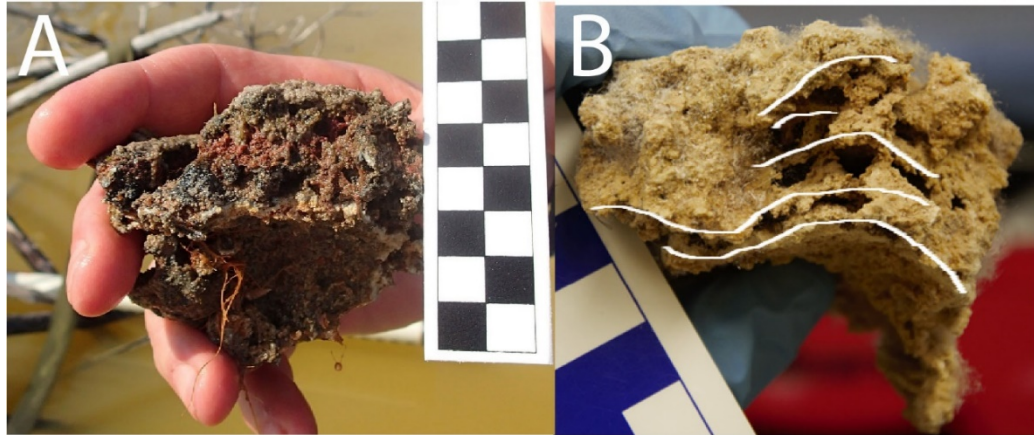


Figure 5-1 (A) Field photo of WN1A showing granular underside and microbial mat colors. (B) Lab photo of dried WN1A with laminations outlined, sample rotated $\sim 90^\circ$ clockwise from A. (scales in centimeters)

WN2

A much larger sample (WN2), characterized as a plateau mushroom (following Paul et al., 2016), was found further along the northern transect of Storr's Lake. Water depth was 82 cm to the head of the microbialite at the time of collection. The whole microbialite was massive (~ 68 cm long, ~ 65 cm wide, and ~ 27 cm tall) with a concave bottom surface. A hand sample (~ 12.5 cm long, ~ 7 cm wide, and ~ 22.5 cm tall) was cleaved off the side of the microbialite with a trowel. The top of the sample was a bright green color in the field and retained a green tinge after drying (Figure 5-2). In the field, downward from the green surface the sample transitioned to light gray then tan with salmon colored ooze. The surface of the sample had a branching networked structure and the full microbialite has a cloud like structure above a well cemented "stalk" and a smooth, strongly cemented lower exterior (Figure 5-2C). The macroscopic interior

structure is largely free of laminations, except for a few 2-3 cm wide more compact regions (Figure 5-3).

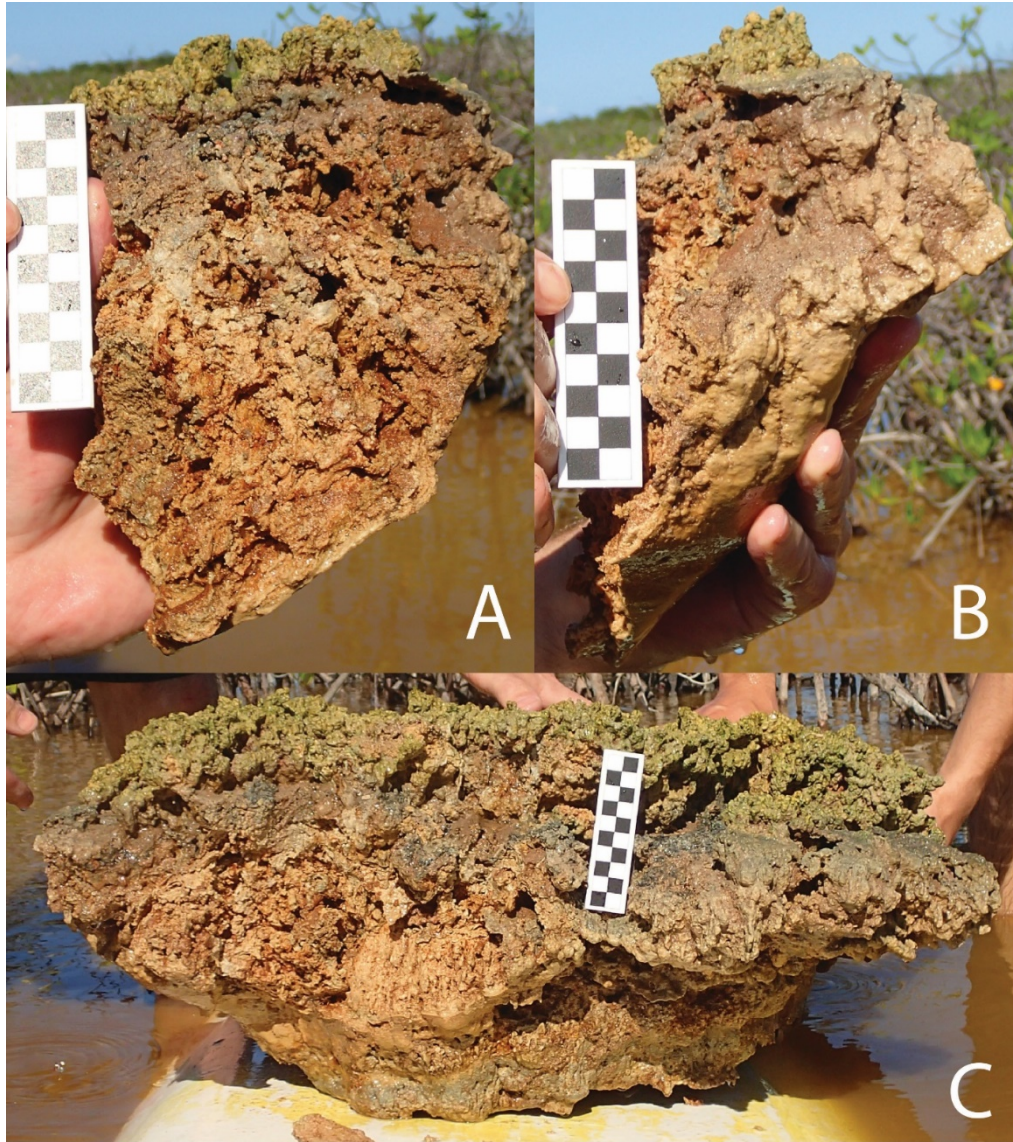


Figure 5-2 Field photos of WN2 showing fresh color and morphology. (A) Interior view of hand sample; Profile view of hand sample (B); (C) Side view of full size microbialite (scales in centimeters).

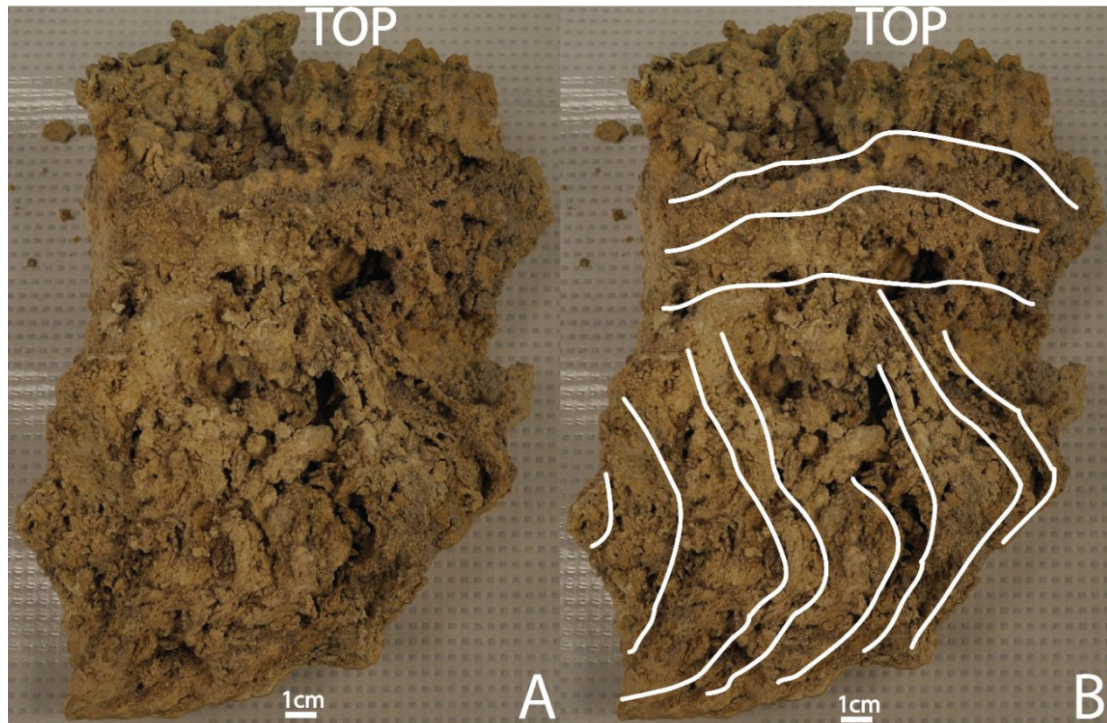


Figure 5-3 The 2 to 3cm scale laminae visible in WN2 are traced (B) and show two sets of laminae that are perpendicular to each other. (A) Clean image for comparison.

WN3

Near the halfway point of the northern transect, WN3 was collected. The morphology for WN3 is difficult to characterize, because there are limited field photos and the dried sample in storage has crumbled into unconsolidated flakes except for a fist sized hand sample (Figure 5-4). Most likely a cauliflower top mushroom (as per Paul et al., 2016), WN3 was collected from a depth of 102 cm to the head of the microbialite. The surface of the microbialite has bulging knobs and the interior had continuous friable and crumbly laminations (Figure 5-4). The whole sample had a tan color to it with salmon colored ooze on the underside (Figure 5-4A).

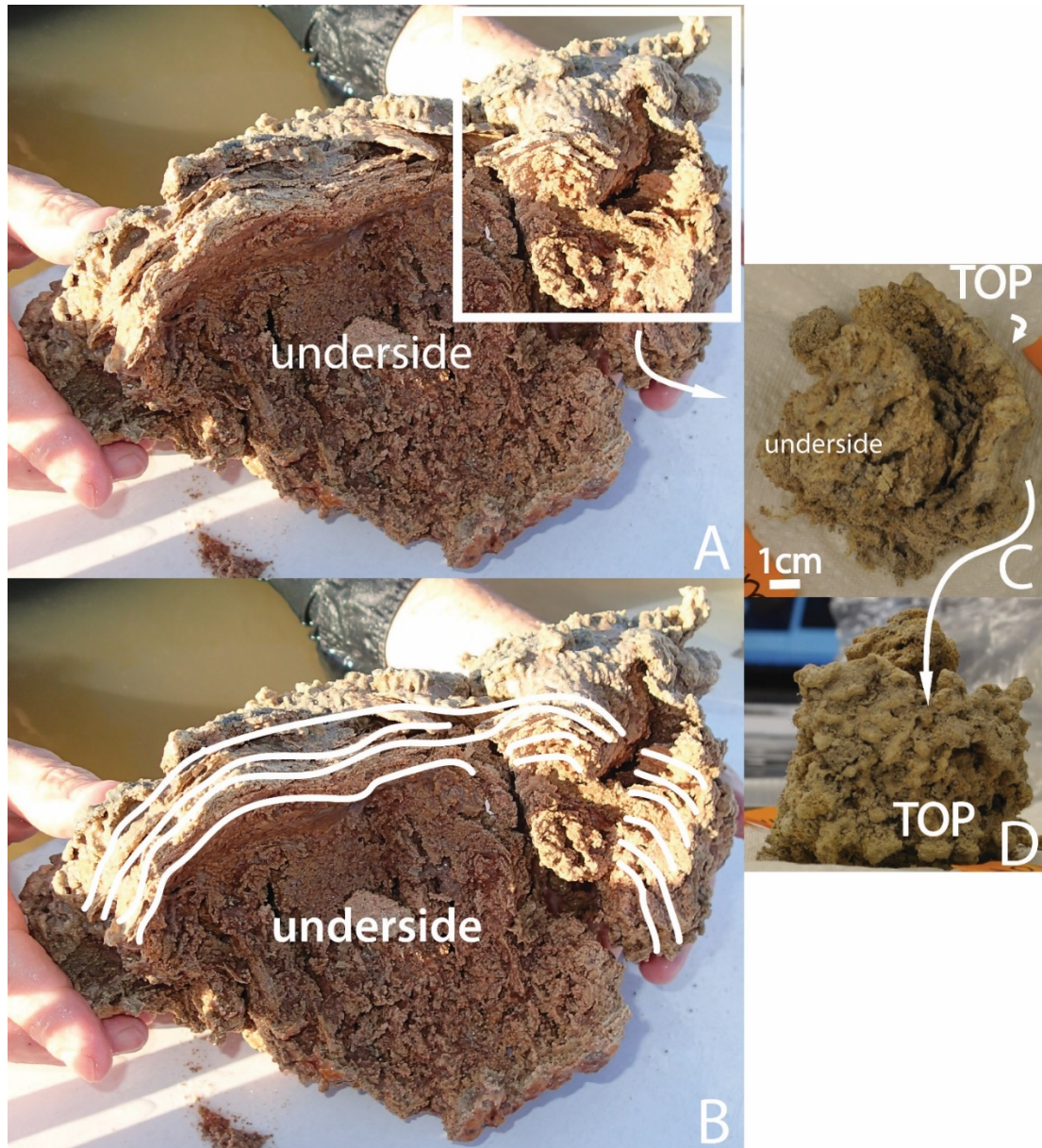


Figure 5-4 (A) Field photo of full WN3 sample with square outlining most likely location of lab sample, (B) traced millimeter scale laminations of the sample. Lab photos are inset showing the underside (D) and top view (C) of the remaining sample.

WN4

Near the northern extent of Storr's Lake, WN4 was collected from a water depth of 75 cm to the microbialite head and is the furthest north microbialite collected in this study. Classified as a multi-cusped type microbialite (following Paul et al., 2016), because of the 2-3 cm scale protrusions of well lithified carbonate and small laminations on the bottom of the microbialite. The dried sample (~5.5 cm long, ~3.5 cm wide, and ~8 cm tall) is a homogeneous tan color as shown in Figure 5-5A with the lower laminations outlined in Figure 5-5B.

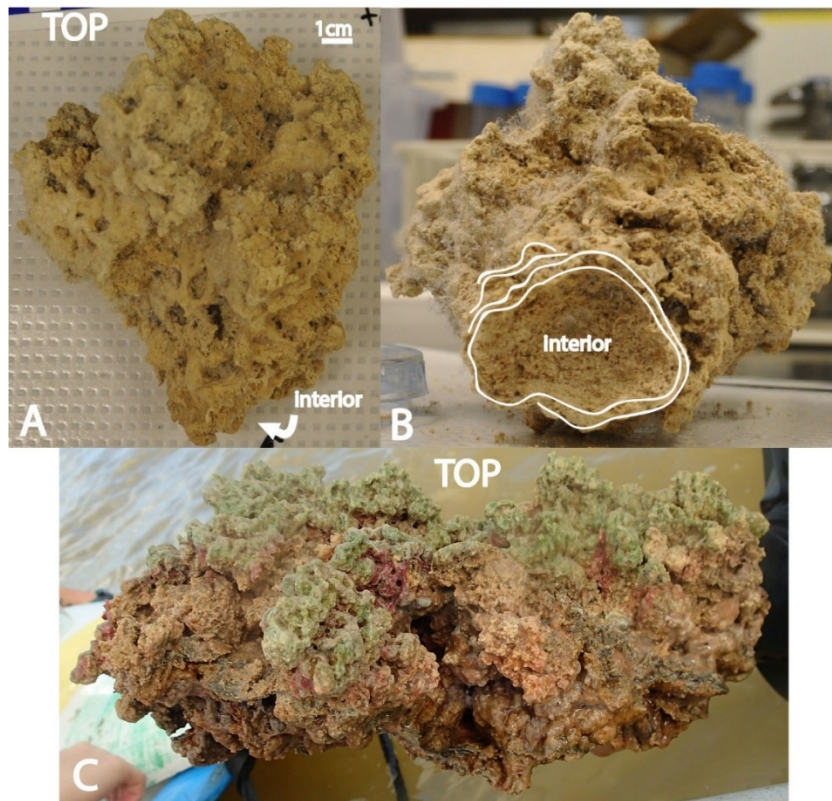


Figure 5-5 (A) WN4 dried in the lab; (B) interior centimeter scale laminations traced; (C) side view of WN4 in the field before separating into a hand sample in the field.

WN5

In the deepest part of the northern transect, WN5 (~12 cm long, ~10 cm wide, and ~7 cm tall) was collected from a water depth of roughly 167 cm to the microbialite head. The most fitting characterization (per Paul et al., 2016) is as a cauliflower top mushroom that lacks a fragile stalk (Figure 5-6A). The whole sample is a reddish-brown color with interior laminations and a knobby top. The laminations alternated between thin ~2 mm hard laminations and centimeter scale, more granular laminations (Figure 5-6C). WN5 appears to have grown upwards off a hard crust (Figure 5-6A).

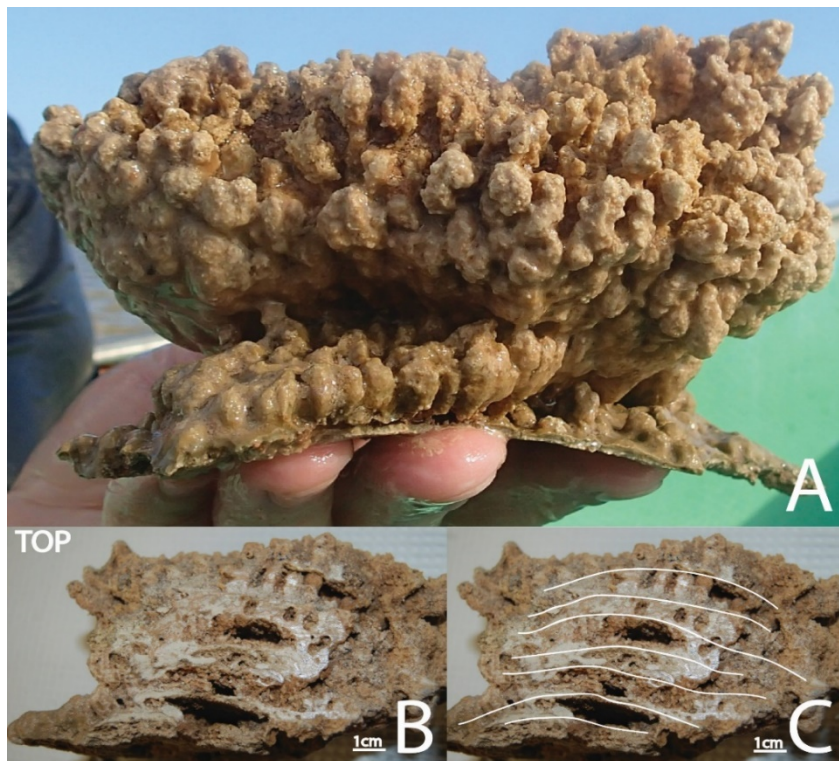


Figure 5-6 (A) Field profile photo of WN5; (B) dried half section photos of WN5 showing internal laminations; (C) traced fine laminations (~2 mm) with thicker laminations between.

WN7

Sampled from within the northern transect close to Cactus Island, WN7 is a plateau mushroom (~30 cm long, ~22 cm wide, and ~20 cm tall). The characterization follows Paul et al. (2016) and the below description paraphrases Li (2017). The largely tan colored plateau mushroom (Figure 5-7B) was collected from a water depth of 60-70 cm to the head of the microbialite. The surface of the microbialite had a branching structure and the upper 5-6 cm had no visible laminations. However, there were visible ~0.5 cm scale laminations in the bottom section of the microbialite (Figure 5-7A).

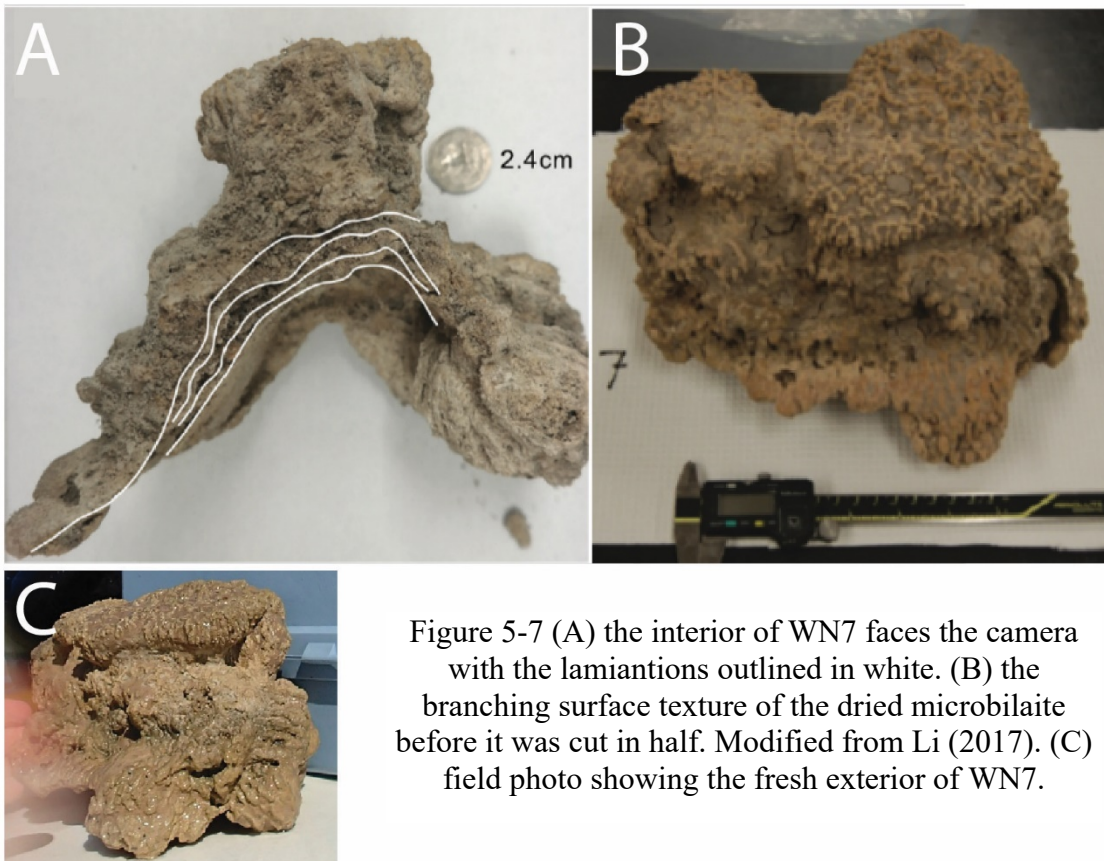


Figure 5-7 (A) the interior of WN7 faces the camera with the lamiantions outlined in white. (B) the branching surface texture of the dried microbilaite before it was cut in half. Modified from Li (2017). (C) field photo showing the fresh exterior of WN7.

WN8

Closest to Cactus Island within the northern transect, a pinnacle mound was collected from a water depth of 81 cm to the head of the microbialite (WN8, Figure 5-8). The whole microbialite was collected and the bottom crust of WN8 was laminated and friable (Figure 5-9A). WN8 is primarily a rusty brown color (dried) and the surface and exterior of the microbialite are quite knobby, which is not included in the pinnacle mound definition (Figure 5-9B). However, below the knobby surface, there is a continuous region of thrombolitic texture followed by laminations decreasing from centimeter scale to millimeter scale in the broken off bottom piece (Figure 5-9D).



Figure 5-8 Field photo of the top of WN8 (scale in centimeters).

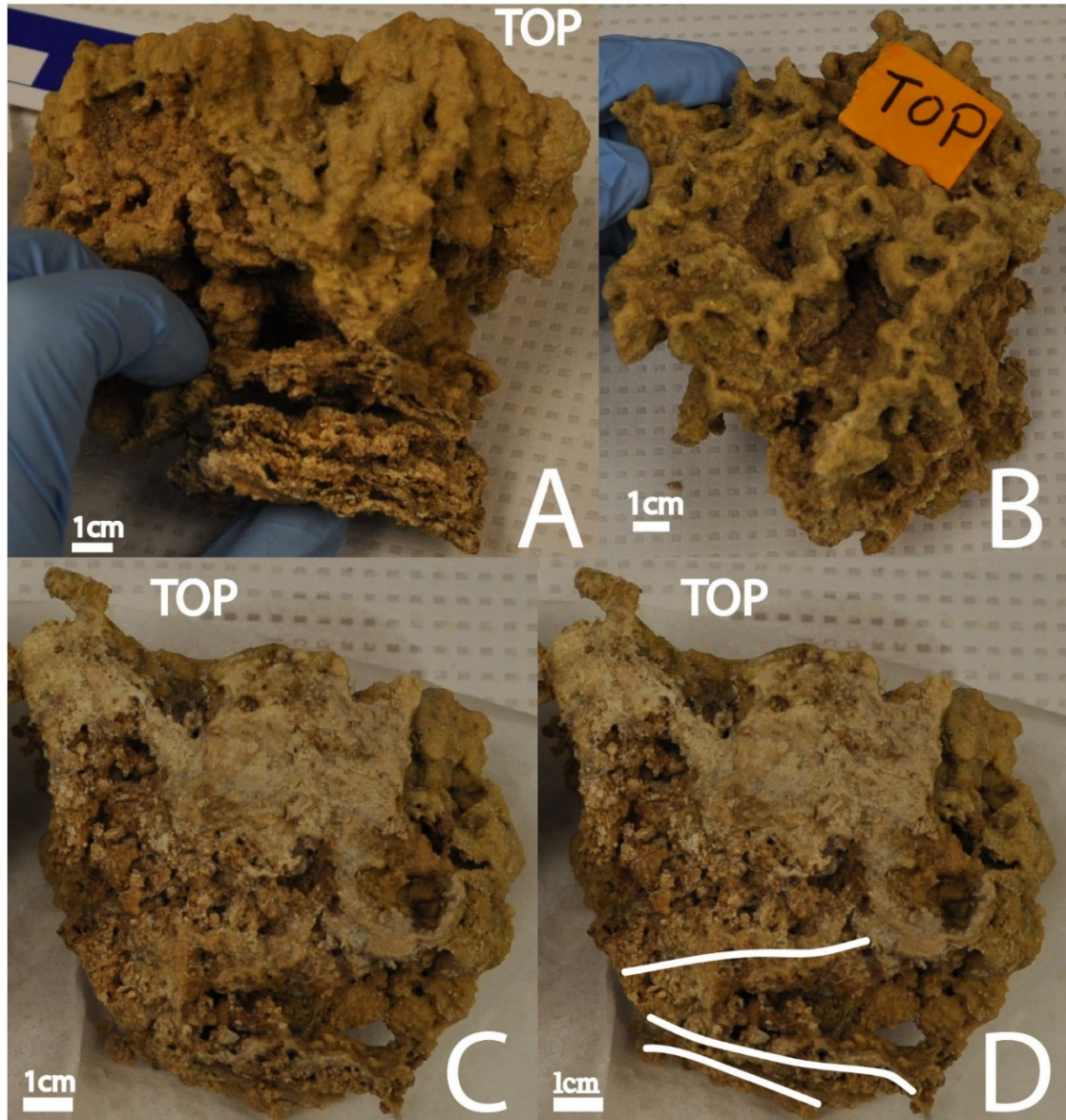


Figure 5-9 (A) Side view of WN8 full sample with bottom laminated crust held in place; (B) Top surface of full sample showing the knobby top; (C) Dried half section photo of WN8 with interior facing the camera; (D) traced laminations within the interior.

EN1

Another small calcareous knob (following Paul et al., 2016) was collected north of Cactus Island on the eastern shore of Storr's Lake from a water depth of 55 cm to the microbialite head. The sample (EN1) has the characteristic upper smooth carbonate with a lower, darker granular structure (~9 cm long, ~5 cm wide, and ~3.5 cm tall). In the field the surface of the microbialite was green that transitioned into a dark brownish gray. The bottom granular portion of the microbialite was rusty red (Figure 5-10A). After drying the sample retains a slight green tinge to the tan surface carbonate and the granular portion is a browner tan (Figure 5-10B).



Figure 5-10 (A) Field photo of EN1 (scale centimeters); (B) EN1 after drying

SWN2

At the southern end of the northern sector of Storr's Lake, another small calcareous knob (~8 cm long, ~6 cm wide, and ~7 cm tall) was collected from a water depth of roughly 40 cm. The sample (SWN2) has a smooth bulbous carbonate top layer and a granular darker color bottom layer (Figure 5-11). Shortly after sampling the surface layer retained a green tinge and the interior transitioned in color to grey and then to salmon red at the bottom (no images available).

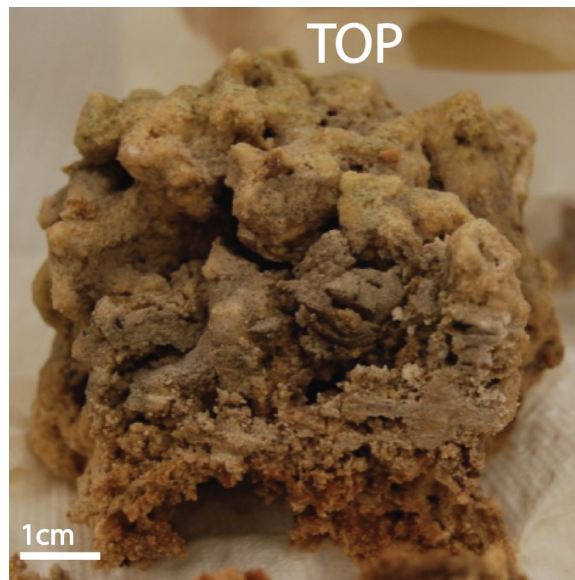


Figure 5-11 Half-sectioned hand sample of SWN2 with the interior facing the camera label bottom

WS1

At the deepest part of the southern transect and about 250 m from the western lake shore, WS1 was collected from a water depth of 111 cm to the head of the microbialite. A hand sample (~22 cm long, ~6 cm wide, and ~18 cm tall) was separated from the large microbialite head (~38 cm long, ~32 cm wide, and ~25 cm tall) (Figure 5-12B). The microbialite was previously described by Li (2017) as a pinnacle mound (following Paul et al., 2016) and that description is paraphrased here. The bulbous crust at the top of the microbialite was largely light tan with green spots. Below the 7-8 cm crust were continuous horizontal laminations on the millimeter scale (Figure 5-12A). The laminations started out as a greyish brown color and transitioned to a reddish-brown color deeper in the microbialite. Additionally, the laminations were quite friable.

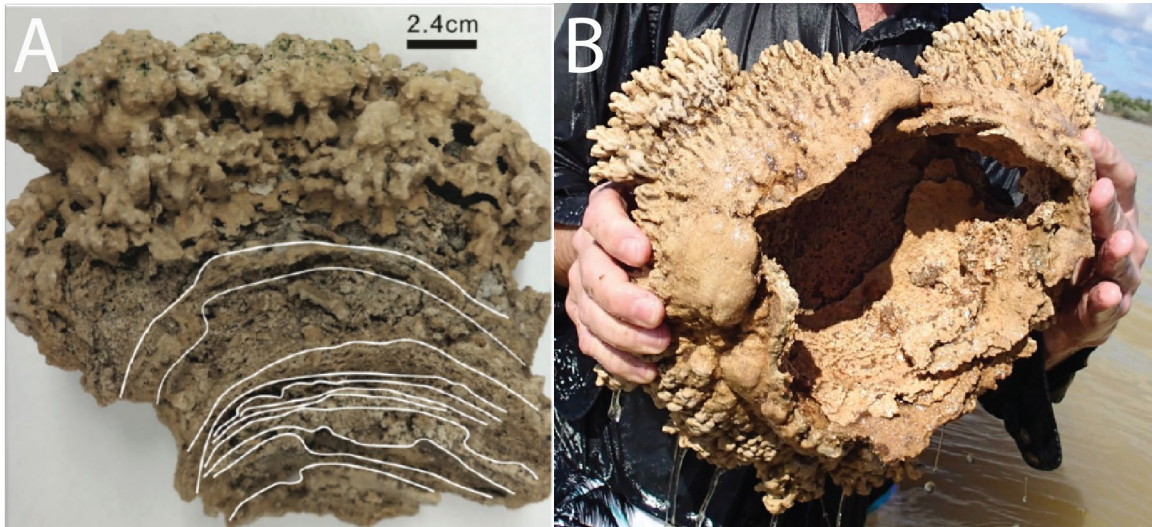


Figure 5-12 (A) the interior of WS1 faces the camera with the lamianations outlined in white. (B) The full size microbialite as it was pulled from the lake, hand sample in the man's left hand. Modified from Li (2017).

WS2

Halfway along the southern transect, but at a similar water depth to the nearest shore sample, WS2 was collected from a water depth of 46 cm to the microbialite head. The sample was characterized as a cauliflower top mushroom (following Paul et al., 2016) because of the continuous laminations throughout the sample, the more fissile bottom half, and the bulbous upper crust (Figure 5-13). The laminations alternated from well lithified thin (~2 mm) layers to thicker (~1cm) fissile and porous layers (Figure 5-13B). The top half of the sample (~6 cm long, ~5 cm wide, and ~5.5 cm tall) was green and light gray when fresh and dried to a tan-green color (Figure 5-13C, D). The bottom half of the sample (~9 cm long, ~6 cm wide, and ~8.5 cm tall) was tan and blood red when fresh and dried to a rust splattered tan (Figure 5-13C, E).

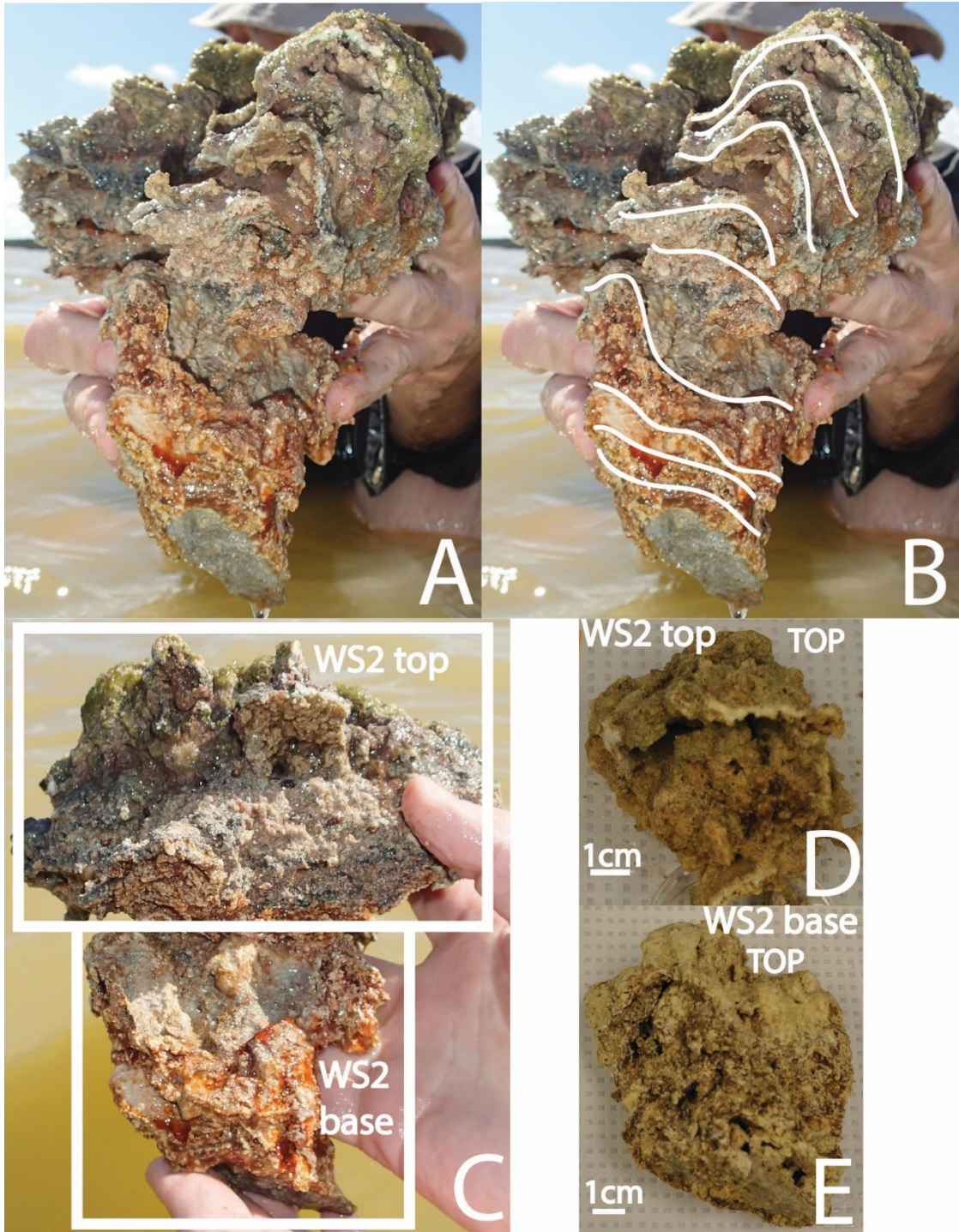


Figure 5-13 Field and lab photos of WS2 including (A) a profile view; (B) traced laminae shown in the profile view; (C) a front view with top and base outlined; dried lab photos of hand sample from the top (D) and the hand sample from the base (E).

Mineralogy of Microbialite Subsamples

Subsamples from each microbialite were analyzed for their mineralogy using XRD. Mineralogy data is shown in Table 5-1. High-Mg calcite (HMC) was the dominant mineralogy in all microbialites studied ($\text{Ca}_{0.9}\text{Mg}_{0.1}(\text{CO}_3)$, PDF 4+ mineral database pattern number: 04-008-8067). The upper surface of most microbialites, where the top could be definitively determined (all except WN3), was 100 wt% HMC. In every microbialite collected from water depths greater than 40 cm, there was also aragonite measured within the interior of the microbialite. The amount of aragonite measured ranged from 2.1 wt% to 28.3 wt%. Of the subsamples analyzed in the study, the microbialite with the most aragonite was from the deepest water depth of about 167 cm, WN5 with 28.3 wt% aragonite. The only microbialite sample measured without aragonite in any of the layers was WN1A, collected from the northern sector of Storr's Lake nearest to the western shore (near to an access point by a brackish water conduit) at a water depth of 40 cm.

Spectra from each XRD analysis are shown in Appendix A. Mineralogy data reported in Li (2017) from two microbialites (WN7 and WS1) collected at the same time as the microbialites in this study will be included in the discussion of this data. Both microbialites studied by Li (2017) had subsamples from similar depths in the north (between 61 and 140 cm) and south (111 cm) sectors of Storr's Lake with a significantly larger portion of aragonite than this study.

Table 5-1 Elemental and mineralogy data for Storr's Lake microbialites measured in this study. HMC = high magnesium calcite ($\text{Ca}_{0.9}\text{Mg}_{0.1}(\text{CO}_3)$)

Sample ID	depth to head	wt%	Molar ratio		Mol%
		Aragonite /HMC	Ca:Mg (mol/mol)	Sr:Ca (mmol/mol)	Mg (± 1)
Calcareous knob	55cm				
EN1-i		0/100	5.3 \pm 0.5	3.8 \pm 0.3	16
EN1-ii		5.6/94.4	5.5 \pm 0.5	3.7 \pm 0.3	15
Calcareous knob	~40cm				
SWN2-i		0/100	5.7 \pm 0.5	3.8 \pm 0.3	15
SWN2-ii		5.0/95.0	6.4 \pm 0.6	3.9 \pm 0.3	14
Calcareous knob	40cm				
WN1A-i		0/100	5.53 \pm 0.5	3.7 \pm 0.3	16
WN1A-ii		0/100	6.3 \pm 0.6	3.5 \pm 0.3	14
Plateau mushroom	82cm				
WN2-i		0/100	5.8 \pm 0.5	3.7 \pm 0.3	15
WN2-ii		4.1/95.9	6.3 \pm 0.6	4.2 \pm 0.4	14
WN2-iii		9.4/90.6	7.4 \pm 0.7	5.4 \pm 0.5	12
WN2-iv		0/100	6.3 \pm 0.6	3.7 \pm 0.3	14
Cauliflower top mushroom	102cm				
WN3-i		3.2/96.8	6.6 \pm 0.6	3.9 \pm 0.3	13
WN3-ii		4.8/95.2	6.4 \pm 0.6	4.2 \pm 0.4	14
Multi-cuspate	75cm				
WN4-i		0/100	6.1 \pm 0.6	3.5 \pm 0.3	14
WN4-ii		4.6/95.4	6.4 \pm 0.6	4.0 \pm 0.3	14
Cauliflower top mushroom	~167cm				
WN5-I		6.7/93.3	6.5 \pm 0.6	3.9 \pm 0.3	13
WN5-VI		28.3/71.7	9.1 \pm 0.9	8.4 \pm 0.7	10
WN5-IX		0/100	6.2 \pm 0.6	3.6 \pm 0.3	14
Pinnacle Mound	61cm				
WN8-i		0/100	5.5 \pm 0.5	3.8 \pm 0.3	15
WN8-ii		6.9/93.1	6.3 \pm 0.6	3.7 \pm 0.3	14
WN8-iii		2.1/97.9	5.9 \pm 0.5	3.7 \pm 0.3	15
Cauliflower top mushroom	46cm				
WS2-b		4.6/95.4	6.4 \pm 0.6	4.2 \pm 0.4	13
WS2-t		0/100	5.7 \pm 0.5	3.5 \pm 0.3	15

Elemental Compositions of Microbialite Subsamples

Digested carbonate subsamples from each microbialite studied were analyzed using ICP-OES for Ca, Mg, and Sr concentrations and molar ratios were calculated, Sr:Ca and Ca:Mg (Table 5-1). In addition, the mol% of Mg was calculated relative to the cumulative moles of Ca and Mg under the assumption that Sr is negligible, i.e. does not impact the mol% Mg calculated. The mol% Mg ranges from 10 to 16 mol% with the lowest value from the sample with the highest aragonite. When compared to the XRD HMC mol% Mg of 10, the ICP-OES calculated mol% Mg is quite similar and confirms the presence of HMC within these samples.

There is a significant positive linear relationship ($r^2=0.8776$, $p=1.411e-10$) between Sr:Ca and wt% aragonite (Figure 5-14A). When combined with data from Li (2017) (Figure 5-14B), there is a significant positive linear relationship ($r^2=0.949$, $p<2.2e-16$), but the slope of the line decreases. There is also a significant negative linear relationship ($r^2=0.6578$, $p=4.68e-6$) between wt% aragonite and Mg:Ca (Figure 5-15A), which continues with the addition of data from Li (2017) ($r^2=0.9803$, $p<2.2e-16$) as shown in Figure 5-15B.

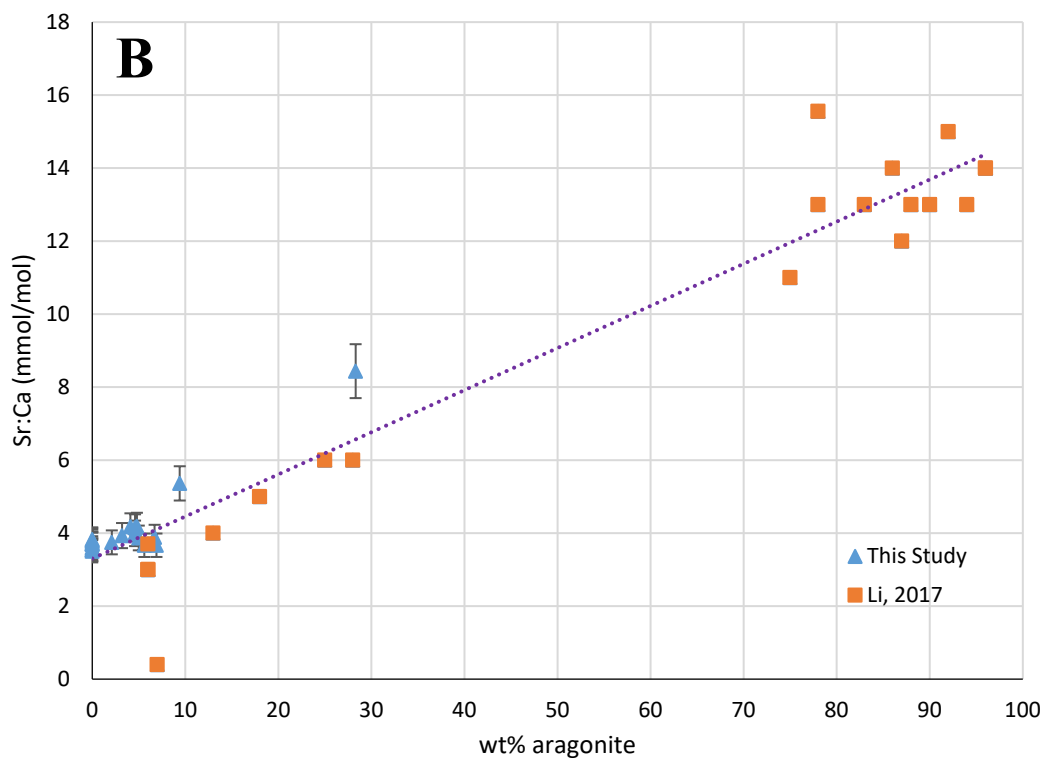
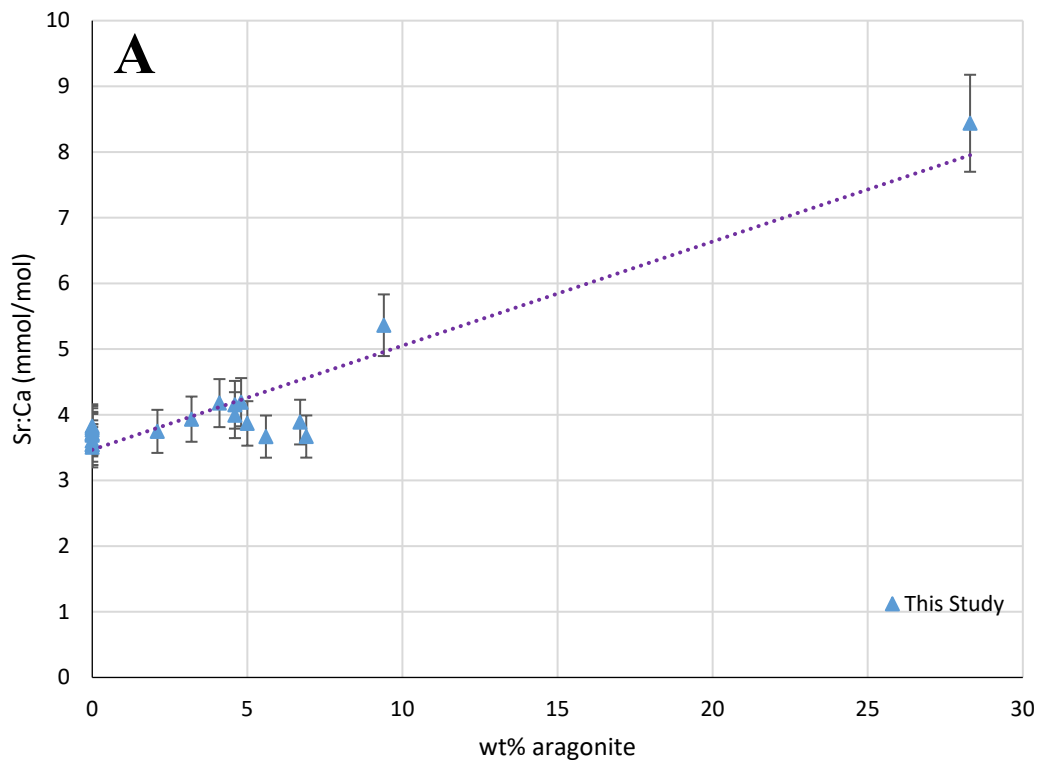


Figure 5-14 Trend lines showing (A) the positive relationship between Sr:Ca molar ratio and wt% aragonite for this study and (B) this study combined with Li (2017).

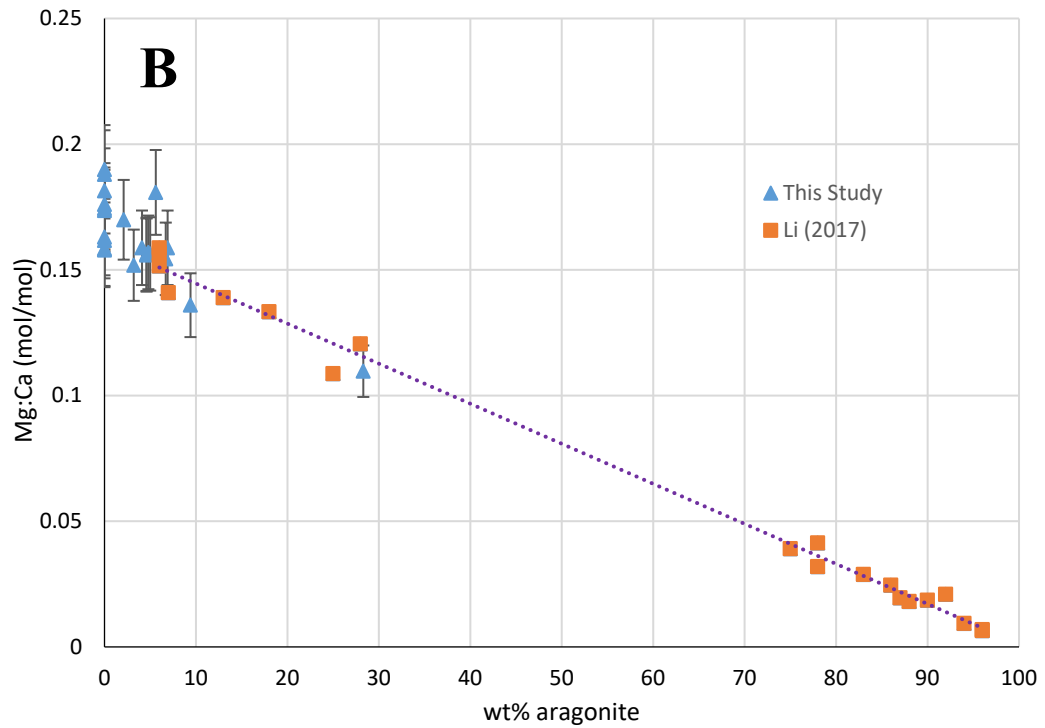
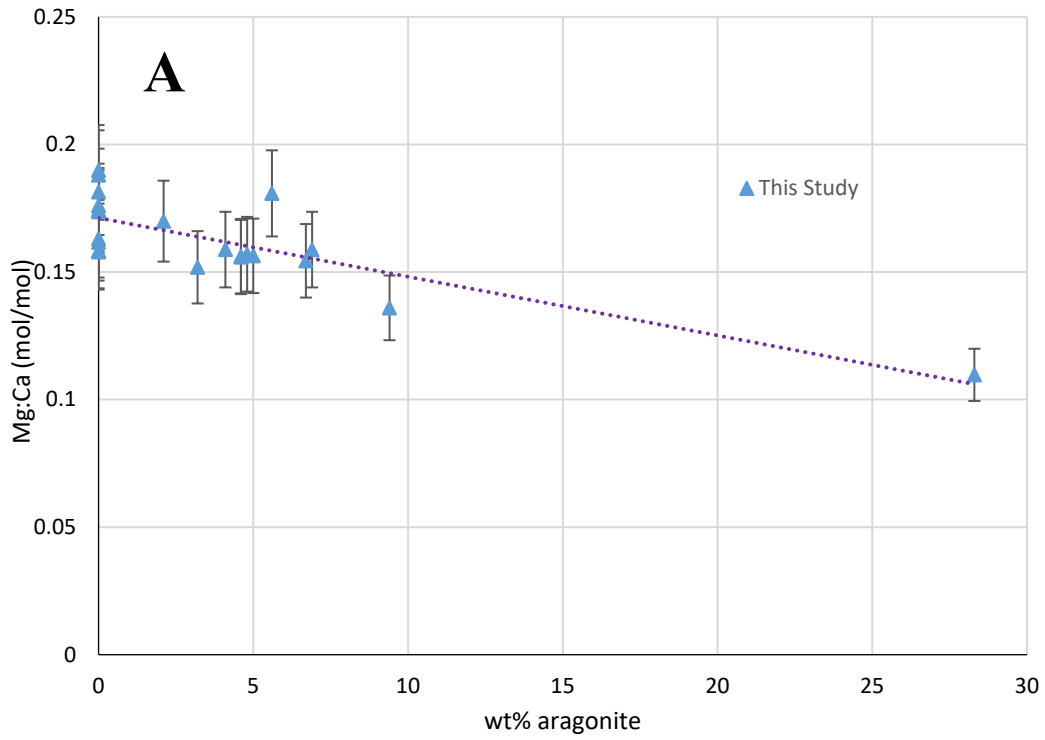


Figure 5-15 (A) Negative trend between Mg:Ca molar ratio and wt% aragonite in this study and (B) the same trend with the combined data set of this study and Li (2017).

$^{87}\text{Sr}/^{86}\text{Sr}$ of Storr's Lake Water

$^{87}\text{Sr}/^{86}\text{Sr}$ was measured for waters collected throughout Storr's Lake in addition to two microbialite subsamples from WS1. The microbialite subsamples, WS1-i and WS1-6, have the highest amount of HMC and aragonite, respectively, of the samples previously studied by Li (2017). $^{87}\text{Sr}/^{86}\text{Sr}$ values for each measured sample are shown in Table 5-2.

All replicates and duplicates of local seawater were within error of the published value, 0.709167 ± 0.000012 (Paull et al., 1995). While the variability on the seawater replicates ($2\text{SD} = \pm 0.000012$) is slightly outside the long-term variability of the SRM 987 (± 0.000009), seawater variability is still within published errors, see Paull et al. (1995).

Lake water sample ES1-50cm was analyzed twice as a replicate and WS1-111cm was prepared and measured twice as a method duplicate. The difference between the replicates of ES1-50cm is 0.000007, which is slightly less than the external reproducibility (± 0.000009). Between the duplicates of WS1-111cm, the difference is 0.000015, which is greater than the external reproducibility (± 0.000009).

Local well water and surface water conduit samples were replicated as well. The conduit water was also sampled twice, from both sides of the road, only one conduit sample (Conduit S) was replicated. Difference between replicates of the local well water (GRC Well) is 0.000005, which is similar to the lake water replicate difference and less than the external reproducibility (± 0.000009). Similarly, the difference of the conduit replicates is 0.000006. Twice the standard deviation of the two conduit samples and replicate is 0.000009, which is similar to but slightly greater than the external

reproducibility (± 0.000009). The reproducibility of the brackish conduit samples is greater than the seawater or hypersaline lake water.

Two replicates were measured for each microbialite subsample (WS1-i and WS1-6). For the HMC rich sample (WS1-i), the $^{87}\text{Sr}/^{86}\text{Sr}$ average value was 0.709178, where the difference between the two values was 0.000003. For the aragonite rich sample (WS1-6), the $^{87}\text{Sr}/^{86}\text{Sr}$ average value was 0.709173, where the difference between the two values was 0.000002. All four values were within instrumental external reproducibility (± 0.000009) of each other and twice the standard deviation of all four analyses, 0.000006, was less than the external reproducibility. In addition, the $^{87}\text{Sr}/^{86}\text{Sr}$ values for the carbonate samples were similar to lake water and local seawater.

Water samples from the northern sector of Storr's Lake ($n = 9$) have $^{87}\text{Sr}/^{86}\text{Sr}$ values ranging from 0.709155 to 0.709177 with a median of 0.709174 which was close to the average value measured for local seawater (0.709175, $n=4$). Water sample measurements from the southern sector ($n = 10$) had $^{87}\text{Sr}/^{86}\text{Sr}$ values ranging from 0.709155 to 0.709181 with a median of 0.709176, which was also close to the value measured for local seawater and to the values of the northern sector waters. The standard deviation of the northern sector waters is 0.000007 and the standard deviation of the southern sector was 0.000009, both were close to the external reproducibility (± 0.000009). Statistically, the water samples from the northern and southern sectors were not from different populations using a student's t-test at a significance level of 0.1%. Additionally, the standard deviation of all measured lake waters was 0.000008, which was slightly less than the external reproducibility of the measurements. No distinct trends

existed in $^{87}\text{Sr}/^{86}\text{Sr}$ values relative to lake water depth, however, depth profiles were only studied in the southern sector.

The average of two replicates from the local well water at Gerace Research Centre had a $^{87}\text{Sr}/^{86}\text{Sr}$ value of 0.709173, which was within error of published data from the same well: 0.709160 ± 0.000023 (Martin and Moore, 2008). While the majority of water samples measured in this study were collected in 2016, two additional water samples were collected in 2017 by Dr. David Wronkiewicz. One was local seawater and the other corresponds to WN3. $^{87}\text{Sr}/^{86}\text{Sr}$ at both locations for both years (2016 and 2017) were within error of each other.

Table 5-2 $^{87}\text{Sr}/^{86}\text{Sr}$ measured in Storr's Lake water, carbonate, and nearby locations. Error in each measurement is estimated to be ± 0.000009 calculated from the long-term reproducibility of NBS 987 on the TIMS at Ohio State (n=114).

Sample ID	$^{87}\text{Sr}/^{86}\text{Sr}$	Within Run Error (2SD)
Lake Water: northern sector		
WN1-44cm	0.709177	0.000005
WN3-104cm	0.709177	0.000006
WN3-2017	0.709174	0.000006
WN4	0.709169	0.000006
WN6	0.709169	0.000006
WN8-61cm	0.709177	0.000006
EN1	0.709164	0.000006
EN2	0.709175	0.000006
SWN1	0.709155	0.000005
Lake Water: southern sector		
WS1-5cm	0.709178	0.000008
WS1-50cm	0.709180	0.000005

Table 5-2 Continued

Sample ID	$^{87}\text{Sr}/^{86}\text{Sr}$	Within Run Error (2SD)
Lake Water: southern sector (contd.)		
WS1-111cm	0.709155	0.000006
WS1-111cm	0.709170	0.000006
WS2-46cm	0.709162	0.000006
WS1-5cm	0.709178	0.000006
WS1-50cm	0.709180	0.000006
WS1-111cm	0.709155	0.000005
WS1-111cm-duplicate	0.709170	0.000005
WS2-46cm	0.709162	0.000005
WS3-40cm	0.709178	
ES1-10cm	0.709166	0.000005
ES1-50cm	0.709181	0.000005
ES1-50cm	0.709173	
SSS1-40cm	0.709178	0.000006
Well Water		
GRC well	0.709172	0.000006
GRC well	0.709173	
Surface Water		
Conduit S	0.709170	0.000020
Conduit S	0.709167	0.000006
Conduit N	0.709176	0.000006
Seawater		
SW-2017	0.709181	0.000006
SS1-SW	0.709180	0.000005
SS1-SW	0.709171	0.000006
SS1-SW	0.709169	0.000006
Microbialite Carbonate		
WS1-i	0.709176	0.000006
WS1-i	0.709179	0.000006
WS1-6	0.709174	0.000006
WS1-6	0.709172	0.000005

$\delta^{44/40}\text{Ca}$ of Storr's Lake Water and Microbialites

MC-ICP-MS

The previously described microbialite WS1 (Li, 2017) and nearby waters were prioritized for analysis on the MC-ICP-MS at Penn State in Summer 2018 (Table 5-3 and Table 5-4). Three water samples were analyzed for $\delta^{44/42}\text{Ca}$ and $\delta^{44/43}\text{Ca}$, because MC-ICP-MS analysis does not allow for direct measurement of ^{40}Ca : SSI-SW (local seawater from Dim Bay), WS1-5cm (shallow lake water from above WS1), and WS1-111cm (deep lake water from above WS1). From within the microbialite WS1, two carbonate samples were analyzed: WS1-i with 94% HMC and WS1-6 with 96% aragonite (Li, 2017). The $\delta^{44/42}\text{Ca}$, $\delta^{42/43}\text{Ca}$, and $\delta^{44/40}\text{Ca}$ values relative to SRM 915a for each measured sample are shown in Table 5-4 and Figure 5-16. Two standards were also measured concurrently, SRM 915b and SRM 3109a, and are reported below. The samples and standards generally fall on the Ca mass dependent fractionation (MDF) line (Figure 5-16), but seem to diverge from the linear trend at higher delta values. The samples that fall off the MDF line (WS1-5cm, WS1-111cm, and SSI-SW) have a higher $\delta^{43/42}\text{Ca}$ than expected, which shifts them above the MDF line.

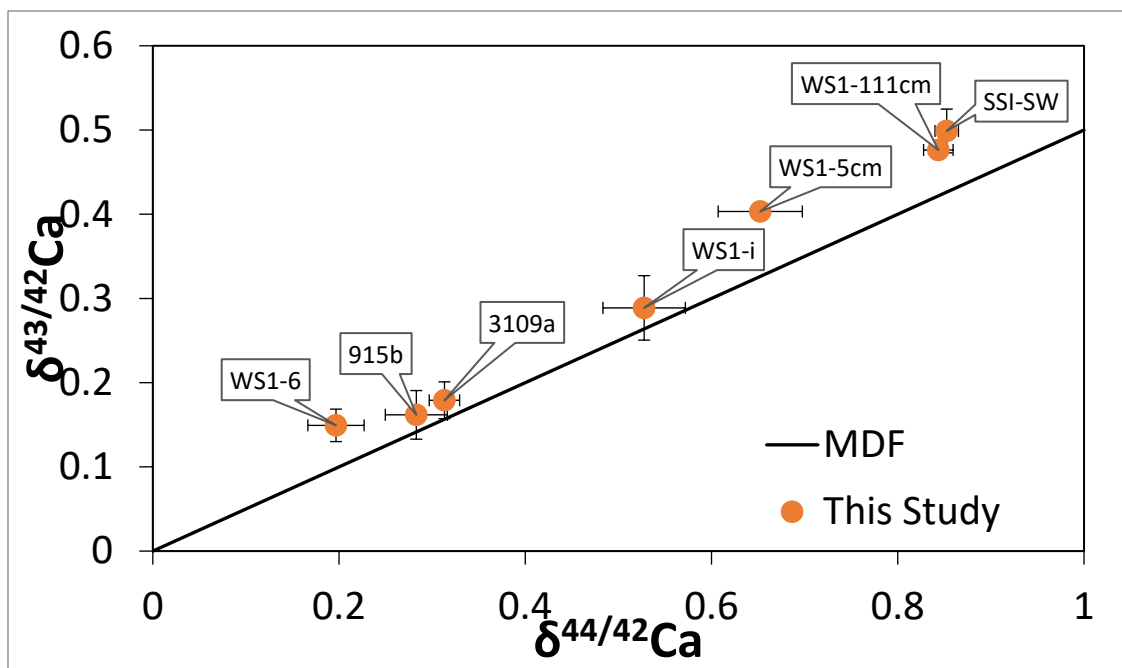


Figure 5-16 MC-ICP-MS samples plotted along the mass dependent fractionation line (MDF); all error bars are external 2SD on the analyzed samples and the nonvisible ones are smaller than the data point.

The $\delta^{44/40}\text{Ca}$ of SSI-SW (local seawater) is 1.75‰ (2SD = 0.03; n = 3), which is lower than published range of seawater values for MC-ICP-MS with a median value of $1.95 \pm 0.25\text{‰}$ (n=11) (Fantle and Tipper, 2014). The two lake water samples were distinctly different from each other despite being collected from the same location in the lake, but from different depths. The shallower water sample (WS1-5cm) had a lower $\delta^{44/40}\text{Ca}$ value of 1.34‰ (2SD = 0.10; n = 3), which differed by 0.39‰ from the deeper water sample (WS1-111cm). WS1-111cm had a $\delta^{44/40}\text{Ca}$ value, 1.73‰ (2SD = 0.03; n = 3), that was within error of the measurement for local seawater ($1.75 \pm 0.03\text{‰}$). The two carbonate samples had $\delta^{44/40}\text{Ca}$ values distinct from the surrounding lake water and

distinct from each other. WS1-i (94% HMC) had a higher $\delta^{44/40}\text{Ca}$ value, 1.08‰ (2SD = 0.10; n = 3), compared to WS1-6 (96% aragonite), which had a $\delta^{44/40}\text{Ca}$ value of 0.40‰ (2SD = 0.06; n = 3). The $\delta^{44/40}\text{Ca}$ difference between the two carbonate samples, WS1-i and WS1-6, is 0.68‰.

Table 5-3 Sample description, column recovery and number of replicates for samples measured on MC-ICP-MS at Penn State (Summer 2018)

Sample	sample type	Sr-spec %recovery	Cation exchange %recovery	n
<i>915b</i>	standard	n/a	n/a	8
<i>3109a</i>	standard	n/a	n/a	8
<i>WSI-i</i>	high-Mg calcite	101.6	91.9	3
<i>WSI-6</i>	aragonite	105.7	95.0	3
<i>WSI-5cm</i>	lake water	109.7	102.5	3
<i>WSI-111cm</i>	lake water	107.9	104.9	3
<i>SSI-SW</i>	seawater	93.0	118.7	3

Table 5-4 Ca isotopic values (relative to SRM 915a) for samples measured on MC-ICP-MS at Penn State (summer 2018) with error as 2SD of replicates

Sample	$\delta^{44/42}\text{Ca} \pm 2\text{SD}$ (‰)	$\delta^{43/42}\text{Ca} \pm 2\text{SD}$ (‰)	$\delta^{44/40}\text{Ca} \pm 2\text{SD}$ (‰)
<i>915b</i>	0.28±0.03	0.16±0.03	0.58±0.07
<i>3109a</i>	0.31±0.02	0.18±0.02	0.64±0.03
<i>WSI-i</i>	0.53±0.04	0.29±0.04	1.08±0.10
<i>WSI-6</i>	0.20±0.03	0.15±0.02	0.40±0.06
<i>WSI-5cm</i>	0.65±0.05	0.40±0.01	1.34±0.10
<i>WSI-111cm</i>	0.84±0.02	0.48±0.01	1.73±0.03
<i>SSI-SW</i>	0.85±0.01	0.50±0.03	1.75±0.03

TIMS

The majority of samples were analyzed for $\delta^{44/40}\text{Ca}$ on the TIMS at Ohio State in January and February 2020 (Table 5-5). Data is reported relative to the average SRM 915a measurement from that wheel (n=2 per wheel). Additionally, the internal 2SD of the measured 44/40 ratio is reported each analysis. Samples are labeled as “auto” if they were heated using the automatic heating method (Table 5-5). The rest are labelled as “manual” indicating they were heated manually (Table 5-5).

Lake water samples from both the northern (n=4) and southern (n=7) sectors of Storr’s lake were analyzed. To compare differences in the $\delta^{44/40}\text{Ca}$ of the northern and southern sectors of Storr’s Lake, a Welch’s unequal variances t-test was used to test the difference in the means using the function “t.test” within the language R. The difference in the means was not significant at the 5% confidence level (p=0.078). Additionally, there was no significant linear correlation of $\delta^{44/40}\text{Ca}$ in either sector relative to various parameters (p >>0.05 for all parameters) as shown in Figure 5-17 (including Sr:Ca molar ratio, SI of calcite, and pH; plots not shown). A linear correlation p value less than the significance level (0.05) indicates a significant linear correlation.

Table 5-5 $\delta^{44/40}\text{Ca}$ values measured in Storr's Lake water, carbonate, and local seawater

Sample ID	$\delta^{44/40}\text{Ca}$ (‰, rel. to 915a)	Within Run Error on 44/40 (2SD)	Heating Method
Lake Water: northern sector			
WN4-75cm	1.89	0.00049	auto
WN3-102cm	1.77	0.00018	auto
WN8-61cm	1.77	0.00024	auto
WN6-120cm	1.82	0.00024	auto
Lake Water: southern sector			
WS1-5cm	1.76	0.00024	manual
WS1-5cm	1.73	0.00019	manual
WS1-111cm	1.68	0.00016	auto
WS1-111cm	1.77	0.00017	auto
WS1-50cm	1.76	0.00022	auto
WS3-40cm	1.66	0.00031	auto
WS2-46cm	1.75	0.00029	auto
ES1-10cm	1.73	0.00024	manual
ES1-50cm	1.81	0.00025	auto
Microbial Carbonate : WN7			
WN7-i	0.94	0.00023	manual
WN7-ii	0.86	0.00022	manual
WN7-1	0.56	0.00033	manual
WN7-3	0.61	0.00016	manual
Microbial Carbonate : WS1			
WS1-6 CX	0.38	0.00019	manual
WS1-1	0.93	0.00012	manual
Seawater: Dim Bay			
SW-2017	1.84	0.00007	auto
SSI-SW-A	1.84	0.00025	manual
SSI-SW-B	1.86	0.00027	auto

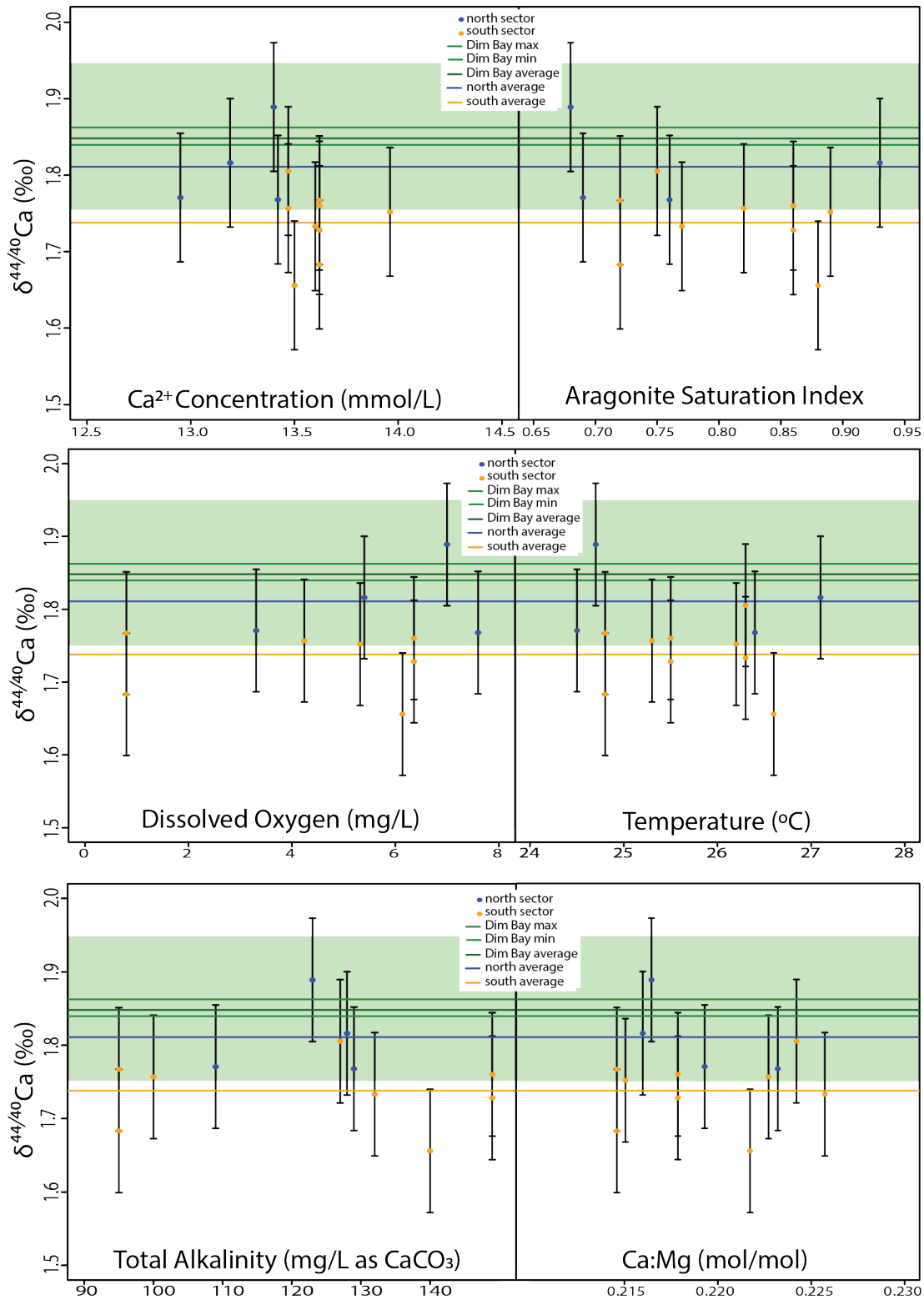


Figure 5-17 Variability of $\delta^{44/40}\text{Ca}$ in Storr's Lake water relative to various parameters, where the light green rectangle shows the extent of the error bars on measurements of local seawater.

Spatially, the $\delta^{44/40}\text{Ca}$ of Storr's Lake water is visualized along two depth profiles and two lateral transects. In the southern sector of the lake, two depth profiles were collected and measured for $\delta^{44/40}\text{Ca}$ at sample sites WS1 and ES1. As shown in Figure 5-18, no depth trends are visualized and all measurements are within external 2SD of each other ($\pm 0.08\%$). Samples were collected along transects in the northern (WN transect) and southern (WS transect) sector of the lake (Figure 2-3). Along both transects measurements are within error of each other and show no visualized trends in the data (Figure 5-19).

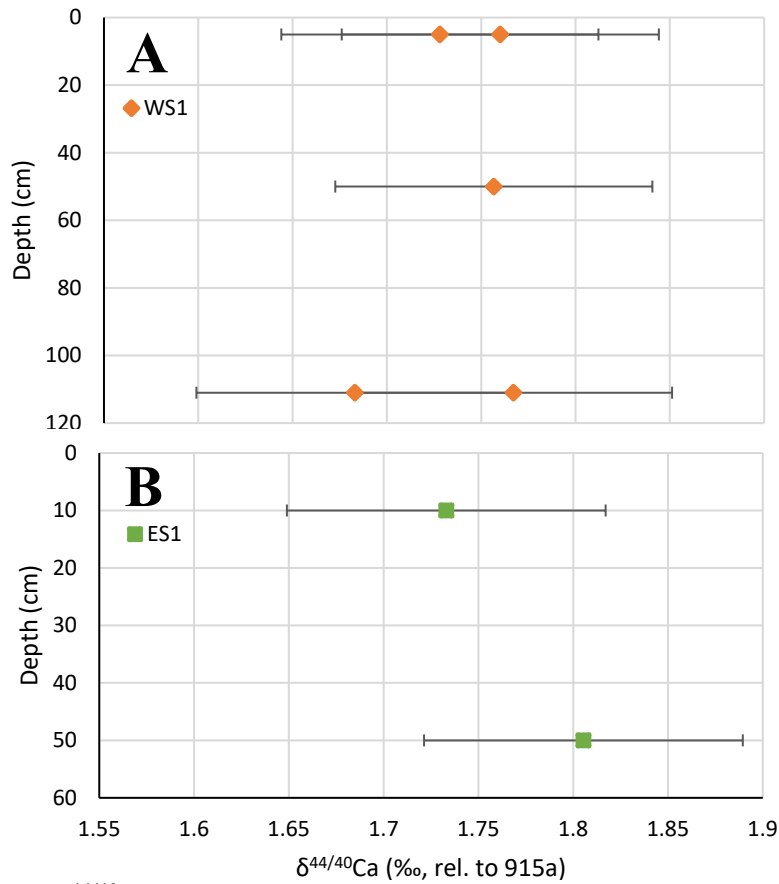


Figure 5-18 $\delta^{44/40}\text{Ca}$ depth profiles from WS1 (A) and ES1 (B) in Storr's Lake

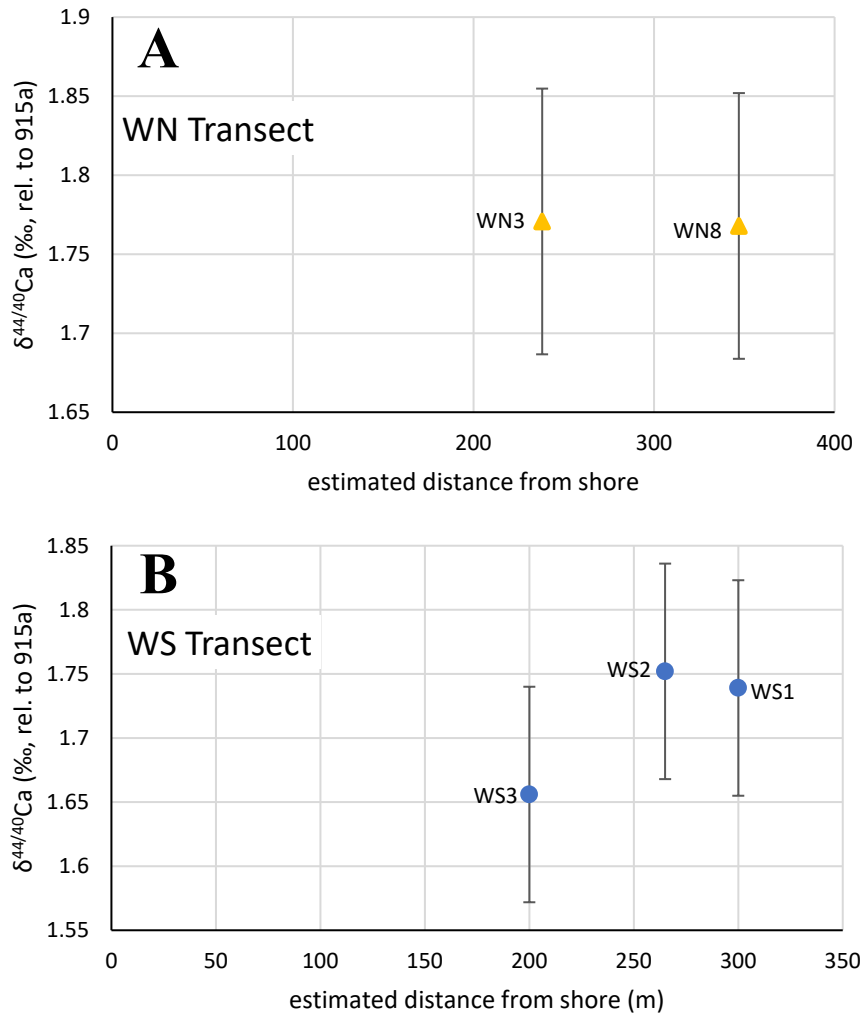


Figure 5-19 $\delta^{44/40}\text{Ca}$ lateral transects from the western sides of the northern (A) and southern (B) sectors of Storr's Lake

In addition to the water samples, microbialite subsamples were measured from two separate microbialites (WS1 and WN7). The carbonate subsamples were previously measured for $\delta^{25}\text{Mg}$, $\delta^{13}\text{C}$, $\delta^{18}\text{O}$, mineralogy, and trace elements as shown in Table 5-7 (Li, 2017). $\delta^{44/40}\text{Ca}$ of the carbonates were plotted against each variable (Figure 5-20). $\delta^{44/40}\text{Ca}$ shows a significant negative linear correlation with wt% of aragonite as

determine by XRD ($r^2=0.9009$, $p=0.0038$) (Figure 5-20A). There is a significant negative linear correlation ($r^2=0.6873$, $p=0.0413$) between $\delta^{44/40}\text{Ca}$ and $\delta^{25}\text{Mg}$ (Figure 5-20B). The existing data suggest a negative linear correlation between $\delta^{44/40}\text{Ca}$ and $\delta^{18}\text{O}$ (Figure 5-20C), however, it is not significant ($r^2=0.5299$, $p=0.101$). Similarly, between $\delta^{44/40}\text{Ca}$ and $\delta^{13}\text{C}$, there is a slight positive linear relationship (Figure 5-20D) which is not significant ($r^2=0.3239$, $p=0.2385$). In agreement with the relationship with mineralogy, Sr:Ca molar ratio has a significant negative linear correlation with $\delta^{44/40}\text{Ca}$ (Figure 5-20E; $r^2=0.8329$, $p=0.0111$) and Ca:Mg molar ratio also has a significant positive linear correlation (Figure 5-20; $r^2=0.9246$, $p=0.0022$) with $\delta^{44/40}\text{Ca}$.

Table 5-6 Selected data from Li, 2017 for microbialite subsamples

Sample ID	Ca:Mg (mol/mol)	Sr:Ca (mol/mol)	mol% Mg	Aragonite (wt%)	$\delta^{13}\text{C}$ (‰ VPDB)	$\delta^{18}\text{O}$ (‰ VPDB)	$\delta^{25}\text{Mg}$ (‰ DSM3)
Microbial Carbonate: WN7							
WN7-i	7.1	0.0004	12.2	7	-0.9	0.4	-1.52 ±0.15
WN7-ii	9.2	0.006	9.7	25	0.4	1.2	-1.55±0.09
WN7-1	51.3	0.012	1.9	87	-0.4	1.3	-1.46±0.07
WN7-3	54	0.013	1.8	90	-0.7	1	-1.21±0.1
Microbial Carbonate: WSI							
WS1-1	8.3	0.006	10.7	28	-0.9	0.8	-1.56±0.12
WS1-6	154.8	0.014	0.6	96	-2.5	1.3	-1.22±0.07

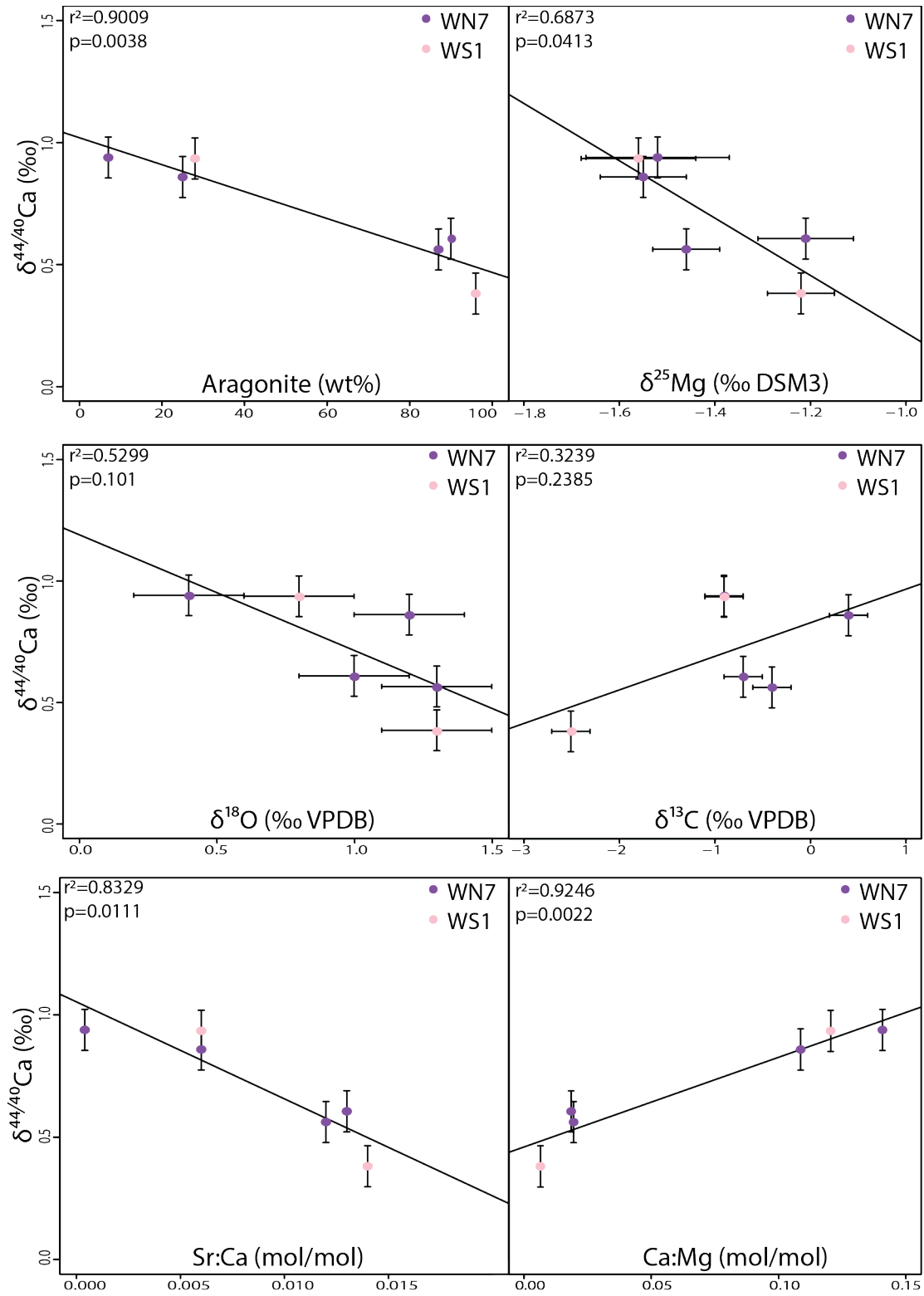


Figure 5-20 $\delta^{44/40}\text{Ca}$ of carbonate subsample correlations with various measurements on the same samples.

Chapter 6. Discussion

Morphology, Mineralogy and Elemental Concentrations

Morphology of microbialites is largely controlled by depth in Storr's Lake, with deeper microbialites receiving a lot less sunlight than shallower microbialites due to the high turbidity of the lake water (Mann and Nelson, 1989). This is evident in the microbialites studied for this work as well. Calcareous knobs were not found below depths of 60 cm and they were also the only morphology to have a sample (WN1A) without any aragonite, as measured using powder XRD. Both mushroom morphologies were found at a large range of water depths (41 cm to ~167 cm) and included the highest wt% of aragonite measured in this study (WN5-VI = 28.3 wt% aragonite). The morphology and water depth correlation has been linked to the presence of aragonite by Paul et al. (2016) and Li (2017), which serves as the basis for my first hypothesis.

The new mineralogical data collected in this study supports my first hypothesis. Hypothesis 1: *I hypothesize that microbialites with more accommodation space (i.e., deeper water; greater than ~40cm depth in the water column at the time of collection) will all have a transition from high-Mg calcite to aragonite because they were able to grow tall enough that heterotrophy dominates within the interior of the microbialite and the transformation from high-Mg calcite to aragonite can start to occur.* A minimum water depth of ~40 cm for aragonite precipitation is supported by the lack of aragonite

within WN1A (collected at a water depth of 40 cm in January 2016) and the presence of aragonite in all deeper water microbialites. Without measurement of shallower microbialites the minimum water depth is difficult to precisely determine, especially because aragonite was found within SWN2 (another calcareous knob). This microbialite (SWN2) was collected from a water depth of roughly 40 cm, however potential error in the depth measurement comes from wind created waves the day the microbialite was collected. With the similar depths of SWN2 and WN1A, I cannot draw a specific minimum water depth limit where precipitation of aragonite occurs within Storr's Lake microbialites. Additionally, WN1A was collected nearest to a brackish surface water inflow conduit, however any influence in lake water chemistry at this site is overwhelmed by the high salinity and concentration of Mg^{2+} and Ca^{2+} in Storr's Lake (Li, 2017). Future researchers exploring the relationship between aragonite within Storr's Lake microbialites and water depth should note that the lake water level can change by about 16 cm annually or more on longer time scales as it is dependent on rainfall and evaporation, with no tidal influence (Mann and Nelson, 1989). Variability in lake water level measurement can also be introduced due to the muddy lake bottom throughout much of the lake and variable wind speeds making measurement consistency difficult.

To confirm the mineralogy measurements, elemental concentrations were measured for each microbialite subsample for Mg, Sr, and Ca. These concentrations were used to calculate molar ratios (Mg:Ca and Sr:Ca) and mol% Mg in the carbonate. As expected there is a positive linear relationship between Sr:Ca and wt% aragonite in my measured data (Figure 5-13A). This relationship is due to the crystal structure of

aragonite having a higher substitution capacity for Sr than HMC, because of the nine-fold coordination of Ca and longer Ca-O bonds in the orthorhombic crystal structure of aragonite (Figure 6-1A) (Wassenburg et al., 2016; Wang et al., 2017). This relationship holds with samples that have even higher wt% aragonite. The positive linear relationship is clear, when the new data is combined with data from different microbialites (Li, 2017), sampled at the same time as the ones discussed here, with higher wt% aragonite (Figure 5-13B). Interestingly, both this study and Li (2017) have a distinct lack of subsamples with wt% aragonite between 30 and 70 wt% as determined by powder XRD. The strong correlation is upheld between aragonite wt% and Sr distribution coefficients for this study combined with Li's data (Figure 6-2; $p < 2.2e-16$, $r^2 = 0.9366$). The Sr distribution coefficients were calculated as the Sr:Ca molar ratio of the carbonate divided by the Sr:Ca molar ratio of the nearest water sample to the microbialite.

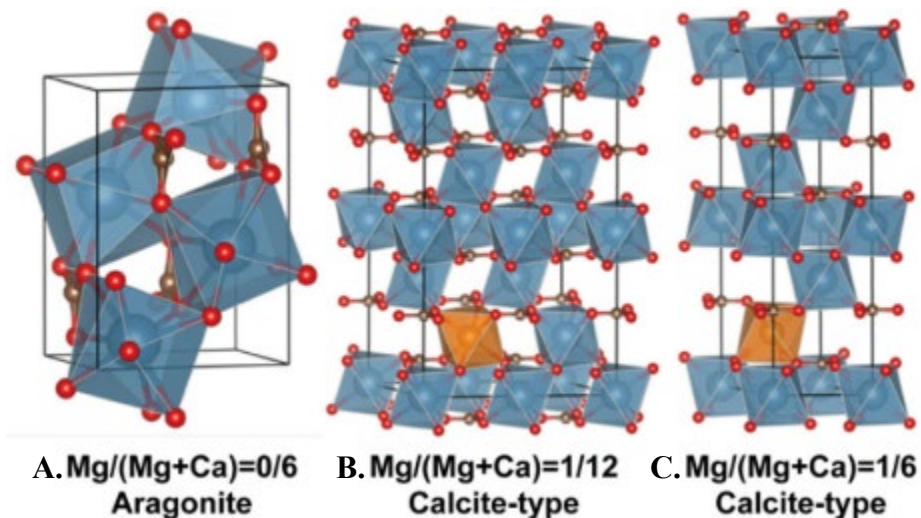


Figure 6-1 Aragonite and HMC crystal structures for different mole fractions of Mg (B-1/12; C-1/6). Modified from Wang et al. (2017)

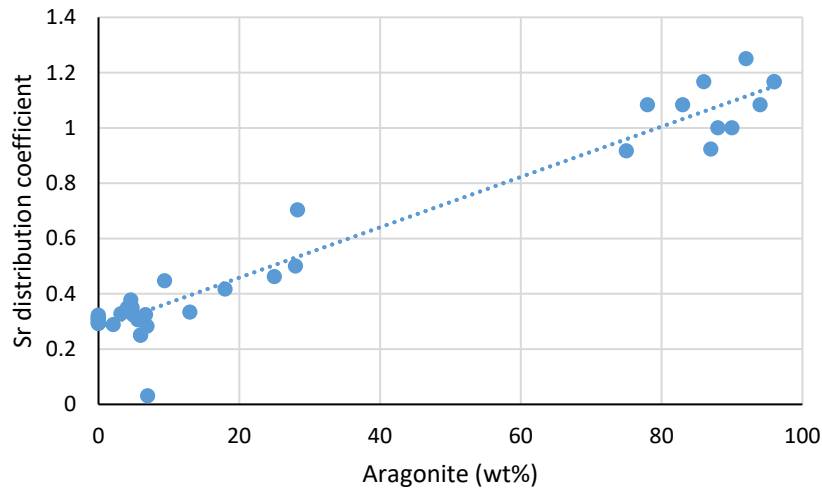


Figure 6-2 Sr distribution coefficient between carbonate and lake water versus mineralogy; data from this study combined with Li (2017).

The relationship between Mg:Ca and wt% aragonite is also a significant positive linear relationship (Figure 5-14B). In this instance, the crystal structure of HMC has a high substitution capacity for Mg, but Mg does not substitute for Ca within aragonite (Wang et al., 2017; Figure 6-1A). The lower molar ratios of Mg:Ca correspond to high wt% aragonite and low wt% HMC. In aragonite, Ca^{2+} has a nine-fold coordination, rather than the six-fold coordination of calcite, which, in addition to having a denser crystal structure, potentially prevents the incorporation of Mg^{2+} into aragonite (Loste et al., 2003; Greer et al., 2015). Low concentrations of Mg are seen within aragonite in Storr’s Lake. This Mg is likely hosted within disordered Mg-bearing carbonates and/or organic matter within the aragonite rich microbialite carbonate (Finch and Allison, 2008).

When looking at the structure of HMC, the replacement of Ca with Mg can be discussed as a fraction of 12 Ca atoms in a “supercell”, with relevant examples of this

shown in Figure 6-1 (Wang et al., 2017). Given the ranges of mol% Mg measured for samples with 100% HMC (14-16%), the structure of the HMC in Storr's Lake microbialites is largely 1/6 Mg (Figure 6-1C) with a few 1/12 Mg cells (Figure 6-1B) mixed in. Mg incorporation into calcite is thought to be influenced by the presence of organic matter, which can stabilize higher mol% Mg HMC (4-44%) (Loste et al., 2003; Wombacher et al., 2011; Greer et al., 2015). The distribution coefficients of Mg in this study combined with Li (2017) also holds a strong linear correlation with wt% aragonite ($p = <2.2e-16$ $r^2=0.9795$; Figure 6-3). Mg distribution coefficients were calculated as the Mg:Ca molar ratio of the carbonate divided by the Mg:Ca molar ratio of the nearest water sample to the microbialite.

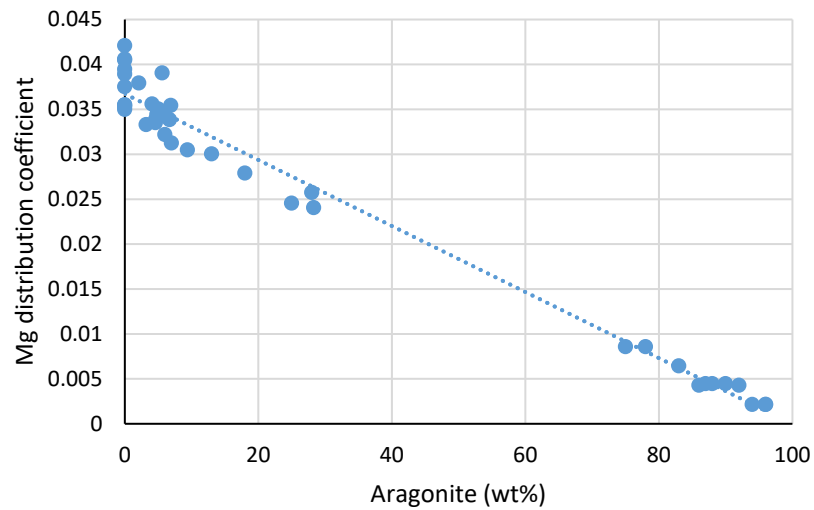


Figure 6-3 Mg distribution coefficient between carbonate and lake water versus mineralogy; data from this study combined with Li (2017).

Trace element distribution coefficients in carbonates have been used to explore reaction rate (Tang et al., 2008a, 2012; Gabitov et al., 2014; Alkhatib and Eisenhauer, 2017b, 2017a; Giri et al., 2018) and can be used in this study to understand the interaction between the space where carbonate is precipitating and the surrounding ocean/lake water. The range of Sr distribution coefficients for microbialite samples with >90 wt% aragonite, 1.08 to 1.17, is similar to the range for biogenic aragonite (skeletal carbonate from scleractinian coral *Pocillopora damicornis*) of 1.03 to 1.13 (Giri et al., 2018). Giri et al. (2018) cultivated corals in seawater solutions with different Mg, Ca, and Sr concentrations and determined that the pore space of the corals was partially open to seawater. Abiotic aragonite crystals were grown under a variety of reaction rates and temperatures by (Alkhatib and Eisenhauer, 2017a), with a range of Sr distribution coefficients from 0.978 to 1.228 which includes the range of values for the microbialite samples with >90 wt% aragonite (1.08 to 1.17). Given the range of Sr distribution coefficients calculated for the microbialites samples in comparison to both an open (Alkhatib and Eisenhauer, 2017a) and a leaky (Giri et al., 2018) system, I conclude that Sr^{2+} is in communication with the lake water in the deeper aragonite precipitating portions of the microbialites.

However, the Mg distribution coefficients of aragonite were calculated from the aragonite rich (>90 wt%) microbialite subsamples using simple two endmember mixing equation 6-1 ($1.58\text{e-}5$ to $4.23\text{e-}5$). The Mg distribution coefficient for HMC ($D_{\text{Mg,HMC}}$) was calculated as the average $D_{\text{Mg,HMC}}$ of ten microbialite subsamples with 100% HMC.

The calculated range of Mg distribution coefficients for aragonite ($D_{Mg,aragonite}$) is $1.58e-5$ to $4.23e-5$.

$$D_{Mg,HMC} * wt\% HMC = D_{Mg,aragonite} * wt\% aragonite \quad \text{Eq. 6-1}$$

Coral Mg distribution coefficients reported by Giri et al. (2018) ranging from $8.7e-4$ to $10.3e-4$. Abiotic aragonite Mg distribution coefficients range from $0.367e-3$ to $1.590e-3$ (Alkhatib and Eisenhauer, 2017a). Given the range of microbialite aragonite Mg distribution coefficients ($1.58e-5$ to $4.23e-5$) in comparison to Giri et al. (2018)'s leaky system and Alkhatib and Eisenhauer (2017a)'s open system, it is unlikely that the Mg^{2+} in the aragonite section of microbialites is in open communication with the lake water.

In the 100% HMC microbialite subsamples, the Sr distribution coefficients ranged from 0.29 to 0.32, which was a bit higher than the Sr distribution coefficient for abiotic calcite precipitation experiments (0.078 to 0.225) (Alkhatib and Eisenhauer, 2017b) which could be due to the fact that the microbialite calcite has such high Mg content, different from the experimental calcite. The high Mg content of the microbialite calcite (14-16mol% Mg, HMC) is in the upper range for biogenic carbonates (Long et al., 2014).

$^{87}Sr/^{86}Sr$ Groundwater Tracing

Martin and Moore (2008) measured radiogenic Sr isotopes ($^{87}Sr/^{86}Sr$), Sr concentrations, salinity and Cl concentrations in waters on San Salvador Island (SSI) to calculate deep groundwater input and bedrock $^{87}Sr/^{86}Sr$ using a mixing model but did not

study Storr's Lake. Their model used chloride concentrations as a conservative tracer of seawater, because it was strongly correlated with salinity in their data and because no chloride bearing minerals are present on SSI (Martin and Moore, 2008). Chloride was then used to calculate the mole fraction of Sr²⁺ from the limestone bedrock ($f_{\text{Sr-carbonate}}$, equation 6-2). The carbonate fraction of Sr²⁺ was then used along with lake water ⁸⁷Sr/⁸⁶Sr in a simple two end member mixing model to calculate the ⁸⁷Sr/⁸⁶Sr of the bedrock the groundwater originated from (equation 6-3).

$$f_{\text{Sr,carb}} = 1 - \frac{\left(\frac{\text{Sr}}{\text{Cl}}\right)_{\text{seawater}} * \text{Cl}_{\text{sample}}}{\text{Sr}_{\text{sample}}} \quad \text{Eq. 6-2}$$

$$\left(\frac{{}^{87}\text{Sr}}{{}^{86}\text{Sr}}\right)_{\text{sample}} = f_{\text{Sr,carb}} * \left(\frac{{}^{87}\text{Sr}}{{}^{86}\text{Sr}}\right)_{\text{carbonate}} + (1 - f_{\text{Sr,carb}}) * \left(\frac{{}^{87}\text{Sr}}{{}^{86}\text{Sr}}\right)_{\text{seawater}} \quad \text{Eq. 6-3}$$

Significant groundwater flux could alter and add heterogeneity to the geochemistry of Storr's Lake and the microbialites forming in the lake. To try and quantify this influence, I measured ⁸⁷Sr/⁸⁶Sr values of the lake water and potential sources of water to the lake to determine if Sr could be used to examine the flux of groundwater into the lake with the model from Martin and Moore (2008). However, as shown in Figure 6-3, chloride does not show a strong linear correlation with salinity for Storr's Lake, which suggests that it is not conservative in Storr's Lake, or that there is significant error in either the salinity or the chloride measurements reported by Li (2017). The high salinity of the lake could contribute to the variability in measurements and matrix effects

from high amounts of dissolved organic matter could also affect the measurement of chloride. Additionally, the isotopic composition of shallow groundwater in this region is not very different from modern seawater because it is recent carbonate and the $^{87}\text{Sr}/^{86}\text{Sr}$ of seawater hasn't shifted substantially since it was deposited (Martin and Moore, 2008). For a few water samples the mixing calculations could be made (highlighted in dark blue in Figure 6-3), including GRC well, both conduit water samples, WN1-44cm, WN6, and WN3-2017 (Table 6-1). These data points follow the conservative trend of Martin and Moore's (2008) data, suggesting that their model applies to these samples (Figure 6-3).

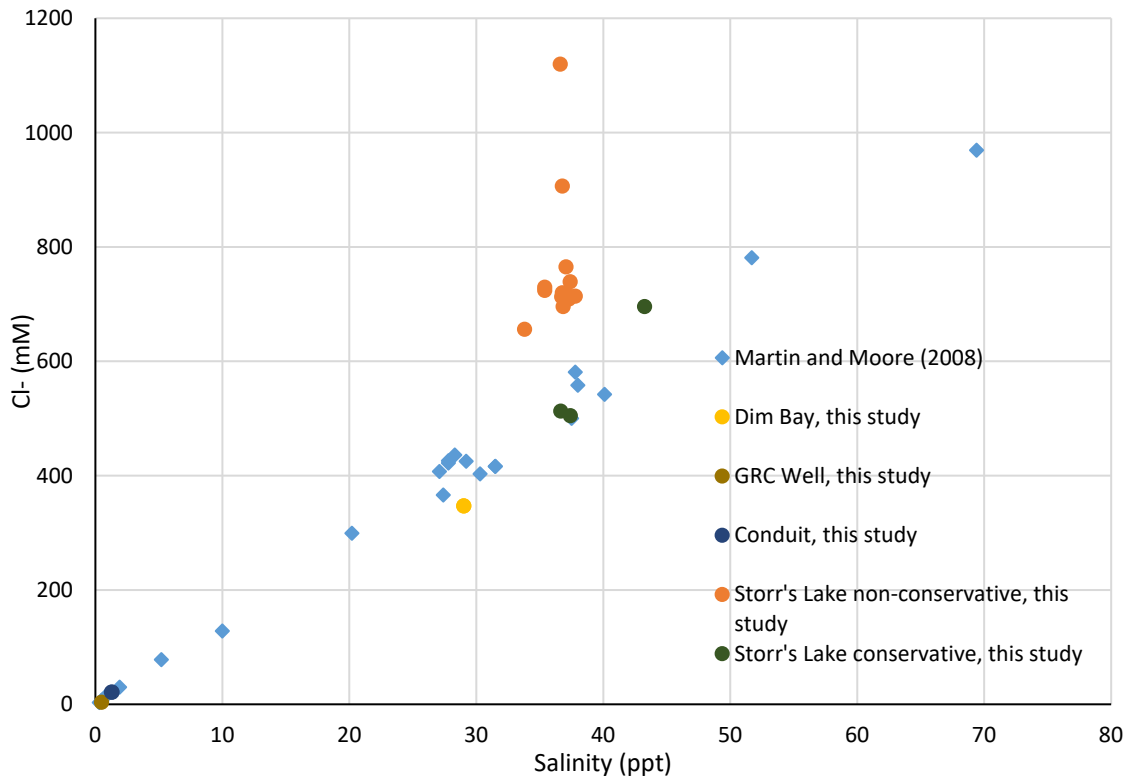


Figure 6-4 Chloride and salinity data from this study and Martin and Moore (2008).

Table 6-1 Conservative samples from Storr's Lake and surrounding water sources with the carbonate fraction and carbonate $^{87}\text{Sr}/^{86}\text{Sr}$ calculated following Martin and Moore (2008). Elemental concentrations and salinities from Li (2017).

Samples	Salinity (PSU)	Cl (mM)	Sr (mM)	$^{87}\text{Sr}/^{86}\text{Sr}$ sample	External 2SD	$f_{\text{Sr,carb}}$	$^{87}\text{Sr}/^{86}\text{Sr}$ carbonate
<i>Dim Bay</i>	29.02	346.8	0.08	0.709173	0.000009	0.00	-
<i>GRC well</i>	0.50	3.3	0.09	0.709173	0.000009	0.99	0.709173
<i>Conduit S</i>	1.33	21.0	0.06	0.709169	0.000009	0.92	0.709168
<i>Conduit N</i>	1.27	21.0	0.04	0.709176	0.000009	0.89	0.709176
<i>WN1- 44cm</i>	36.66	512.6	0.17	0.709177	0.000009	0.30	0.709186
<i>WN6</i>	37.42	504.5	0.15	0.709169	0.000009	0.22	0.709154
<i>WN3-2017</i>	43.27	695.4	0.17	0.709174	0.000009	0.03	0.709176

My calculations suggest no more than 30% groundwater input into Storr's Lake (Table 6-1), which is consistent with the values calculated for other lakes on the island (Martin and Moore, 2008). Even with 30% groundwater input into the northern sector of Storr's Lake, the Sr^{2+} concentration is much larger in seawater than groundwater and the estimated $^{87}\text{Sr}/^{86}\text{Sr}$ of the carbonate bedrock is similar to my local seawater measurement, though outside the external error bars (Figure 6-4). Using the projected mixing lines and error bars in Figure 6-5, only greater than 70% groundwater influence would be quantifiable using $^{87}\text{Sr}/^{86}\text{Sr}$ and even then, only at WN3.

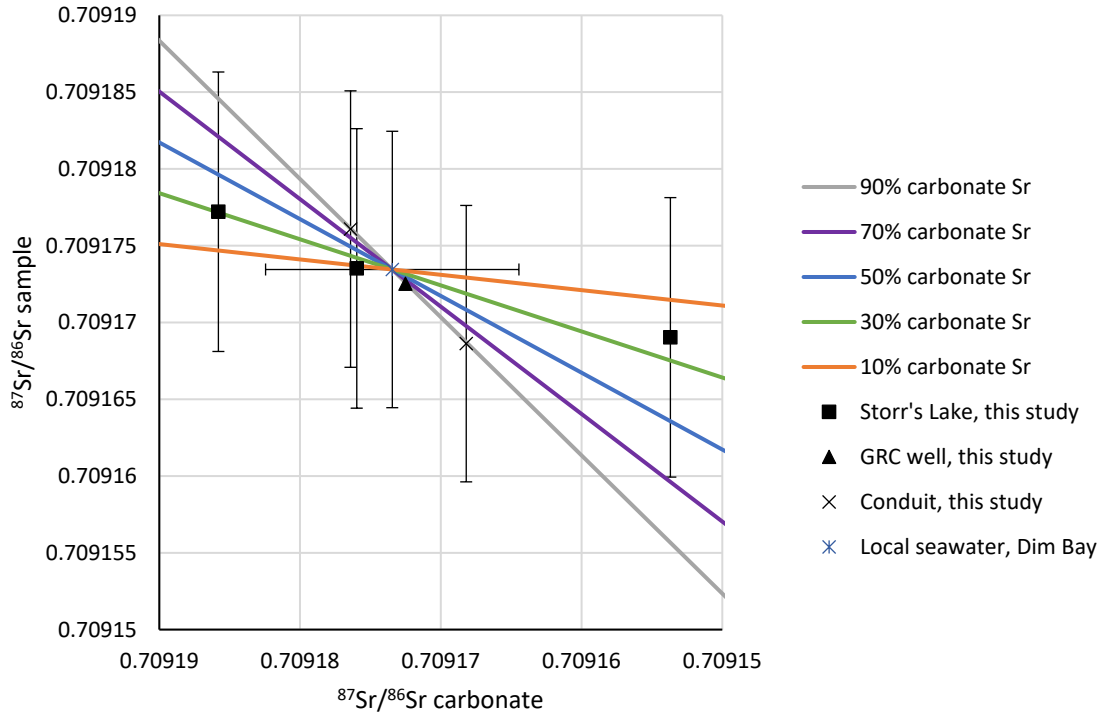


Figure 6-5 Calculated mixing lines from Martin and Moore (2008), overlain by data from this from this study. The central point of the plot is the local seawater value.

Within the precision of the measurement (± 0.000009 , average 2SD of NBS 987, $n=114$) no differentiation can rigorously be made at this time with regards to any variability of $^{87}\text{Sr}/^{86}\text{Sr}$ within Storr's Lake, including the groundwater calculations and mixing lines from Figure 6-4. A student's t-test of the $^{87}\text{Sr}/^{86}\text{Sr}$ data shows that the northern and southern sectors have statistically the same mean ($p=0.7261$). This exercise illustrates the maximum amount of groundwater that could be impacting the Sr content of the lake water. Furthermore, this new data confirms no Saharan dust input significantly alters the lake water $^{87}\text{Sr}/^{86}\text{Sr}$ from seawater, as expected (e.g., Schulting et al., 2018).

$\delta^{44/40}\text{Ca}$ Understanding of Microbialite formational processes

Variability within Storr's Lake water $\delta^{44/40}\text{Ca}$ (*Hypothesis 2*) was studied to investigate the effect it could have on the $\delta^{44/40}\text{Ca}$ of the microbialites. It was hypothesized that both sectors of the lake would be homogeneous in their isotopic composition and primarily influenced by seawater. A Welch's t-test was used to test the difference in the means between the northern sector (n=4) and the southern sector (n=7), which resulted in a p value of 0.078. For this test, when the p value is greater than the significance level, both populations are statistically the same (accept the null hypothesis). However, the significance level is somewhat arbitrary and usually ranges from 5% to 10%. While the $\delta^{44/40}\text{Ca}$ p value is above the significance level of 0.05 suggesting no significant variability between the two sectors, it would be below a significance level of 0.1 suggesting significant variability (at the 10% significance level). The $\delta^{44/40}\text{Ca}$ means of the northern and southern sectors are within external reproducibility ($\pm 0.08\%$) of each other and seawater. However, the p value for $\delta^{44/40}\text{Ca}$ is much lower than the p value for the $\delta^{25}\text{Mg}$ data (p=0.848) from the northern (n=6) and southern (n=4) sectors utilizing the same function (Li, 2017). While this comparison suggests more variability in $\delta^{44/40}\text{Ca}$ than $\delta^{25}\text{Mg}$ of lake water, there is potential for sampling bias between the two data sets, especially since more samples in the northern sector and less in the southern sector were measure for $\delta^{25}\text{Mg}$. This difference suggests that the primary Ca isotopic difference may be in the smaller and shallower southern sector and should be investigated further. It should be noted that only the TIMS data is used for this analysis since there is some suggestion that the MC-ICPMS is influenced by incomplete Sr separation.

The average lake water $\delta^{44/40}\text{Ca}$ ($1.76\text{‰} \pm 0.1\text{‰}$, 2SD) differs significantly from local seawater ($1.85\text{‰} \pm 0.1\text{‰}$, 2SD) (t-test, $p=0.0012$), despite being within error. This is interesting because the history and hydrology of Storr's Lake implies that it is simply a more concentrated version of seawater and because $\delta^{25}\text{Mg}$ in Storr's Lake was homogeneous and exactly the same as seawater (Li, 2017). As described in Chapter 2, the lake was formed as a tidally influenced lagoon later separated from the ocean.

To quantify seawater influence on each sector of the lake, I performed a one-way ANOVA on the lake water and seawater, and then a Tukey multiple pairwise-comparison after the ANOVA returned a significant result. In both of these statistical tests when the p value is less than the significance level (0.05) it shows a statistical difference between the means of the populations. The results of the ANOVA showed significant differences between at least two of the three groups ($p=0.01$). Then the Tukey comparisons showed that the northern sector $\delta^{44/40}\text{Ca}$ was significantly related to seawater ($p=0.59$), but that the southern sector $\delta^{44/40}\text{Ca}$ was significantly different from seawater ($p=0.015$). As expected, given the statistics discussed above, the Tukey comparison of the northern and southern sectors was right on the line of potentially significant difference between the two populations ($p=0.060$). Doubling the $\delta^{44/40}\text{Ca}$ data in the Northern sector (from 4 to 8 samples) may change the relationship between the two sectors or confirm this observation.

On a smaller scale, spatial variability can be quantified using water depth profiles and lateral transects. From two depth profiles in the southern sector, no obvious changes occurred with water depth in the lake (Figure 5-17). The lack of a clear correlation with

water depth shows that there was no significant enrichment from the precipitation of carbonate, because both depth profiles were directly above microbialites where carbonate is precipitated. Along the northern transect, moving away from the conduit there was also no change in lake water $\delta^{44/40}\text{Ca}$ as expected from the water chemistry and $\delta^{25}\text{Mg}$ data (Li, 2017). However, there may be an unmeasured trend in other parts of the lake.

To discover a potential source for variability in the southern sector lake water $\delta^{44/40}\text{Ca}$, I plotted $\delta^{44/40}\text{Ca}$ against many different analytes (water Sr:Ca, water Ca:Mg, water saturation index of calcite and aragonite, water Ca^{2+} concentration, dissolved oxygen, temperature, total alkalinity, and pH). No significant correlations were found for the whole lake (all $p \gg 0.05$) or within either sector (all $p \gg 0.05$). For a linear correlation, p values less than the significance level (0.05) indicates a significant linear correlation (rejection of the null hypothesis). This lack of correlation suggests that $\delta^{44/40}\text{Ca}$ is likely not significantly impacted by any of the parameters tested. The lack of a significant correlation with mineral saturation state suggests that the precipitation of carbonate either in microbial mats or in the water column does not significantly enrich the lake water.

Therefore, testing hypothesis 2 (*I hypothesize that the Ca isotope budget within the lake will be dominated by seawater and uniform within the lake similar to that for Mg and Sr isotopes*) is more complex than I first imagined, but the dominant seawater influence is at least true in the northern sector of the lake. Caution should be exercised as the differences between the sectors could be impacted by sampling bias.

Other sources of variability in Storr's Lake $\delta^{44/40}\text{Ca}$ include: incomplete mixing of external water sources to the lake (groundwater, seawater, and/or surface water) and Ca

isotopic fractionation during adsorption of Ca^{2+} cations by organic matter in the water column.

Groundwater would shift the $\delta^{44/40}\text{Ca}$ value of lake water to lower values due to the influence of the Pleistocene/Holocene bedrock on the island ($\delta^{44/40}\text{Ca}_{\text{groundwater}} = 0.85\text{‰}$, rel. to SRM915a), however, the Ca concentration of groundwater is quite low 1.1 mM compared to 10 mM of local seawater and 13 mM for the lake water (Neumann et al., 1989; Holmden et al., 2012; Li, 2017). Using simple two end member mixing (groundwater = 0.85‰, rel. to SRM915a and seawater = 1.85‰, rel. to SRM915a, equation 6-4) along with the maximum range of groundwater influence ($f = 10\text{-}30\%$) calculated using the method from Martin and Moore (2008), I calculated the range of lake water $\delta^{44/40}\text{Ca}$ plausible due to groundwater influence (Table 6-2; this study; Holmden et al., 2012). However, this simple mixing model does not account for the different concentrations of Ca^{2+} in groundwater and lake water. To further test the plausibility of this model, I estimated that 123% volume of groundwater to lake water would be required for 10% of lake water Ca^{2+} to be from groundwater. This percentage precludes the possibility of groundwater influence on $\delta^{44/40}\text{Ca}$, because an excessive amount of groundwater would distinctly change lake water salinity, which is not seen (Holmden et al., 2012; Li, 2017).

$$\delta^{44/40}\text{Ca}_{\text{sample}} = f * (0.85\text{‰})_{\text{carbonate}} + (1 - f) * (1.85\text{‰})_{\text{seawater}}$$

Eq. 6-4

Table 6-2 Calculated lake water $\delta^{44/40}\text{Ca}$ for a range of groundwater influence

Fraction of Groundwater influence	calculated lake water $\delta^{44/40}\text{Ca}$
0.0	1.85 ‰
0.1	1.75 ‰
0.2	1.65 ‰
0.3	1.55 ‰

Variability of lake water $\delta^{44/40}\text{Ca}$, could also be due to the adsorption of Ca^{2+} cations to the negatively charged functional groups on extracellular polymeric substances (EPS) in the water column (Glunk et al., 2011). Isotopic fractionation occurring through sorption in the water column could be estimated using equilibrium fractionation based on the differential bond strength of the Ca^{2+} -aquacomplexes versus the Ca^{2+} -EPS complexes. Through equilibrium fractionation, the heavier Ca isotopes would be concentrated within the Ca^{2+} -EPS complexes and the lighter isotopes would be left in the water, as discussed in the introduction. This would shift the $\delta^{44/40}\text{Ca}$ value of the lake water to lower values. Due to the high amounts of organic matter causing the turbidity within the lake, it is difficult to imagine localization of this process or why it would be more prevalent in the southern sector compared to the northern sector. However, if it is happening throughout the lake, other localized factors could pull the $\delta^{44/40}\text{Ca}$ of the northern sector back up toward seawater values. The tidally influenced water influx to the Northern sector reported by Mann and Nelson (1989) could be bringing in seawater and shifting the delta value of the northern sector back up.

From this discussion of potential $\delta^{44/40}\text{Ca}$ variability within Storr's Lake, I can then consider variability and controlling factors of $\delta^{44/40}\text{Ca}$ in the microbialites. I hypothesized that mineralogy will be a large control on the carbonate $\delta^{44/40}\text{Ca}$ due to the different Ca isotopic fractionation factors in calcite and aragonite (Gussone et al., 2005). To understand the formation of HMC and aragonite within Storr's Lake microbialites, $\delta^{44/40}\text{Ca}$ was measured for two microbialites in detail (WS1 and WN7) and the nearby waters within the lake (as discussed above). Within the carbonates $\delta^{44/40}\text{Ca}$ was strongly negatively correlated with mineralogy (wt% aragonite) as shown in Figure 5-20.

Initial observation of the carbonate $\delta^{44/40}\text{Ca}$ data (Table 5-6), shows the largest difference between carbonates samples is a 0.55‰ difference found between subsamples WS1-1 and WS1-6, which have 28 wt% and 96 wt% aragonite respectively. Gussone et al. (2005) found a 0.6‰ difference between calcite (including 19 mol% Mg HMC) and aragonite in their experiments. However, Gussone et al. (2016a) found a 0.4‰ difference between calcite (including HMC) and aragonite in foraminifera tests, which in combination with variable Sr concentrations, suggests active Ca ion transport or a precursor phase for aragonite precipitation. Due to the appreciable amount of aragonite in WS1-1, the $\delta^{44/40}\text{Ca}$ is lower than if WS1-1 were 100% HMC. Therefore, these two samples are not representative of the system Gussone et al (2005) studied with 0.6‰ difference between pure aragonite and calcite. In WN7, subsamples with 25 wt% and 90 wt% aragonite showed a 0.25‰ difference, which suggests potential differences in Ca isotopic fractionation between microbialites (WS1 vs WN7).

To determine the separate contributions of aragonite and HMC to the bulk carbonate $\delta^{44/40}\text{Ca}$ measured in each sample, I used a simple two end member mixing model (equation 6-5) to calculate the $\delta^{44/40}\text{Ca}$ for HMC and aragonite using algebraic substitutions and pairs of subsamples within the same microbialite. The results of these calculations (Table 6-3), show a ~0.4‰ difference between the aragonite and HMC endmembers calculated for WN7, similar to the difference in foraminifera measured by Gussone et al. (2016a). For WN7-1 and WN7-3 measurements, the pair does not conform to the algebra: WN7-1 has 87 wt% aragonite and $\delta^{44/40}\text{Ca} = 0.56\text{‰}$; where as WN7-3 has 90 wt% aragonite and $\delta^{44/40}\text{Ca} = 0.61\text{‰}$. The two isotopic compositions are too similar and do not follow the assumptions in the model.

$$\delta^{44/40}\text{Ca}_{\text{sample}} = \text{wt}\%_{\text{aragonite}} * \delta^{44/40}\text{Ca}_{\text{aragonite}} + \text{wt}\%_{\text{HMC}} * \delta^{44/40}\text{Ca}_{\text{HMC}}$$

Eq. 6-5

Table 6-3 Results of two endmember mixing for microbialite $\delta^{44/40}\text{Ca}$

$\delta^{44/40}\text{Ca}$ (‰)	Substitution pair					
	WN7-i vs WN7-1	WN7-i vs WN7-3	WN7-ii vs WN7-1	WN7-ii vs WN7-3	WN7-i vs WN7-ii	WS1-1 vs WS1-6
HMC	0.98	0.97	0.98	0.96	0.96	1.16
Aragonite	0.50	0.57	0.50	0.57	0.57	0.35
Difference	0.48	0.40	0.48	0.39	0.39	0.81

Experimental studies have explored the relationship between calcium carbonate fractionation and the Sr distribution coefficient as it relates to precipitation rate in inorganic calcite and aragonite (Tang et al., 2008a, 2012; Alkhatib and Eisenhauer, 2017a, 2017b). Calcium carbonate fractionation can be described as $\Delta^{44/40}\text{Ca}_{s-f} = \delta^{44/40}\text{Ca}_s - \delta^{44/40}\text{Ca}_f$, where “s” stands for solid and “f” stands for fluid. In Storr’s Lake, the solid is the microbialite carbonate and the precipitating fluid is approximated as the nearest lake water sample. Calculated $\Delta^{44/40}\text{Ca}_{\text{carbonate-lake water}}$ for Storr’s Lake are shown in Table 6-4 in addition to estimated $\Delta^{44/40}\text{Ca}_{\text{HMC-lake water}}$ and estimated $\Delta^{44/40}\text{Ca}_{\text{aragonite-lake water}}$ for each microbialite using the mixing model above. Mineralogy specific $\delta^{44/40}\text{Ca}$ for WN7 is averaged from the mixing model results. $\Delta^{44/40}\text{Ca}_{\text{carbonate-lake water}}$ plotted versus the Sr distribution coefficient shows a significant negative correlation (Figure 6-6, $p=0.0125$, $r^2=0.901$). This trend is most likely driven by mineralogy because mineralogy is the primary control on carbonate $\delta^{44/40}\text{Ca}$ and Sr distribution coefficients.

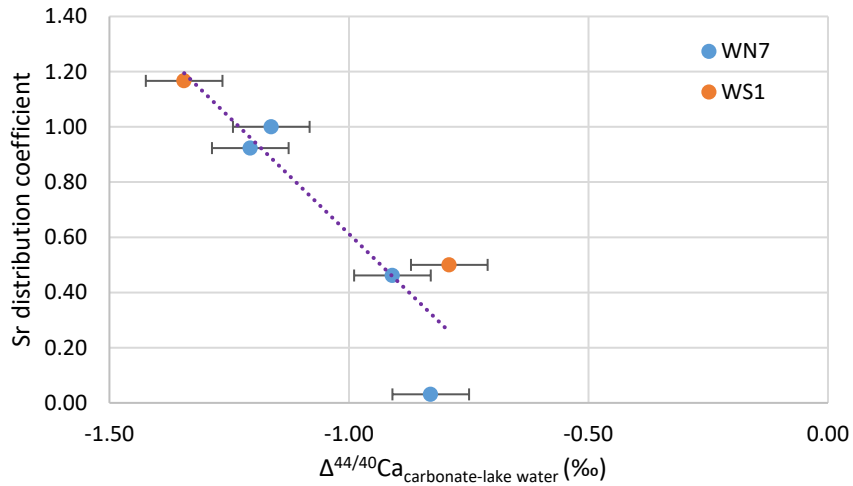


Figure 6-6 Sr distribution coefficient plotted against $\Delta^{44/40}\text{C}_{\text{carbonate-lake water}}$.

Table 6-4 Calculated $\Delta^{44/40}\text{C}_{\text{carbonate-lake water}}$ for WN7 and WS1 including “pure” HMC and aragonite from mixing calculations

Sample name	$\delta^{44/40}\text{Ca}$ carbonate (‰)	Water Sample	$\delta^{44/40}\text{Ca}$ lake water (‰)	$\Delta^{44/40}\text{Ca}$ carbonate-lake water (‰)
Microbialite: WN7				
WN7-i	0.94	WN8-61cm	1.77	-0.83
WN7-ii	0.86		1.77	-0.91
WN7-1	0.56		1.77	-1.21
WN7-3	0.61		1.77	-1.16
<i>WN7 aragonite</i>	0.54		1.77	-1.23
<i>WN7 HMC</i>	0.97		1.77	-0.80
Microbialite: WS1				
WS1-1	0.93	WS1-111cm average	1.73	-0.79
WS1-6	0.38		1.73	-1.34
<i>WS1 aragonite</i>	1.16		1.73	-1.38
<i>WS1 HMC</i>	0.35		1.73	-0.57

For comparison between microbialite heads, the variability in the lake water was normalized by calculating $\Delta^{44/40}\text{C}_{\text{carbonate-lake water}}$ using the lake water sampled from directly above the microbialite head. However, the usage of nearby lake water as the precipitating solution for the whole microbialite assumes that modern lake water $\delta^{44/40}\text{Ca}$ reflects the $\delta^{44/40}\text{Ca}$ of lake water through time. There is no evidence in Storr's Lake reflecting the changes or lack thereof for $\delta^{44/40}\text{Ca}$ within the lake water through time. Given the unexpected variability between lake sectors, there may even be seasonal changes to $\delta^{44/40}\text{Ca}$. Future work should investigate changes in lake water $\delta^{44/40}\text{Ca}$, particularly in the southern sector. Mg and Sr distribution coefficients suggest that the microbialites are open to the lake water throughout precipitation of carbonate, so aragonite is most likely not precipitating from a more isotopically evolved lake water within the pores of the microbialites.

$\Delta^{44/40}\text{C}_{\text{carbonate-lake water}}$ comparison to literature values is used to discuss the biogenic or abiogenic influences on the precipitation of HMC and aragonite within Storr's Lake microbialites. The first comparison is shown in Figure 6-7, where data from this study is compared to inorganic aragonite and calcite samples in addition to one biologically induced mixed carbonate sample measured by Krause et al. (2018). Excluding the data point to the far left of the plot, likely error in the Sr measurement, this plot shows that the microbialite data can be explained by a mixture of inorganic high-Mg calcite and aragonite (thin black line between green calculated line for high-Mg calcite and aragonite data in Figure 6-7). The second comparison is shown in Figure 6-8, with data from this study alongside biogenic aragonite and calcite (Blättler et al., 2012). This

figure shows that the new microbialite data can also be explained by mixing of biogenic aragonite and calcite. Therefore, it cannot be eliminated that the $\Delta^{44/40}\text{Ca}_{\text{carbonate-lake water}}$ records a biogenic signature.

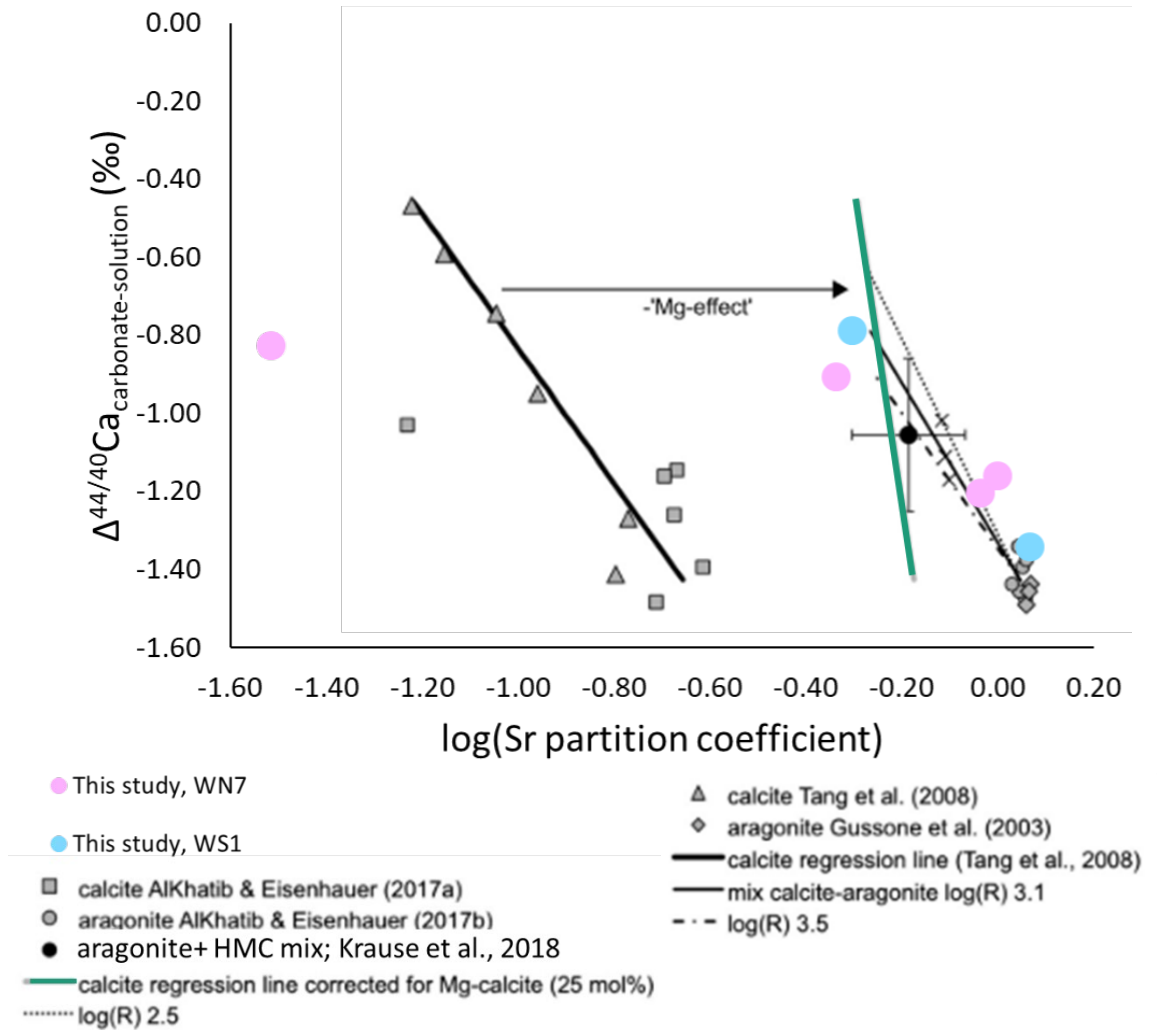


Figure 6-7 Ca isotope values collated by Krause et al. (2018) in combination with data from this study

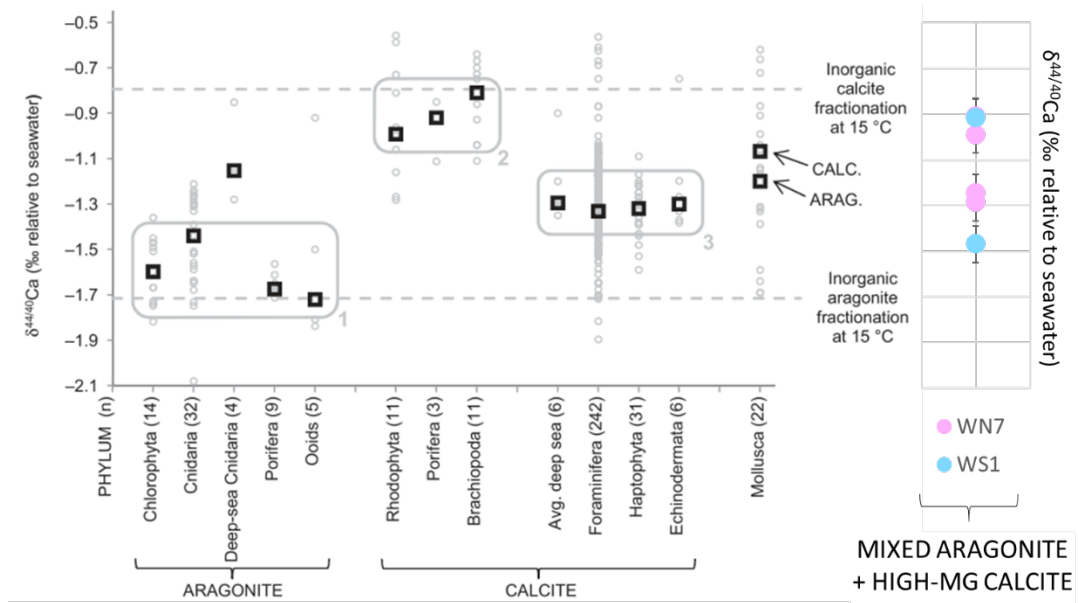


Figure 6-8 Data from Blattler et al. (2012) shows that data from this study falls within a biogenic range of $\delta^{44/40}\text{Ca}$ relative to seawater.

Chapter 7. Conclusions

In this study, I expanded our understanding of microbialites from Storr's Lake through the use of calcium stable isotopes, mineralogy, and elemental analysis. Aragonite was discovered in a majority of the microbialites measured, but seems to only form in water depths greater than 40 cm. This depth dependence on the presence of aragonite suggests that increased accommodation space allows for more heterotrophic activity within the microbialites to modify the chemistry of the micro-environments and promote the crystallization of aragonite.

The use of calcium stable isotopes illuminated previously unknown variability between the two sectors of Storr's Lake. The southern sector seems to have stronger influence of organic matter adsorption of Ca^{2+} in the water column altering its Ca isotopic composition than the northern sector. This variability was shown by a downward shift of the mean $\delta^{44/40}\text{Ca}$ in the southern sector of the lake, away from seawater $\delta^{44/40}\text{Ca}$. On the other hand, the northern sector $\delta^{44/40}\text{Ca}$ follows expectations and was exactly the same as seawater, which is in line with previous measurements of Mg isotopes in Storr's Lake (Li, 2017).

In the microbialites themselves, $\delta^{44/40}\text{Ca}$ was strongly controlled by mineralogy, but the differences between carbonate polymorphs were dissimilar between the two microbialites studied. WN7 recorded a difference of 0.4‰ between high-Mg calcite and

aragonite, whereas WS1 recorded a much larger difference of 0.8‰. More data is needed to speculate on why this difference exists: including better resolution of $\delta^{44/40}\text{Ca}$ within the microbialites and measurement of organic matter concentration within the carbonate.

Contrary to conclusions drawn from $\delta^{26}\text{Mg}$ measurements on the same samples by Li (2017), $\Delta^{44/40}\text{Ca}_{\text{aragonite-lake water}}$ records a potential biogenic signature. This suggests that organic matter within the microbialite is possibly interacting with calcium during precipitation of aragonite. Greer et al. (2015) describes the transformation of HMC to aragonite through changing Mg/Ca ratios within the microenvironment of the microbial mat, where production of aragonite is driven by the consumption of organic matter within the microbialite. Li (2017) suggests that this method should show an inorganic signal in the aragonite, which was consistent with the Mg isotopic composition of the aragonite. However, since Ca is such a universally utilized element, any heterotrophic bacteria consuming organic matter and shifting the microenvironment Mg/Ca ratio could fractionate calcium during its metabolic activities. This fractionation would lend a biogenic signature to the resulting aragonite. Transformation of HMC to aragonite through the consumption of organic matter within the microbialite is still the leading contender for why aragonite forms within Storr's Lake microbialites.

Bibliography

- Alkhatib, M., and Eisenhauer, A., 2017a, Calcium and strontium isotope fractionation during precipitation from aqueous solutions as a function of temperature and reaction rate ; II . Aragonite: *Geochimica et Cosmochimica Acta*, v. 209, p. 320–342, doi:10.1016/j.gca.2017.04.012.
- Alkhatib, M., and Eisenhauer, A., 2017b, Calcium and strontium isotope fractionation in aqueous solutions as a function of temperature and reaction rate ; I . Calcite: *Geochimica et Cosmochimica Acta*, v. 209, p. 296–319, doi:10.1016/j.gca.2016.09.035.
- Althoff, P.L., 1977, Structural refinement of dolomite and a magnesian calcite and implications for dolomite formation in the marine environment: *American Mineralogist*, v. 62, p. 772–783.
- Arp, G., Reimer, A., and Reitner, J., 2001, Photosynthesis-induced biofilm calcification and calcium concentrations in phanerozoic oceans: *Science*, v. 292, p. 1701–1704.
- Beniash, E., 2011, Biominerals-hierarchical nanocomposites: The example of bone: *Wiley Interdisciplinary Reviews: Nanomedicine and Nanobiotechnology*, v. 3, p. 47–69, doi:10.1002/wnan.105.
- Blättler, C.L., Henderson, G.M., and Jenkyns, H.C., 2012, Explaining the phanerozoic Ca isotope history of seawater: *Geology*, v. 40, p. 843–846, doi:10.1130/G33191.1.
- Boggs, S.J., 2006, *Principles of Sedimentology and Stratigraphy: Upper Saddle River, NJ, Pearson Prentice Hall*, 1–662 p.
- Boulyga, S.F., 2010, Calcium Isotope Analysis by Mass Spectrometry: *Mass Spectrometry Reviews*, v. 29, p. 685–716, doi:10.1002/mas.
- Bowlin, E.M., Klaus, J.S., Foster, J.S., Andres, M.S., Custals, L., and Reid, R.P., 2012, Environmental controls on microbial community cycling in modern marine stromatolites: *Sedimentary Geology*, v. 263–264, p. 45–55, doi:10.1016/j.sedgeo.2011.08.002.
- Braga, J.C., Martin, J.M., and Riding, R., 1995, Controls on Microbial Dome Fabric Development along a Carbonate-Siliciclastic Shelf-Basin: *PALAIOS*, v. 10, p. 347–361, <https://www.jstor.org/stable/3515160> (accessed January 2020).
- Braissant, O., Decho, A.W., Dupraz, C., Glunk, C., Przekop, K.M., and Visscher, P.T., 2007, Exopolymeric substances of sulfate-reducing bacteria: Interactions with calcium at alkaline pH and implication for formation of carbonate minerals:

Geobiology, doi:10.1111/j.1472-4669.2007.00117.x.

- Brake, S.S., Hasiotis, S.T., Dannelly, H.K., and Connors, K.A., 2002, Eukaryotic stromatolite builders in acid mine drainage: Implications for Precambrian iron formations and oxygenation of the atmosphere? *Geology*, v. 30, p. 599–602, <https://pubs.geoscienceworld.org/gsa/geology/article-pdf/30/7/599/3523485/i0091-7613-30-7-599.pdf>.
- Brigmon, R.L., Morris, P., and Smith, G., 2008, Evaporite Microbial Films, Mats, Microbialites and Stomatolite, *in* Dilek, Y., Furnes, H., and Muehlenbachs, K. eds., *Links Between Geological Processes, Microbial Activities & Evolution of Life*, Springer Science+Business Media B.V., p. 197–235.
- Buongiorno, J., Gomez, F.J., Fike, D.A., and Kah, L.C., 2019, Mineralized microbialites as archives of environmental evolution, Laguna Negra, Catamarca Province, Argentina: *Geobiology*, v. 17, p. gbi.12327, doi:10.1111/gbi.12327.
- Burne, R. V, and Moore, L.S., 1987, Microbialites: Organosedimentary Deposits of Benthic Microbial Communities: *PALAOIS*, v. 2, p. 241–254, <http://www.jstor.org/stable/3514674>.
- Choudhuri, A., Sarkar, S., Altermann, W., Mukhopadhyay, S., and Bose, P.K., 2016, Lakshanhatti stromatolite, India: Biogenic or abiogenic? *Journal of Palaeogeography*, v. 5, p. 292–310, doi:10.1016/j.jop.2016.05.006.
- Curran, H.A., 1997, Introduction to the Geology of the Bahamas and San Salvador Island, With an Overflight Guide, *in* Curran, H.A. ed., *Guide to Bahamian Ichnology: Pleistocene, Holocene, and Modern Environments*, San Salvador, Bahamas, Bahamian Field Station, p. 1–10.
- Dupraz, C., Fowler, A., Tobias, C., and Visscher, P.T., 2013, Stromatolitic knobs in Storr 's Lake (San Salvador , Bahamas): a model system for formation and alteration of laminae: *Geobiology*, p. 527–548, doi:10.1111/gbi.12063.
- Dupraz, C., Reid, R.P., Braissant, O., Decho, A.W., Norman, R.S., and Visscher, P.T., 2009, Processes of carbonate precipitation in modern microbial mats: *Earth-Science Reviews*, v. 96, p. 141–162, doi:10.1016/j.earscirev.2008.10.005.
- Dupraz, C., Reid, R.P., and Visscher, P.T., 2011, Microbialites, *Modern: Encyclopedia of Geobiology*, p. 617–635.
- Dupraz, C., and Visscher, P.T., 2005, Microbial lithification in marine stromatolites and hypersaline mats: *Trends in Microbiology*, v. 13, p. 429–438, doi:10.1016/j.tim.2005.07.008.

- Dupraz, C., Visscher, P.T., Baumgartner, L.K., and Reid, R.P., 2004, Microbe-mineral interactions: Early carbonate precipitation in a hypersaline lake (Eleuthera Island, Bahamas): *Sedimentology*, v. 51, p. 745–765, doi:10.1111/j.1365-3091.2004.00649.x.
- Fantle, M.S., and Depaolo, D.J., 2007, Ca isotopes in carbonate sediment and pore fluid from ODP Site 807A : The $\text{Ca}^{2+}(\text{aq})$ – calcite equilibrium fractionation factor and calcite recrystallization rates in Pleistocene sediments: *Geochimica et Cosmochimica Acta*, v. 71, p. 2524–2546, doi:10.1016/j.gca.2007.03.006.
- Fantle, M.S., and Tipper, E.T., 2014, Calcium isotopes in the global biogeochemical Ca cycle: Implications for development of a Ca isotope proxy: *Earth-Science Reviews*, v. 129, p. 148–177, doi:10.1016/j.earscirev.2013.10.004.
- Farkaš, J., Böhm, F., Wallmann, K., Blenkinsop, J., Eisenhauer, A., Geldern, R. van, Munnecke, A., Voigt, S., and Veizer, J., 2007a, Calcium isotope record of Phanerozoic oceans : Implications for chemical evolution of seawater and its causative mechanisms: *Geochimica et Cosmochimica Acta*, v. 71, p. 5117–5134, doi:10.1016/j.gca.2007.09.004.
- Farkaš, J., Buhl, D., Blenkinsop, J., and Veizer, J., 2007b, Evolution of the oceanic calcium cycle during the late Mesozoic: Evidence from $\delta^{44}/^{40}\text{Ca}$ of marine skeletal carbonates: *Earth and Planetary Science Letters*, v. 253, p. 96–111, doi:10.1016/j.epsl.2006.10.015.
- Faure, G., and Mensing, T.M., 2005, *Isotopes Principles and Applications*: Hoboken, New Jersey, John Wiley & Sons, Inc.
- Finch, A.A., and Allison, N., 2008, Mg structural state in coral aragonite and implications for the paleoenvironmental proxy: *Geophysical Research Letters*, v. 35, p. 1–5, doi:10.1029/2008GL033543.
- Foster, J.S., and Green, S.J., 2011, Microbial Diversity in Modern Stromatolites, *in* Tewari, V.C. and Seckbach, J. eds., *STROMATOLITES: Interaction of Microbes with Sediments*, Springer Science, v. 18, p. 385–405, doi:10.1007/978-94-007-0397-1.
- Gabitov, R.I., Sadekov, A., and Leinweber, A., 2014, Crystal growth rate effect on Mg/Ca and Sr/Ca partitioning between calcite and fluid: An in situ approach: *Chemical Geology*, v. 367, p. 70–82, doi:10.1016/j.chemgeo.2013.12.019.
- Gamble, D.W., and Jordan, R.D., 2004, Spatial Variability of Precipitation of San Salvador, Bahamas 2001-2003, *in* The 12th Symposium on the Geology of the Bahamas and other Carbonate Regions, Gerace Research Centre, San Salvador, Bahamas, Gerace Research Centre, p. 52–60.

- Giri, S.J., Swart, P.K., and Devlin, Q.B., 2018, The effect of changing seawater Ca and Mg concentrations upon the distribution coefficients of Mg and Sr in the skeletons of the scleractinian coral *Pocillopora damicornis*: *Geochimica et Cosmochimica Acta*, v. 222, p. 535–549, doi:10.1016/j.gca.2017.11.011.
- Glunk, C., Dupraz, C., Braissant, O., Gallagher, K.L., Verrecchia, E.P., and Visscher, P.T., 2011, Microbially mediated carbonate precipitation in a hypersaline lake, Big Pond (Eleuthera, Bahamas): *Sedimentology*, v. 58, p. 720–736, doi:10.1111/j.1365-3091.2010.01180.x.
- Greer, H.F., Zhou, W., and Guo, L., 2015, Phase transformation of Mg-calcite to aragonite in active-forming hot spring travertines: , p. 453–462, doi:10.1007/s00710-015-0367-5.
- Griffith, E.M., Paytan, A., Caldeira, K., Bullen, T.D., and Thomas, E., 2008, A Dynamic Marine Calcium Cycle During the Past 28 Million Years: *Science*, v. 322, p. 1671–1674, doi:10.1126/science.1163614.
- Gussone, N., Böhm, F., Eisenhauer, A., Dietzel, M., Heuser, A., Teichert, B.M.A., Reitner, J., Wörheide, G., and Dullo, W.C., 2005, Calcium isotope fractionation in calcite and aragonite: *Geochimica et Cosmochimica Acta*, v. 69, p. 4485–4494, doi:10.1016/j.gca.2005.06.003.
- Gussone, N., Eisenhauer, A., Heuser, A., Dietzel, M., Bock, B., Böhm, F., Spero, H.J., Lea, D.W., Bijma, J., and Nägler, T.F., 2003, Model for kinetic effects on calcium isotope fractionation ($\delta^{44}\text{Ca}$) in inorganic aragonite and cultured planktonic foraminifera: *Geochimica et Cosmochimica Acta*, v. 67, p. 1375–1382, doi:10.1016/S0016-7037(02)01296-6.
- Gussone, N., Filipsson, H.L., and Kuhnert, H., 2016a, Mg/Ca, Sr/Ca and Ca isotope ratios in benthonic foraminifers related to test structure, mineralogy and environmental controls: *Geochimica et Cosmochimica Acta*, v. 173, p. 142–159, doi:10.1016/j.gca.2015.10.018.
- Gussone, N., Schmitt, A.D., Heuser, A., Wombacher, F., Dietzel, M., Tipper, E.T., and Schiller, M., 2016b, Calcium Stable Isotope Geochemistry (J. Hoefs, Ed.): Springer, doi:10.1007/978-3-540-68953-9_6.
- Harouaka, K., Kubicki, J.D., and Fantle, M.S., 2017, Effect of amino acids on the precipitation kinetics and Ca isotopic composition of gypsum: *Geochimica et Cosmochimica Acta*, p. 343–364, doi:10.1016/j.gca.2017.09.010.
- Harouaka, K., Mansor, M., Macalady, J.L., and Fantle, M.S., 2016, Calcium isotopic fractionation in microbially mediated gypsum precipitates: *Geochimica et Cosmochimica Acta*, v. 184, p. 114–131, doi:10.1016/j.gca.2016.03.003.

- Harvey, D., 2016, Analytical Chemistry: Creative Commons, http://dpuadweb.depauw.edu/harvey_web/eTextProject/AnalyticalChemistry2.0.html.
- Heuser, A., and Eisenhauer, A., 2008, The calcium isotope composition ($\delta^{44}\text{Ca}$) of NIST SRM 915b and NIST SRM 1486: Geostandards and Geoanalytical Research, v. 32, p. 311–315, doi:10.1111/j.1751-908X.2008.00877.x.
- Heuser, A., Eisenhauer, A., Gussone, N., Bock, B., Hansen, B.T., and Nögler, T.F., 2002, Measurement of calcium isotopes ($\delta^{44}\text{Ca}$) using a multicollector TIMS technique: International Journal of Mass Spectrometry, v. 220, p. 385–397, doi:10.1016/S1387-3806(02)00838-2.
- Heuser, A., Schmitt, A.-D., Gussone, N., and Wombacher, F., 2016, Analytical Methods, in Calcium Stable Isotope Geochemistry, p. 23–73, doi:10.1007/978-3-540-68953-9.
- Hindshaw, R.S., Reynolds, B.C., Wiederhold, J.G., Kretzschmar, R., and Bourdon, B., 2011, Calcium isotopes in a proglacial weathering environment: Damma glacier, Switzerland: Geochimica et Cosmochimica Acta, doi:10.1016/j.gca.2010.09.038.
- Hippler, D., Schmitt, A.D., Gussone, N., Heuser, A., Stille, P., Eisenhauer, A., and Nögler, T.F., 2003, Calcium isotopic composition of various reference materials and seawater: Geostandards Newsletter, v. 27, p. 13–19, doi:10.1111/j.1751-908X.2003.tb00709.x.
- Hoffman, P., 1976, Stromatolite Morphogenesis in Shark Bay, Western Australia, in Walter, M.R. ed., Developments in Sedimentology, Elsevier, p. 261–271, doi:10.1016/S0070-4571(08)71139-7.
- Holmden, C., and Bélanger, N., 2010, Ca isotope cycling in a forested ecosystem: Geochimica et Cosmochimica Acta, v. 74, p. 995–1015, doi:10.1016/j.gca.2009.10.020.
- Holmden, C., Papanastassiou, D.A., Blanchon, P., and Evans, S., 2012, $\delta^{44}\text{Ca}$ variability in shallow water carbonates and the impact of submarine groundwater discharge on Ca-cycling in marine environments: Geochimica et Cosmochimica Acta, v. 83, p. 179–194, doi:10.1016/j.gca.2011.12.031.
- Jarosch, D., and Heger, G., 1986, Neutron diffraction refinement of the crystal structure of aragonite: TMPM Tscherms Mineralogische und Petrographische Mitteilungen, v. 35, p. 127–131, doi:10.1007/BF01140844.
- Krause, S., Liebetrau, V., Gorb, S., Sánchez-Román, M., McKenzie, J.A., and Treude, T., 2012, Microbial nucleation of Mg-rich dolomite in exopolymeric substances under anoxic modern seawater salinity: New insight into an old enigma: Geology, v. 40, p.

587–590, doi:10.1130/G32923.1.

- Krause, S., Liebetrau, V., Löscher, C.R., Böhm, F., Gorb, S., Eisenhauer, A., and Treude, T., 2018, Marine ammonification and carbonic anhydrase activity induce rapid calcium carbonate precipitation: *Geochimica et Cosmochimica Acta*, doi:10.1016/j.gca.2018.09.018.
- Lehn, G.O., Jacobson, A.D., and Holmden, C., 2013, Precise analysis of Ca isotope ratios ($\delta^{44}/^{40}\text{Ca}$) using an optimized ^{43}Ca - ^{42}Ca double-spike MC-TIMS method: *International Journal of Mass Spectrometry*, v. 351, p. 69–75, doi:10.1016/j.ijms.2013.06.013.
- Lehn, J.M., and Sauvage, J.P., 1975, [2]-Cryptates: Stability and Selectivity of Alkali and Alkaline-Earth Macrobicyclic Complexes: *Journal of the American Chemical Society*, v. 97, p. 6700–6707, doi:10.1021/ja00856a018.
- Lemarchand, D., Wasserburg, G., and Papanastassiou, D.A., 2004, Rate-controlled calcium isotope fractionation in synthetic calcite: *Geochimica et Cosmochimica Acta*, v. 68, p. 4665–4678, doi:10.1016/j.gca.2004.05.029.
- Li, Z., 2017, Mg Isotope Investigation of Stromatolitic Knobs in Storr's Lake, San Salvador, Bahamas: Implications for Organomineralization and Laminae Formation: University of Texas Arlington, 399–404 p.
- Long, X., Ma, Y., and Qi, L., 2014, Biogenic and synthetic high magnesium calcite - A review: *Journal of Structural Biology*, v. 185, p. 1–14, doi:10.1016/j.jsb.2013.11.004.
- Loste, E., Wilson, R.M., Seshadri, R., and Meldrum, F.C., 2003, The role of magnesium in stabilising amorphous calcium carbonate and controlling calcite morphologies: *Journal of Crystal Growth*, v. 254, p. 206–218, doi:10.1016/S0022-0248(03)01153-9.
- MacKinder, L., Wheeler, G., Schroeder, D., von Dassow, P., Riebesell, U., and Brownlee, C., 2011, Expression of biomineralization-related ion transport genes in *Emiliana huxleyi*: *Environmental Microbiology*, v. 13, p. 3250–3265, doi:10.1111/j.1462-2920.2011.02561.x.
- Mann, C.J., and Nelson, W.M., 1989, Microbialitic Structures in Storr's Lake, San Salvador Island, Bahama Islands: *Palaios*, v. 4, p. 287–293, doi:10.2307/3514777.
- Martin, J.B., and Moore, P.J., 2008, Sr concentrations and isotope ratios as tracers of ground-water circulation in carbonate platforms: Examples from San Salvador Island and Long Island, Bahamas: *Chemical Geology*, v. 249, p. 52–65, doi:10.1016/j.chemgeo.2007.11.009.

- Millero, F.J., 1995, Thermodynamics of the carbon dioxide system in the oceans: *Geochimica et Cosmochimica Acta*, v. 59, p. 661–677, doi:10.1016/0016-7037(94)00354-O.
- Mondal, S., and Chakrabarti, R., 2018, A novel sample loading method and protocol for monitoring sample fractionation for high precision Ca stable isotope ratio measurements using double-spike TIMS: *Journal of Analytical Atomic Spectrometry*, v. 33, p. 141–150, doi:10.1039/c7ja00322f.
- Morgan, J.L., Gordon, G.W., Arrua, R.C., Skulan, J.L., Anbar, A.D., and Bullen, T.D., 2011, High-Precision Measurement of Variations in Calcium Isotope Ratios in Urine by Multiple Collector Inductively Coupled Plasma Mass Spectrometry: *Anal. Chem.*, v. 83, p. 6956–6962, doi:10.1021/ac200361t.
- Mylroie, J.E., and Carew, J.L., 1995, GEOLOGY AND KARST GEOMORPHOLOGY OF SAN SALVADOR ISLAND, BAHAMAS: *Carbonates and Evaporites*, v. 10, p. 193–206.
- Neumann, C.A., Bebout, B.M., McNeese, L.R., Paull, C.K., and Paerl, H.A., 1989, Modern Stromatolites and Associated Mats: San Salvador, Bahamas, *in* Mylroie, J.E. ed., *The Fourth Symposium on the Geology of the Bahamas*, Bahamian Field Station.
- Nightingale, E.R., 1959, Phenomenological theory of ion solvation. Effective radii of hydrated ions: *Journal of Physical Chemistry*, v. 63, p. 1381–1387, doi:10.1021/j150579a011.
- Park Boush, L.E., Myrbo, A., and Michelson, A., 2014, A qualitative and quantitative model for climate-driven lake formation on carbonate platforms based on examples from the Bahamian archipelago: *Carbonates and Evaporites*, v. 29, p. 409–418, doi:10.1007/s13146-014-0221-6.
- Paul, V.G., Wronkiewicz, D.J., Mormile, M.R., and Foster, J.S., 2016, Mineralogy and Microbial Diversity of the Microbialites in the Hypersaline Storr’s Lake, the Bahamas: *Astrobiology*, v. 16, p. 282–300, doi:10.1089/ast.2015.1326.
- Paull, C.K., Fullagar, P.D., Bralower, T.J., and Rohl, U., 1995, Seawater ventilation of mid-Pacific guyots drilled during Leg 143, *in* Winterer, E.L., Sager, W.W., Firth, J. V., and Sinton, J.M. eds., *Proceedings of the Ocean Drilling Program, Scientific Results*, v. 143, p. 231–241, doi:10.2973/odp.proc.sr.143.222.1995.
- Paull, C.K., Neumann, A.C., Bebout, B., Zabielski, V., and Showers, W., 1992, Growth rate and stable isotopic character of modern stromatolites from San Salvador, Bahamas: *Palaeogeography, Palaeoclimatology, Palaeoecology*, v. 95, p. 335–344.

- Perry, R.S. et al., 2007, Defining biominerals and organominerals: Direct and indirect indicators of life: *Sedimentary Geology*, v. 201, p. 157–179, doi:10.1016/j.sedgeo.2007.05.014.
- Pinckney, J., Paerl, H.W., and Bebout, B.M., 1995, Salinity control of benthic microbial mat community production in a Bahamian hypersaline lagoon: *Journal of Experimental Marine Biology and Ecology*, v. 187, p. 223–237, doi:10.1016/0022-0981(94)00185-G.
- Pokroy, B., Fieramosca, J.S., Von Dreele, R.B., Fitch, A.N., Caspi, E.N., and Zolotoyabko, E., 2007, Atomic structure of biogenic aragonite: *Chemistry of Materials*, v. 19, p. 3244–3251, doi:10.1021/cm070187u.
- Reid, R.P., Foster, J.S., Radtke, G., and Golubic, S., 2011, Modern Marine Stromatolites of Little Darby Island, Exuma Archipelago, Bahamas: Environmental Setting, Accretion Mechanisms and Role of Euendoliths, *in* Reitner, J., Quéric, N.-V., and Arp, G. eds., *Advances in Stromatolite Geobiology*, Verlag Berlin Heidelberg, Springer, p. 77–89.
- Riding, R., 2011a, Microbialites, stromatolites, and thrombolites: *Encyclopedia of Geobiology*, p. 635–654, doi:10.1007/978-1-4020-9212-1.
- Riding, R., 2011b, Microbialites , stromatolites , and thrombolites . In J . Reitner and V . Thiel (eds),: *Encyclopedia, Geobiology Series*, Science, p. 635–654, doi:10.1007/978-1-4020-9212-1.
- Riding, R., 2011c, The Nature of Stromatolites: 3,500 Million Years of History and a Century of Research, *in* Reitner, J., Quéric, N.-V., and Arp, G. eds., *Advances in Stromatolite Geobiology*, Verlag Berlin Heidelberg, Springer, doi:10.1007/978-3-642-10415-2.
- Russell, M.J., Ingham, J.K., Zedef, V., Maktav, D., Sunar, F., Hall, A.J., and Fallick, A.E., 1999, Search for signs of ancient life on Mars: expectations from hydromagnesite microbialites, Salda Lake, Turkey: *Journal of the Geological Society*, London, v. 156, p. 869–888.
- Russell, W.A., Papanastassiou, D.A., and Tombrello, T.A., 1978, Ca isotope fractionation on the Earth and other solar system materials: *Geochimica et Cosmochimica Acta*, v. 42, p. 1075–1090, doi:10.1016/0016-7037(78)90105-9.
- Schulting, R., Richards, M., Pouncett, J., Manco, B.N., Freid, E., and Ostapkowicz, J., 2018, Absence of Saharan dust influence on the strontium isotope ratios on modern trees from the Bahamas and Turks and Caicos Islands: *Quaternary Research*, v. 89, p. 394–412, doi:10.1017/qua.2018.8.

- Shahar, A., Elardo, S.M., and Macris, C.A., 2017, Equilibrium Fractionation of Non-traditional Stable Isotopes: an Experimental Perspective: *Reviews in Mineralogy and Geochemistry*, v. 82, p. 65–83, doi:10.2138/rmg.2017.82.3.
- Sharp, Z.D., 2017, *Principles of Stable Isotope Geochemistry*, 2nd Edition:, doi:<https://doi.org/10.25844/h9q1-0p82>.
- Sipahioglu, S.M., 2008, Tracking Storms through Time: Event Deposition and Biologic Response in Storr's Lake, San Salvador Island, Bahamas:, http://rave.ohiolink.edu/etdc/view?acc_num=akron1227031927 (accessed December 2019).
- Skulan, J., DePaolo, D.J., and Owens, T.L., 1997, Biological control of calcium isotopic abundances in the global calcium cycle: *Geochimica et Cosmochimica Acta*, v. 61, p. 2505–2510, doi:10.1016/S0016-7037(97)00047-1.
- Smith, B.N., and Ziegler, H., 1990, Isotopic Fractionation of Hydrogen in Plants: *Botanica Acta*, v. 103, p. 335–342, doi:10.1111/j.1438-8677.1990.tb00171.x.
- Stumm, W., and Morgan, J.J., 1996, *Aquatic Chemistry*: New York, John Wiley & Sons, 1022p p.
- Tang, J., Dietzel, M., Böhm, F., Köhler, S.J., and Eisenhauer, A., 2008a, Sr²⁺/Ca²⁺ and ⁴⁴Ca/⁴⁰Ca fractionation during inorganic calcite formation: II. Ca isotopes: *Geochimica et Cosmochimica Acta*, doi:10.1016/j.gca.2008.05.033.
- Tang, J., Köhler, S.J., and Dietzel, M., 2008b, Sr²⁺/Ca²⁺ and ⁴⁴Ca/⁴⁰Ca fractionation during inorganic calcite formation: I. Sr incorporation: *Geochimica et Cosmochimica Acta*, doi:10.1016/j.gca.2008.05.031.
- Tang, J., Niedermayr, A., Köhler, S.J., Böhm, F., Kisakurek, B., Eisenhauer, A., and Dietzel, M., 2012, Sr²⁺/Ca²⁺ and ⁴⁴Ca/⁴⁰Ca fractionation during inorganic calcite formation: III. Impact of salinity / ionic strength: *Geochimica et Cosmochimica Acta*, v. 77, p. 432–443, doi:10.1016/j.gca.2011.10.039.
- Wang, W., Qin, T., Zhou, C., Huang, S., Wu, Z., and Huang, F., 2017, Concentration effect on equilibrium fractionation of Mg-Ca isotopes in carbonate minerals: Insights from first-principles calculations: *Geochimica et Cosmochimica Acta*, v. 208, p. 185–197, doi:10.1016/j.gca.2017.03.023.
- Wassenburg, J.A. et al., 2016, Determination of aragonite trace element distribution coefficients from speleothem calcite–aragonite transitions: *Geochimica et Cosmochimica Acta*, v. 190, p. 347–367, doi:10.1016/j.gca.2016.06.036.
- Wombacher, F., Eisenhauer, A., Böhm, F., Gussone, N., Regenber, M., Dullo, W.C.,

and Rüggeberg, A., 2011, Magnesium stable isotope fractionation in marine biogenic calcite and aragonite: *Geochimica et Cosmochimica Acta*, v. 75, p. 5797–5818, doi:10.1016/j.gca.2011.07.017.

Young, E.D., Galy, A., and Nagahara, H., 2002, Kinetic and equilibrium mass-dependent isotope fractionation laws in nature and their geochemical and cosmochemical significance: *Geochimica et Cosmochimica Acta*, v. 66, p. 1095–1104, doi:10.1016/S0016-7037(01)00832-8.

Zabielski, V.P., 1991, *The Depositional History of Storr's Lake San Salvador, Bahamas*: University of North Carolina at Chapel Hill, 1–107 p.

Appendix A. X-Ray Diffraction Spectra

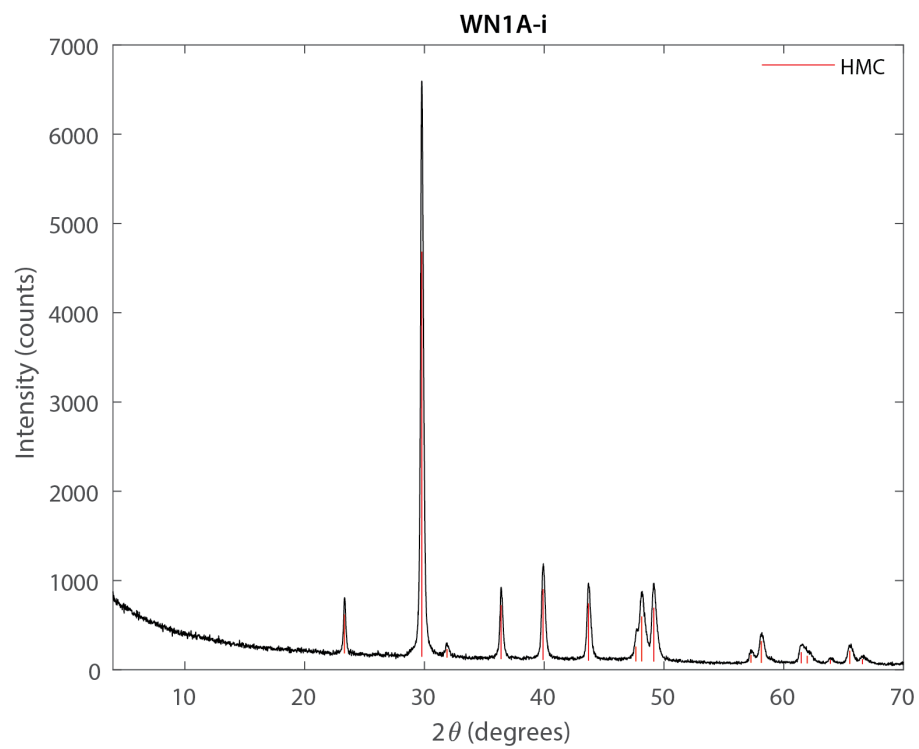


Figure A-1 WN1A-i XRD Spectra

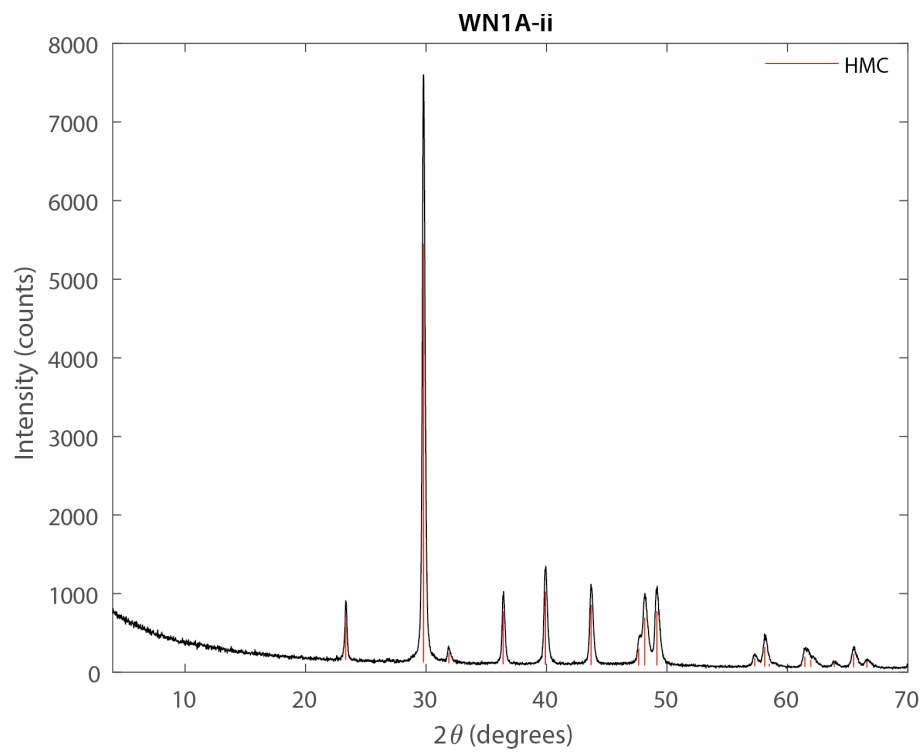


Figure A-2 WN1A-ii XRD Spectra

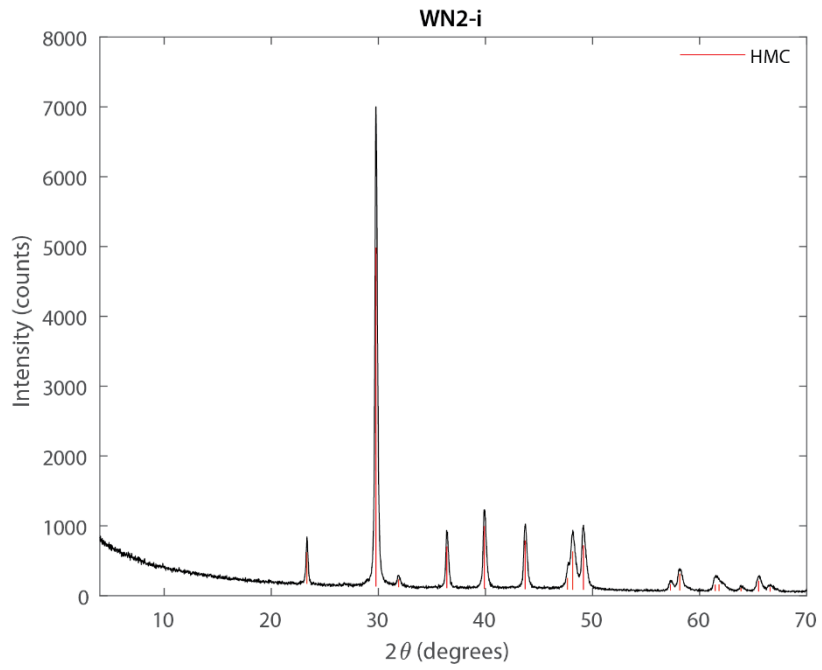


Figure A-3 WN2-i XRD spectra.

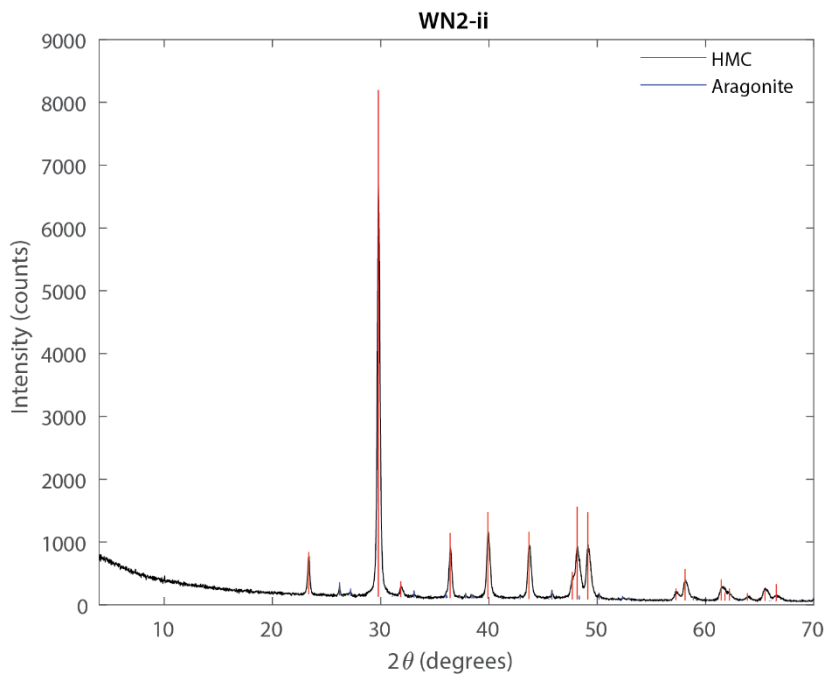


Figure A-4 WN2-ii XRD Spectra

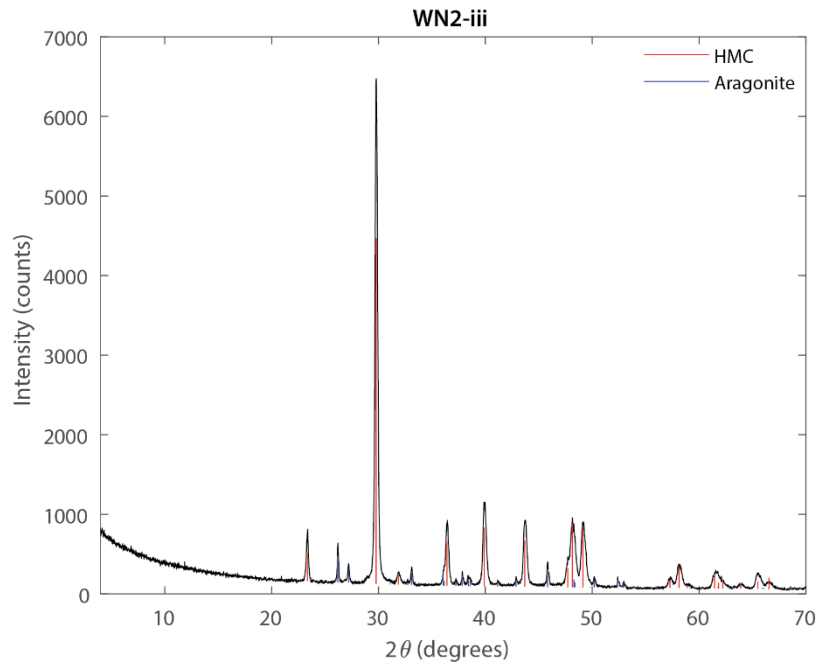


Figure A-5 WN2-iii XRD Spectra

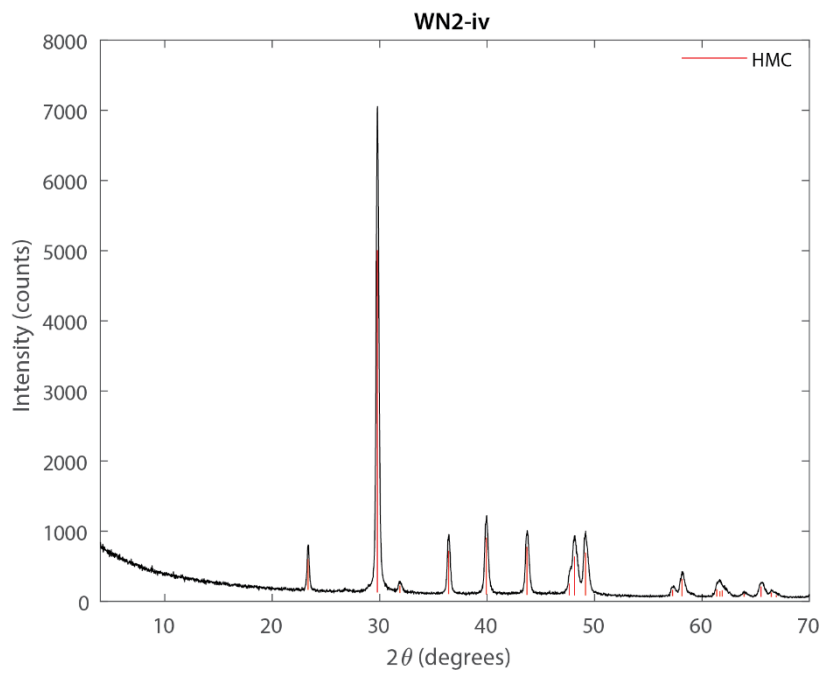


Figure A-6 WN2-iv XRD Spectra

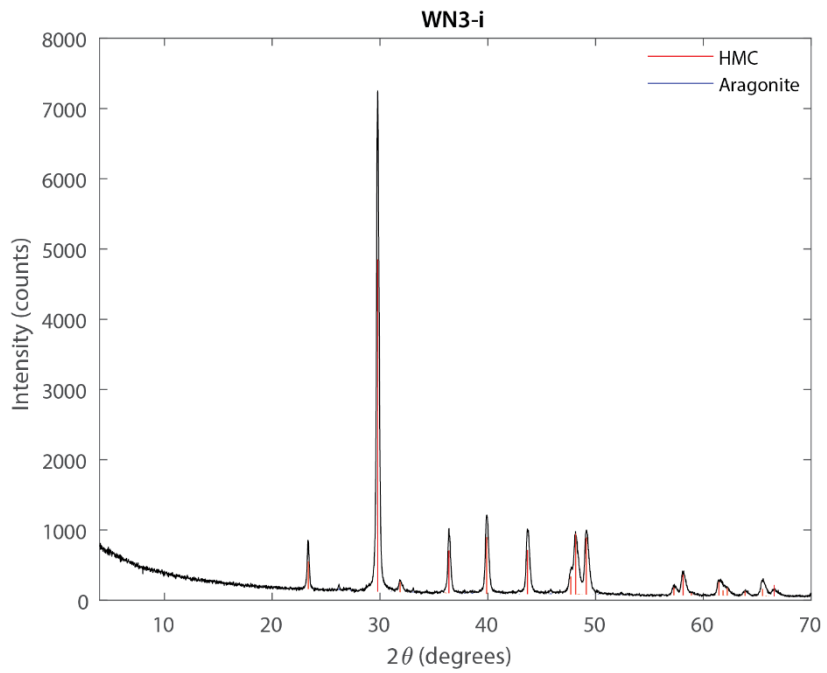


Figure A-5 WN3-i XRD Spectra

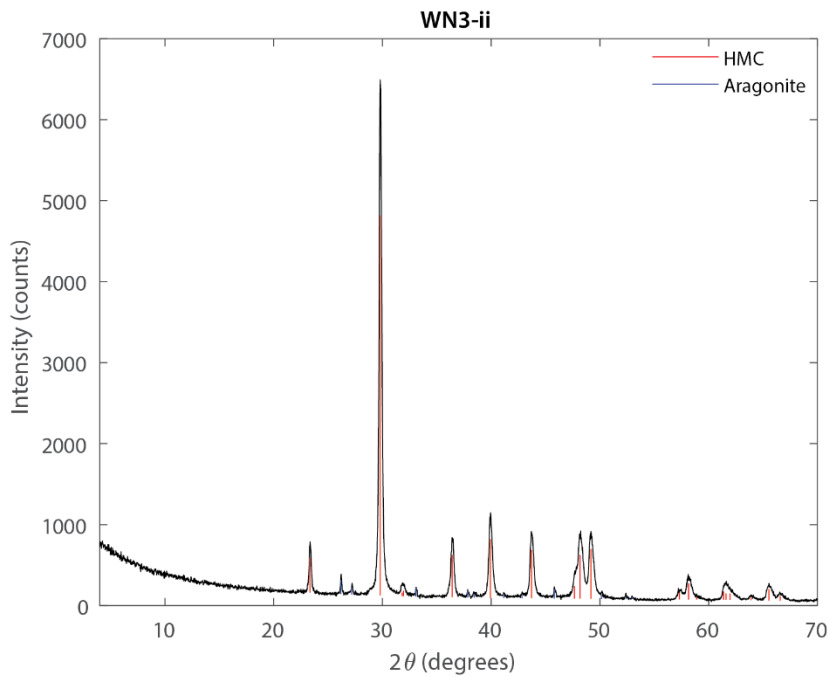


Figure A-6 WN3-ii XRD Spectra

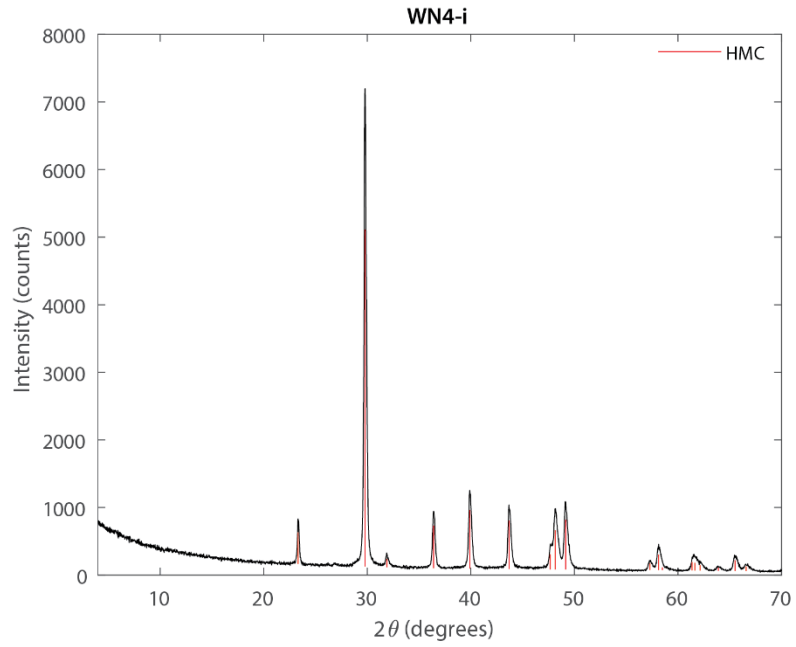


Figure A-7 WN4-i XRD Spectra

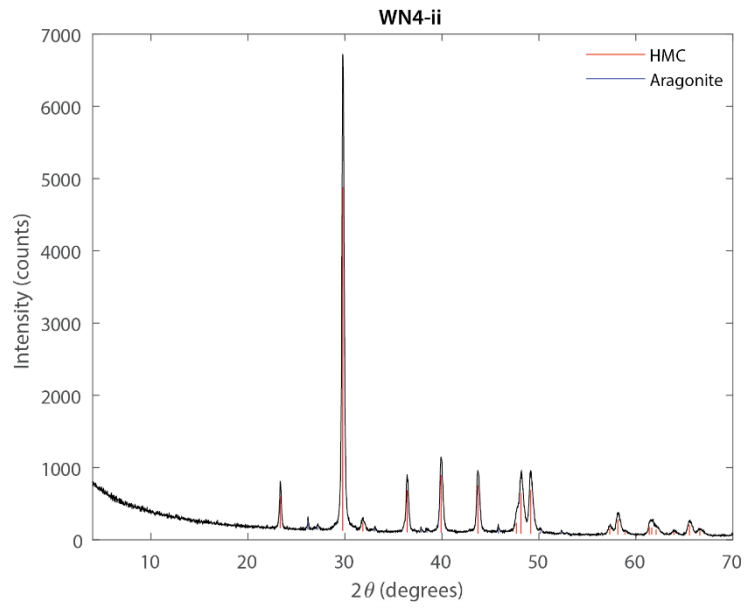


Figure A-8 WN4-ii XRD Spectra

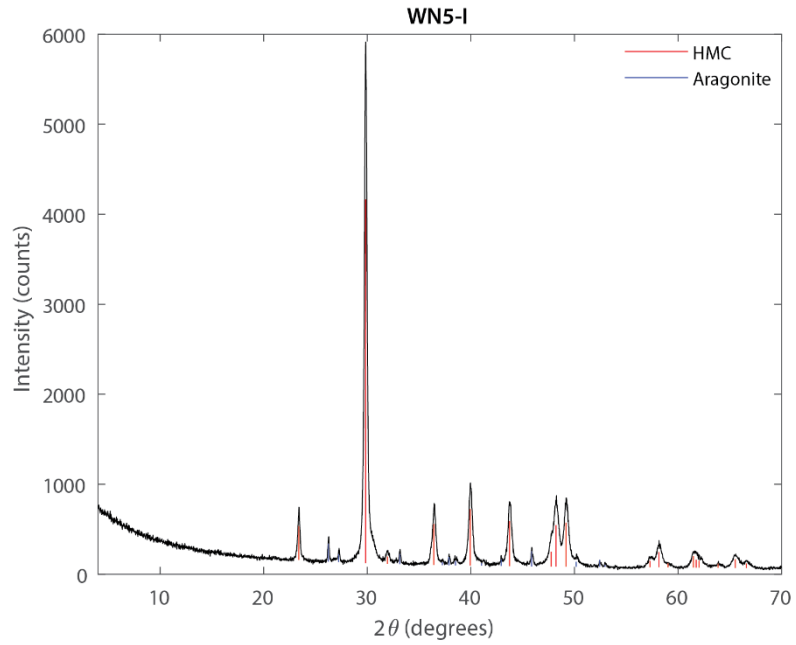


Figure A-9 WN5-I XRD Spectra

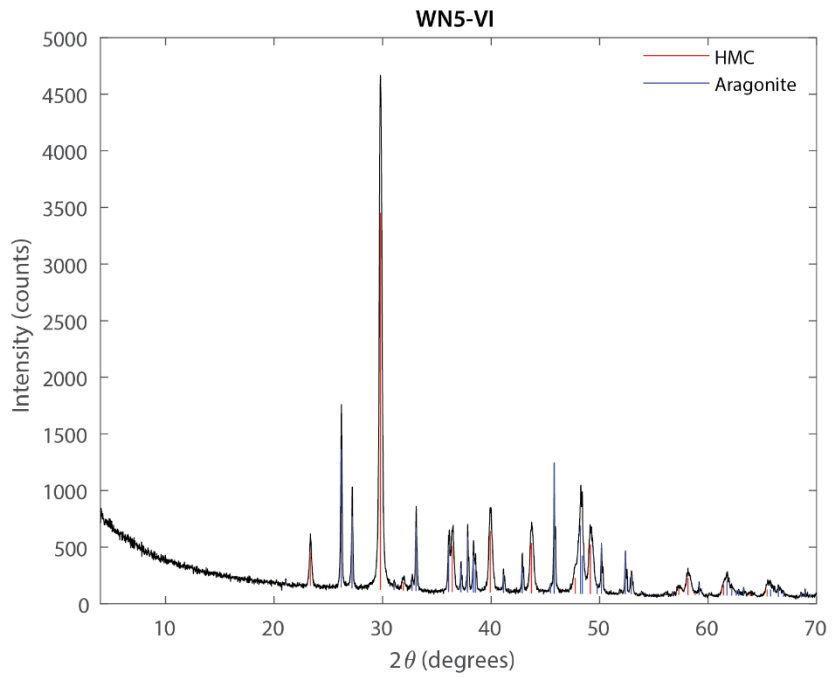


Figure A-10 WN5-VI XRD Spectra

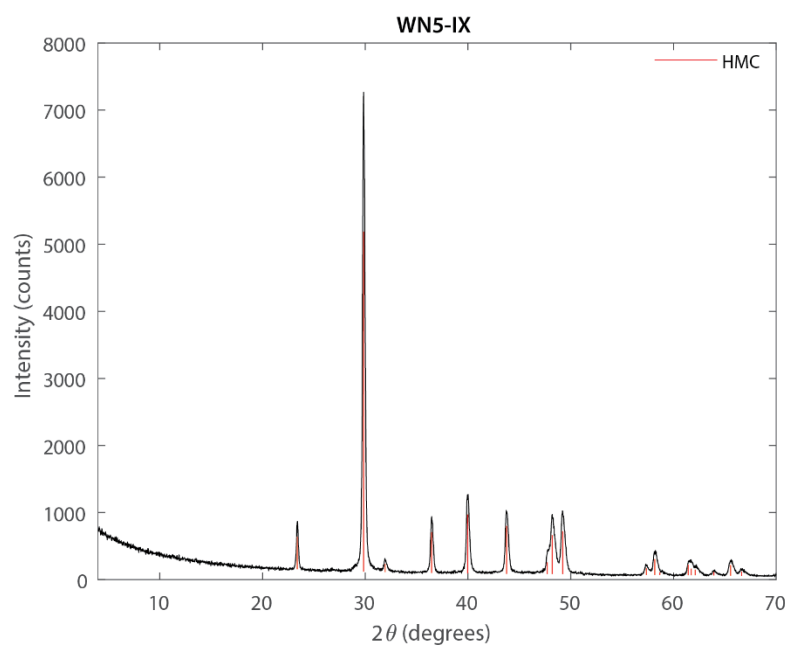


Figure A-11 WN5-IX XRD Spectra

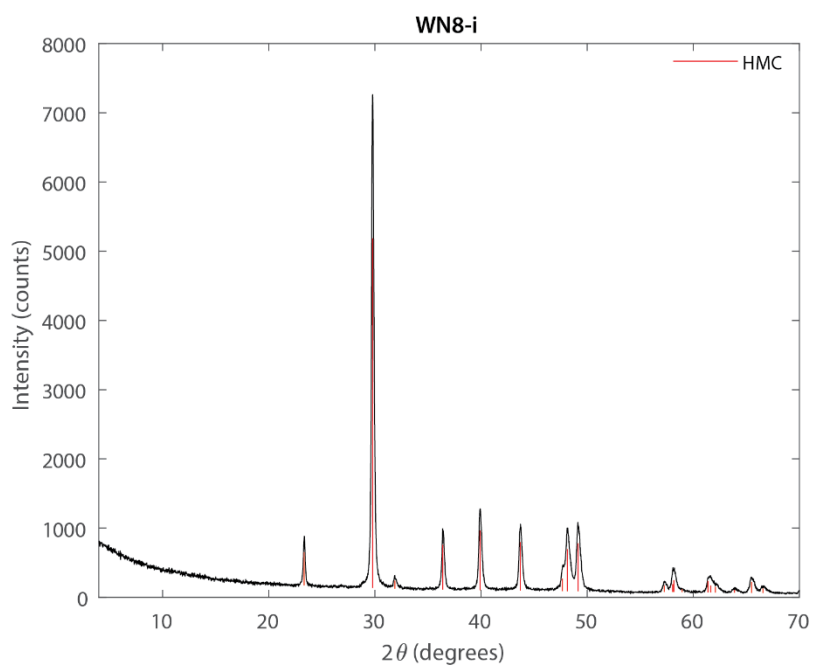


Figure A-12 WN8-i XRD Spectra

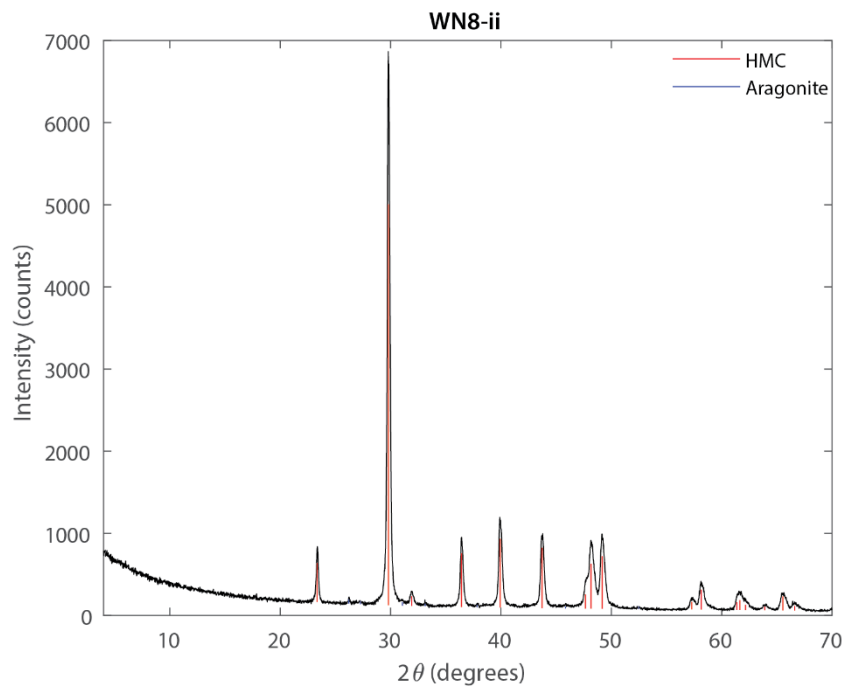


Figure A-13 WN8-ii XRD Spectra

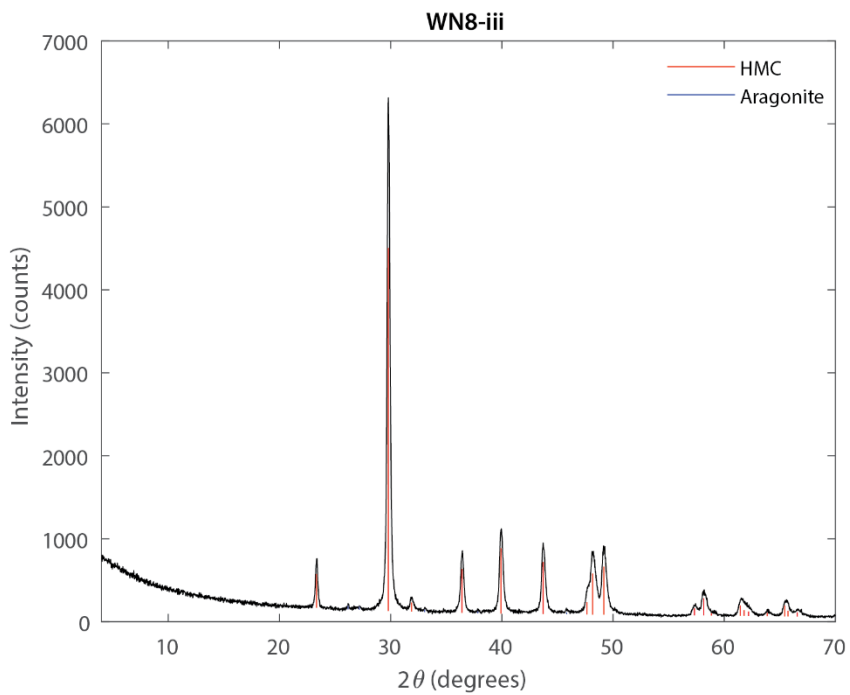


Figure A-14 WN8-iii XRD Spectra

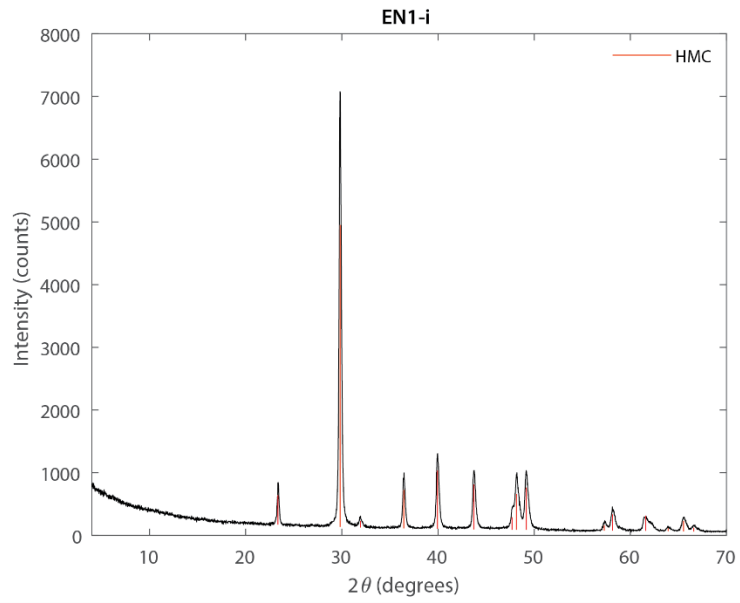


Figure A-15 EN1-i XRD Spectra

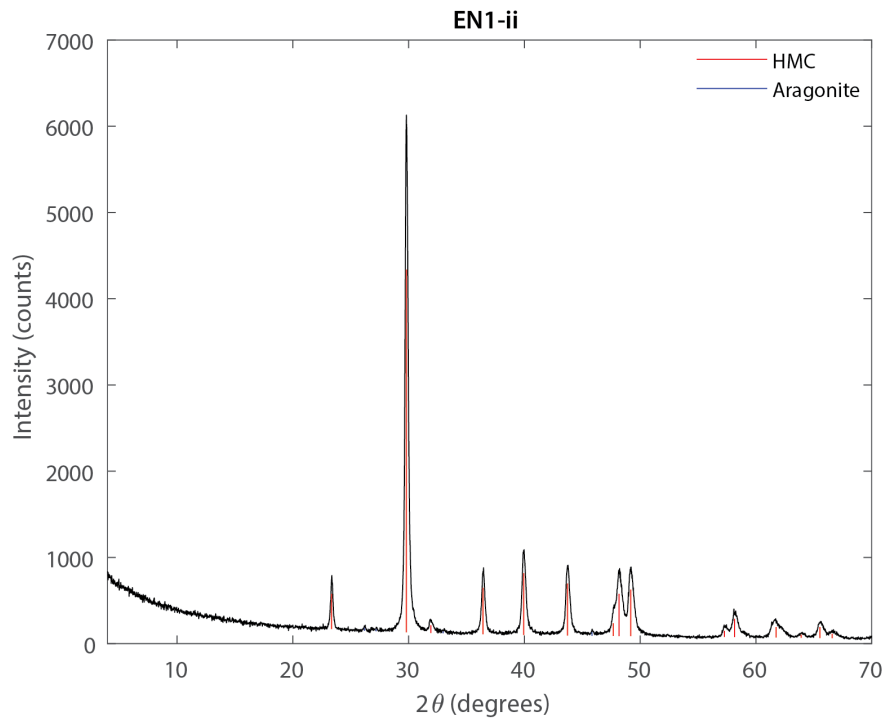


Figure A-16 EN1-ii XRD Spectra

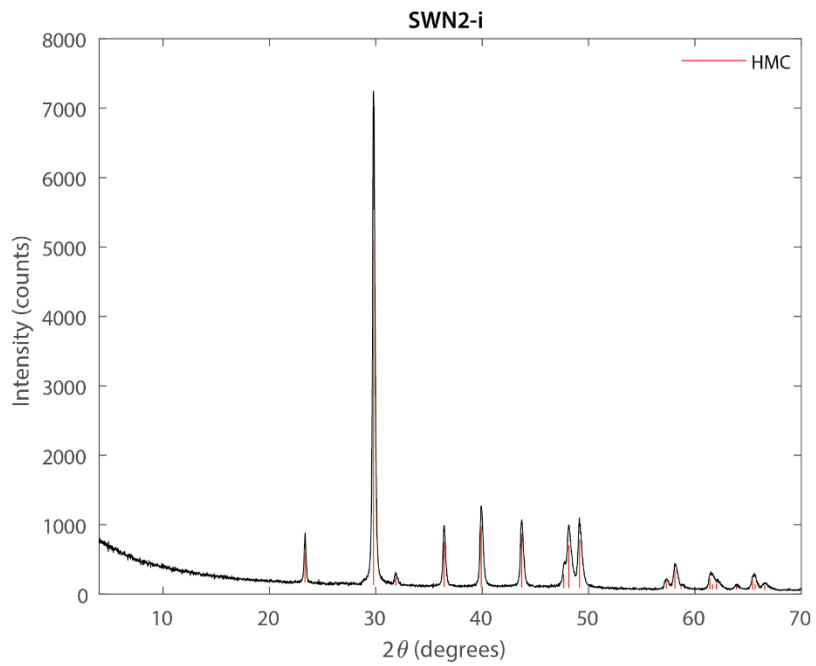


Figure A-17 SWN2-i XRD Spectra

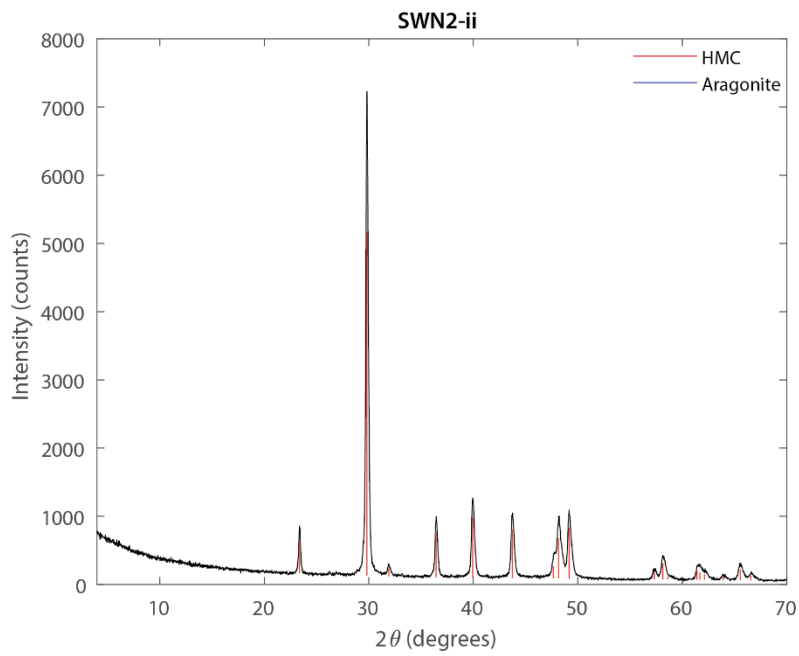


Figure A-18 SWN2-ii XRD Spectra

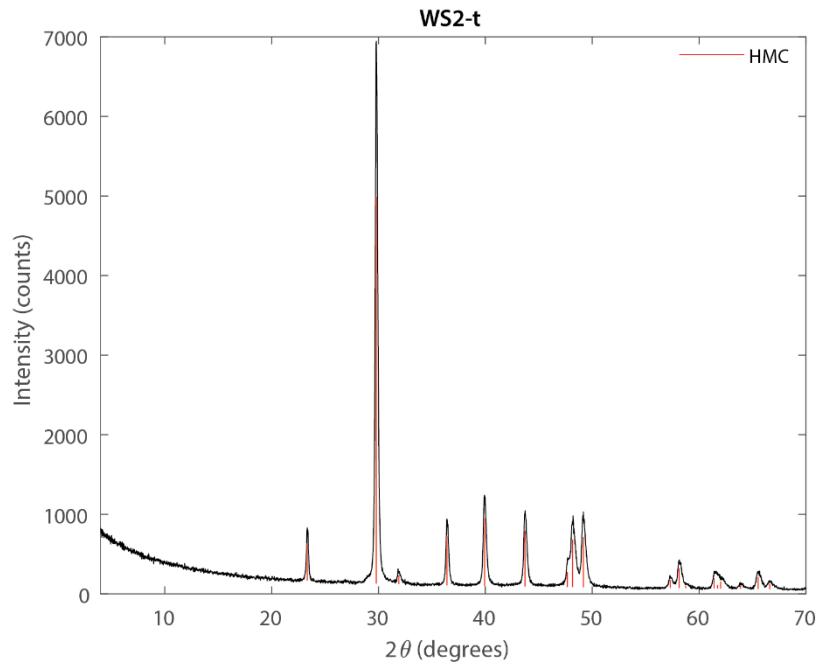


Figure A-19 WS2-t XRD Spectra

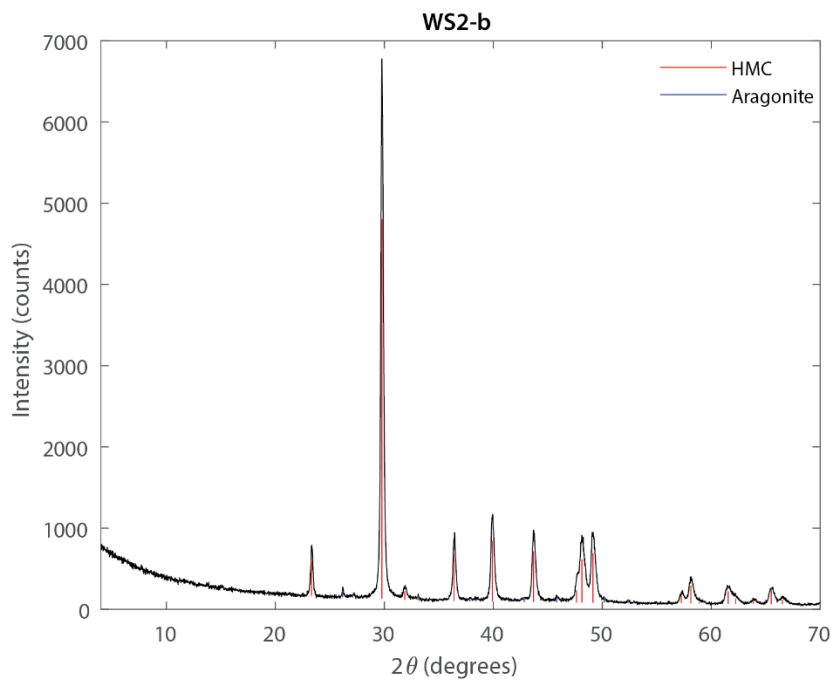


Figure A-20 WS2-b XRD Spectra

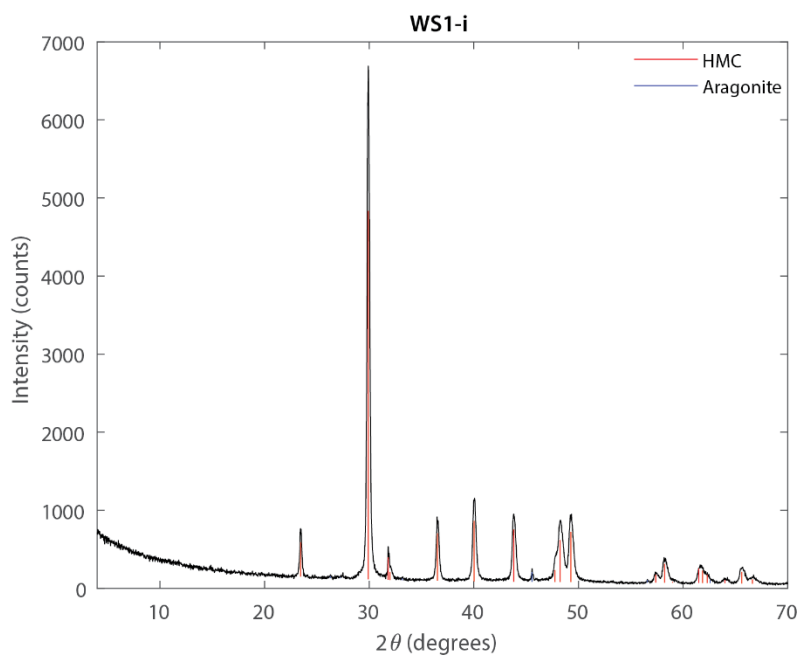


Figure A-21 WS1-i XRD Spectra

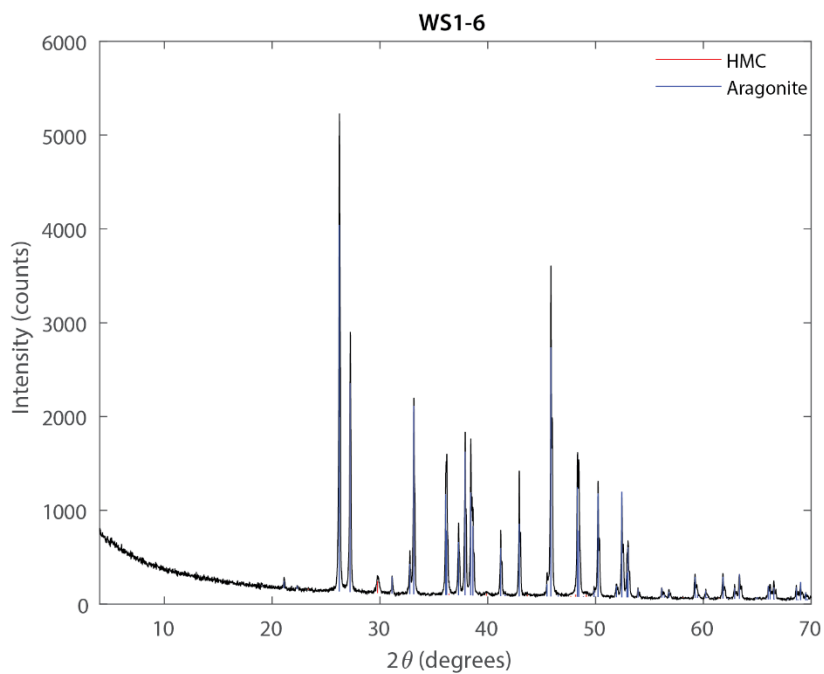
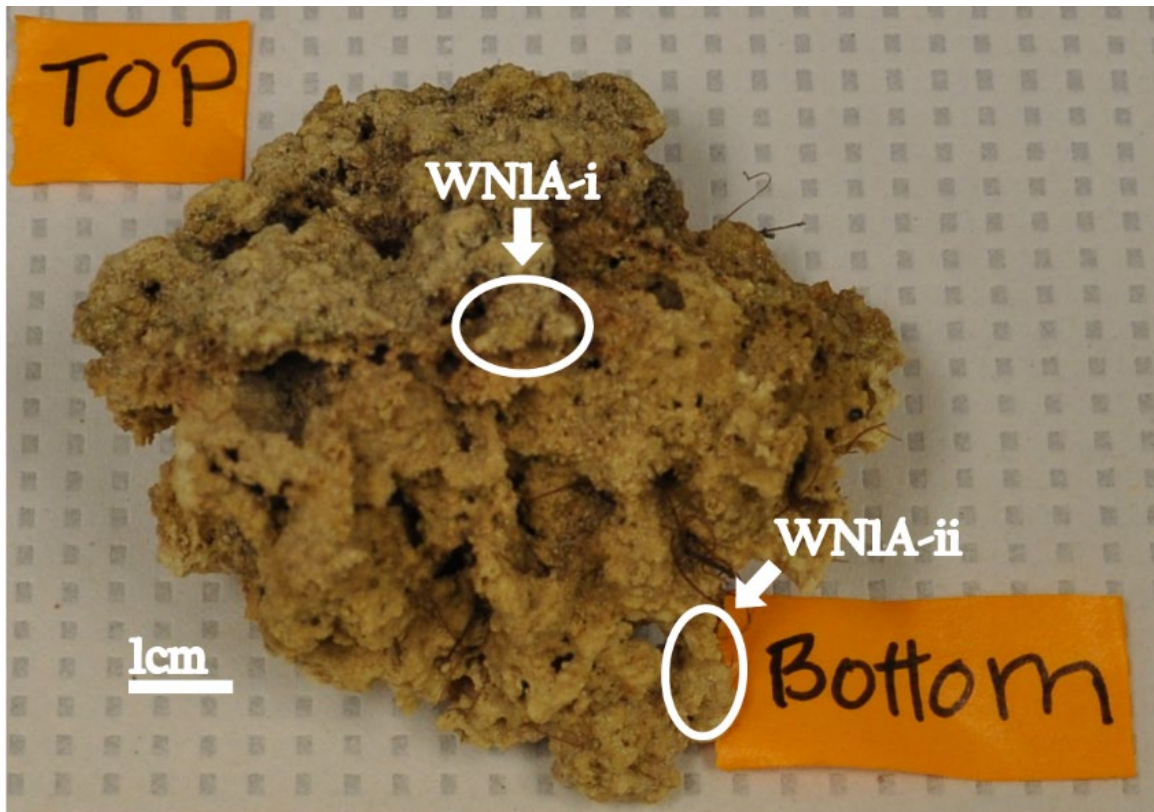


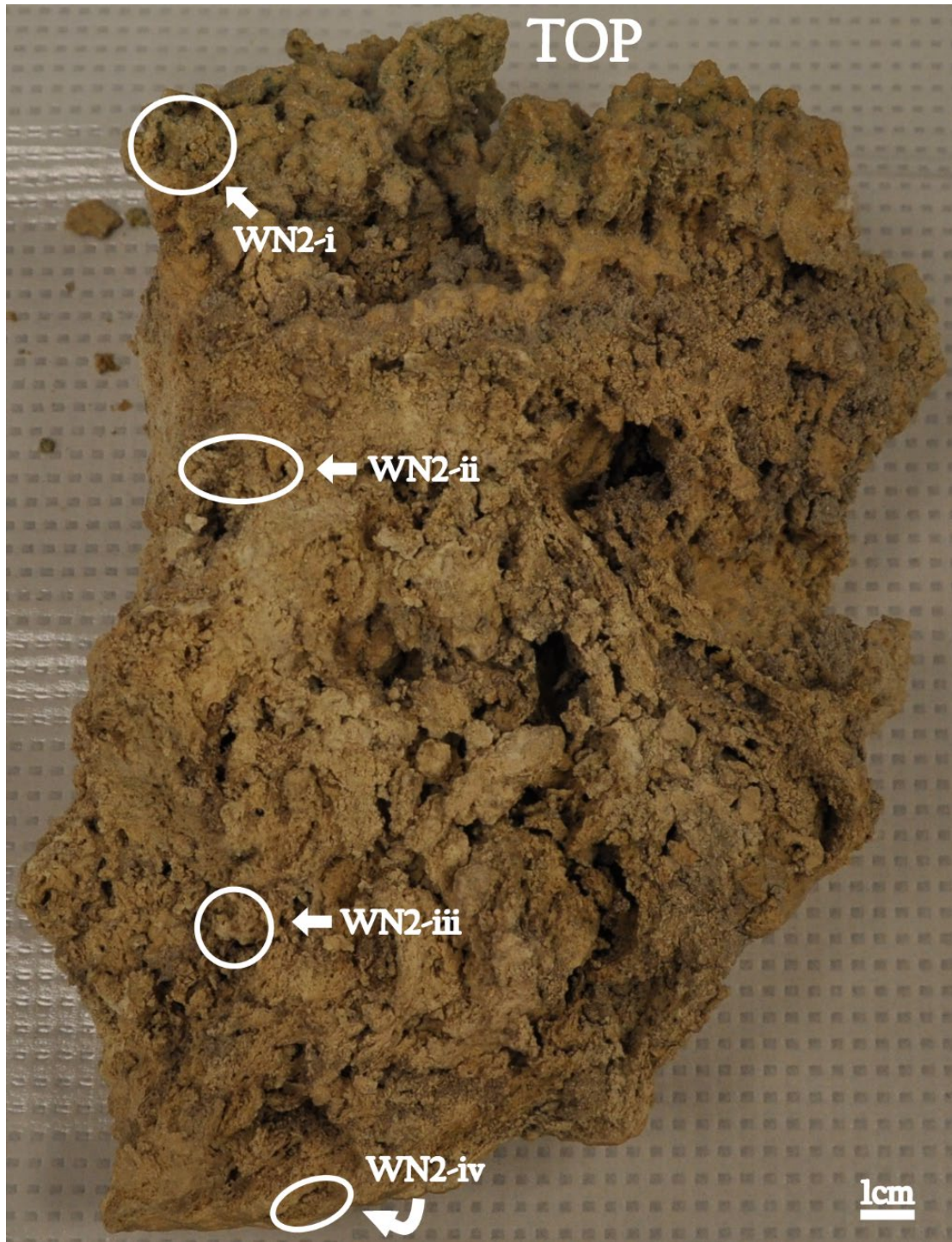
Figure A-22 WS1-6 XRD Spectra

Appendix B. Microbialite Subsample Locations



WN1A is the whole microbialite, but two microbialites were collected at this site, A and B. Only A was subsampled for this research.

Figure B-1 Subsamples Locations for WN1A



WN2 is a slice off of a much larger microbialite that was returned to the lake after hand sample collection. WN2-iv is the smooth exterior of the microbialite.

Figure B-2 Subsample locations for WN2

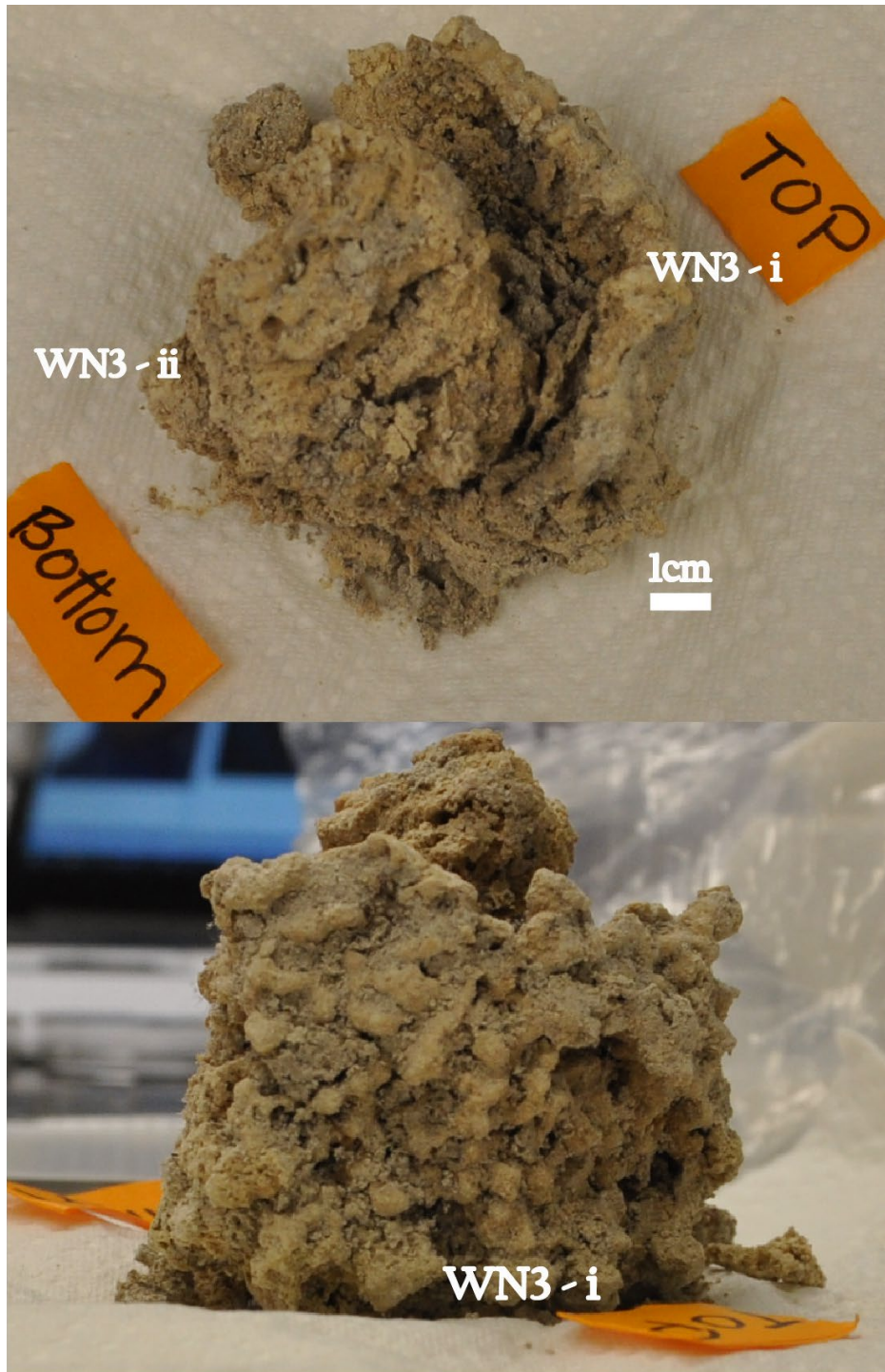
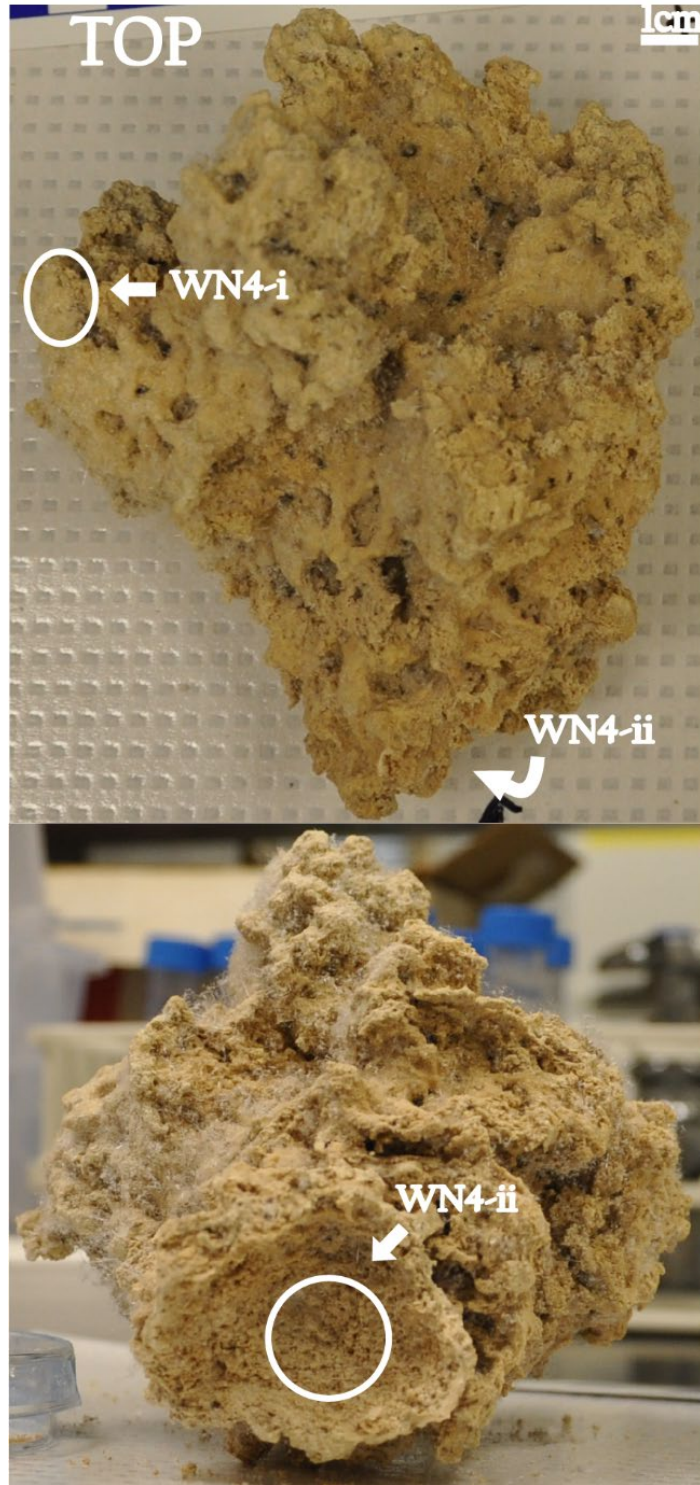


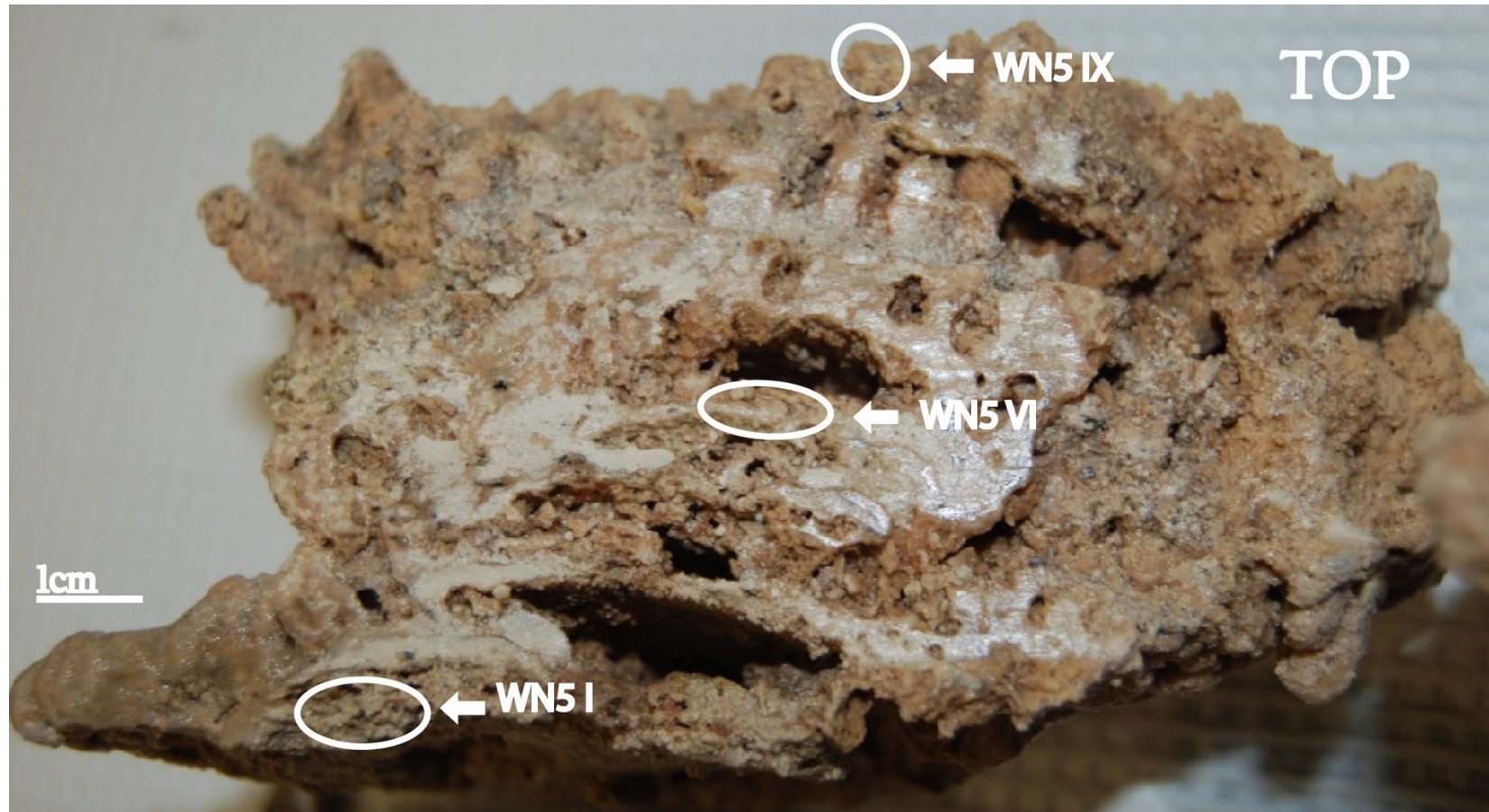
Figure B-3 Subsample locations for WN3

WN3 had crumbled extensively since collection in 2016. WN3-i is likely the exterior based on morphology and field photos. WN3-ii is definitely an interior sample.



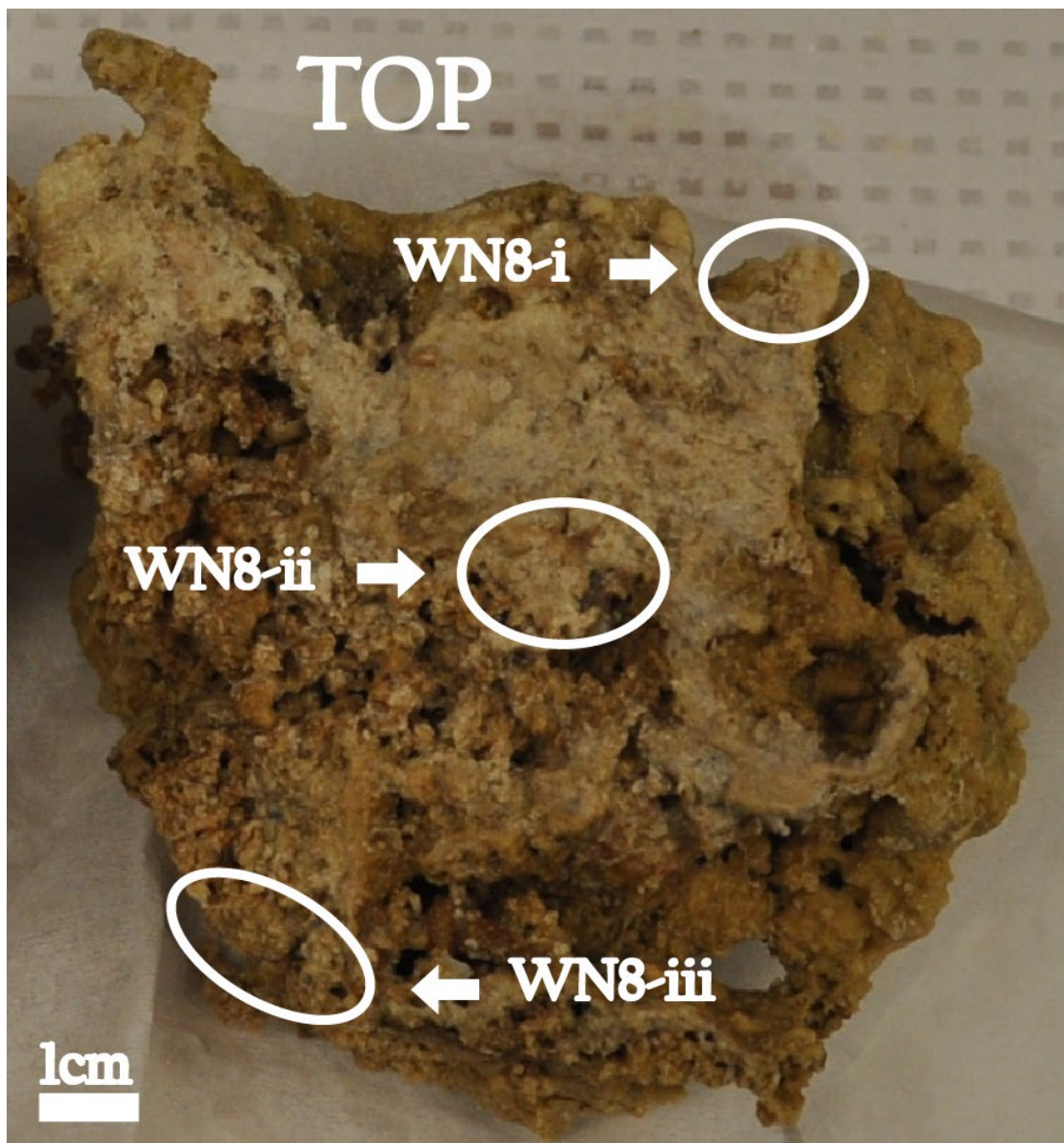
WN4 is a subsample of a larger microbialite. WN4-ii is taken from the interior of the bottom portion of the subsample.

Figure B-4 Subsample locations for WN4



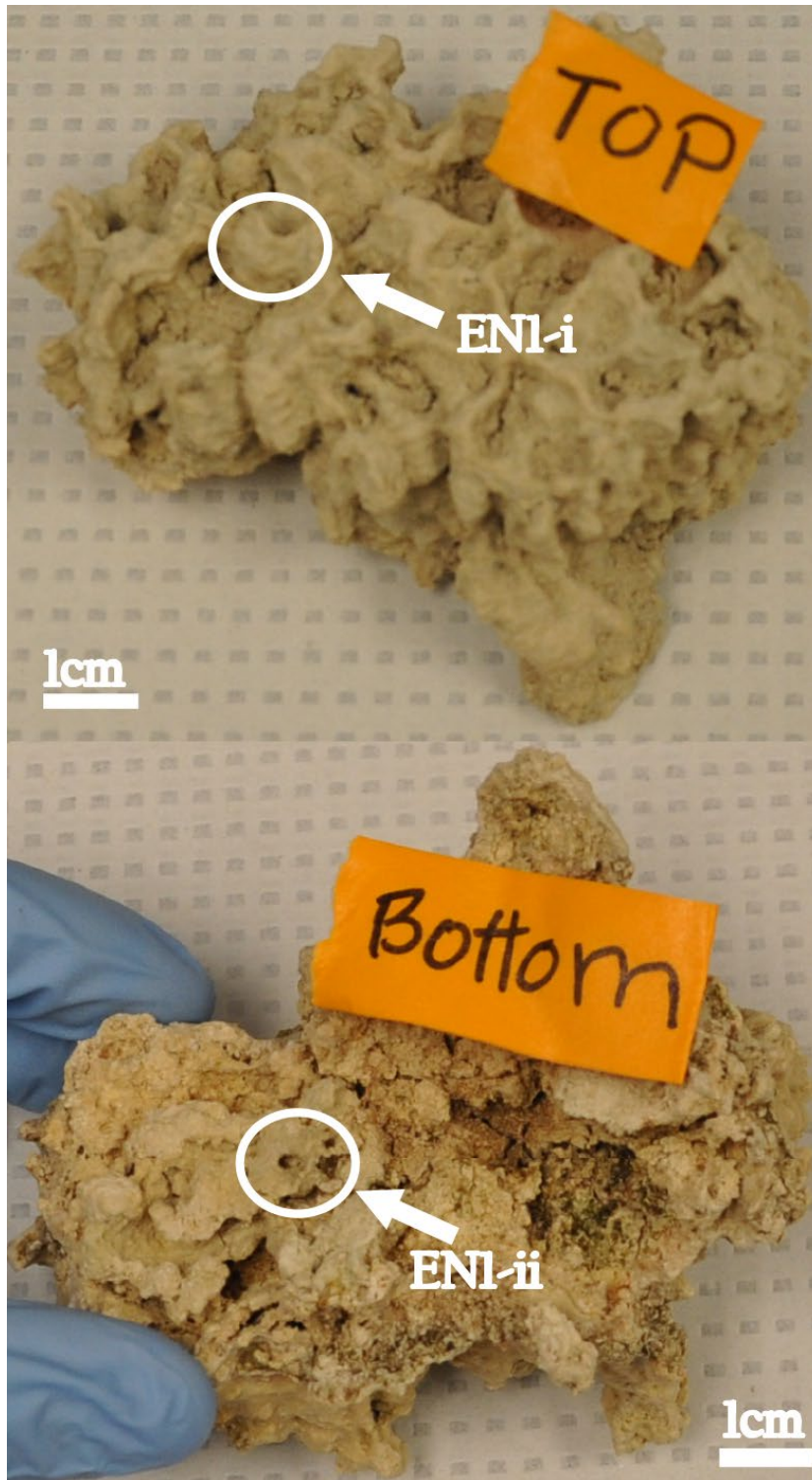
WN5 is half of the microbialite collected. The hand samples was cut in half in the lab and the fresh face is upward in this photograph.

Figure B-5 Subsample locations for WN5



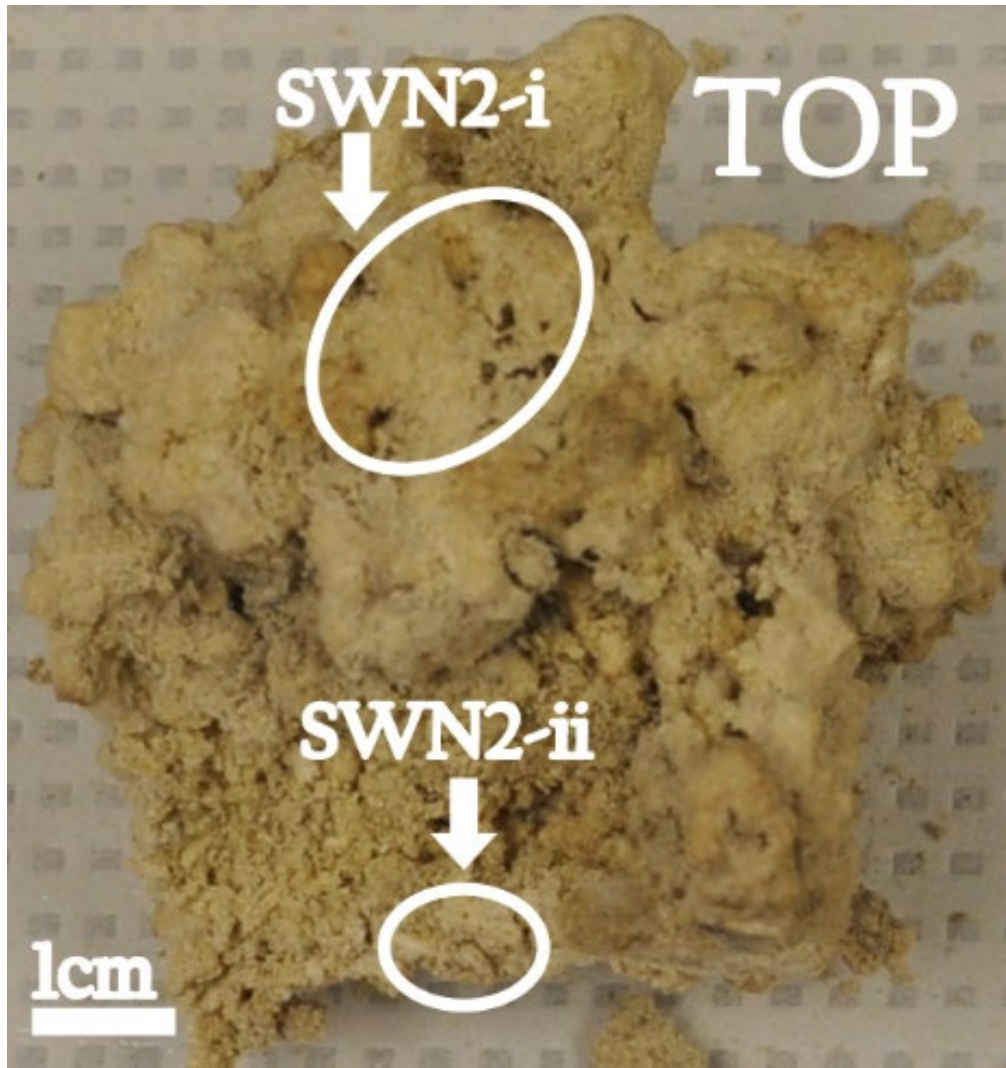
WN8 was cut in half in the laboratory, but is half of the whole microbialite found at the site. The fresh side is facing up in this photograph.

Figure B-6 Subsample Locations for WN8



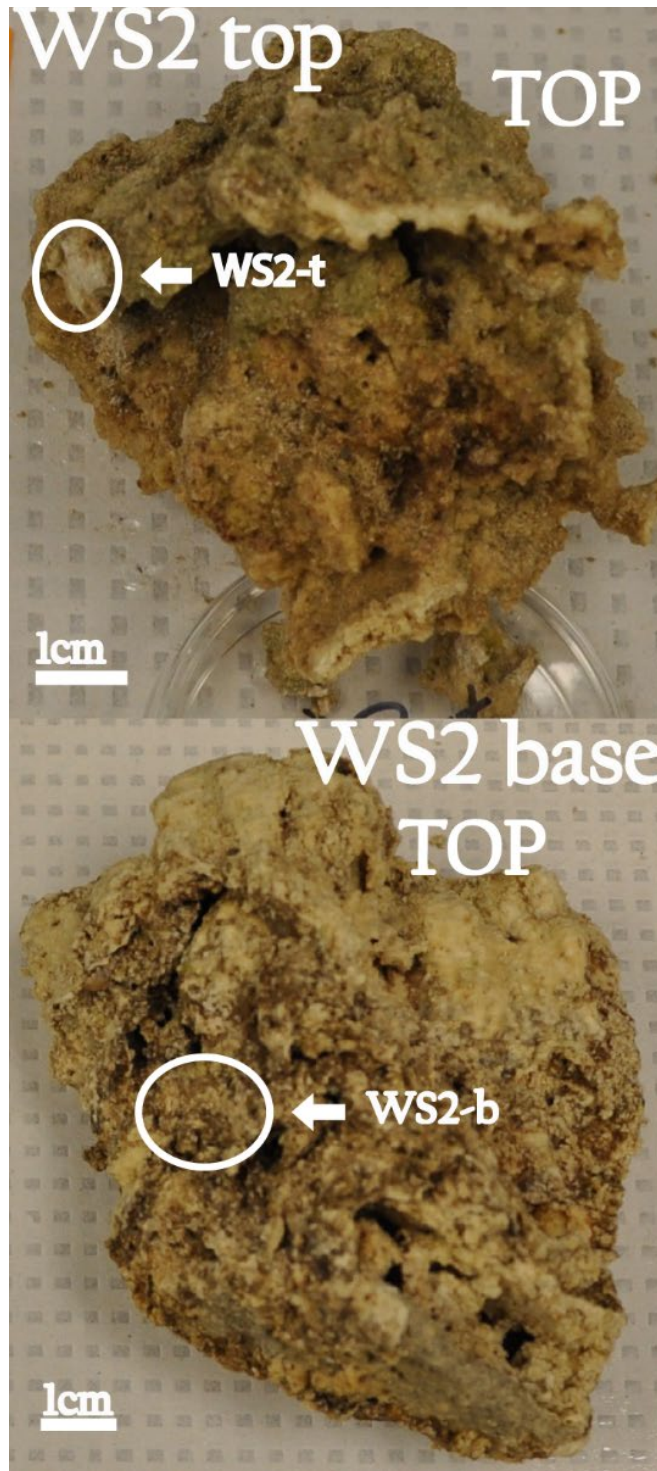
EN1 is the whole microbialite collected at this site.

Figure B-7 Subsample Locations for EN1



SWN2 is half of the microbialite collected at this site. The sample was cut in half in the lab and the fresh side is facing up this photo.

Figure B-8 Subsample Locations for SWN2



WS2 is a portion of the microbialite found at this location. The hand samples were split in half and stored separately. The top sample is from the upper portion of the microbialite and the base sample was in contact with the lake bottom.

Figure B-9 Subsample Locations for WS2

Appendix C. Laboratory SOPs and checklists

C.1 Microbialite Carbonate Subsampling and Preparation Method

***modified from Zijian Li's thesis (2017)**

Required Materials:

- Clean work space
- Containers for the subsamples
- Clean tweezers
- High resolution camera
- Scale bar for photos
- Sharpie to label the background in each photo
- Clean agate mortar and pestle

Subsampling method:

- Lay out a clean workspace for each microbialite
- Label the sheet and lay out the scale bar for the before picture
- Take a picture with the tweezers pointing out the location
- Carefully take the subsample (~0.5g; 6mg for digestion and 0.14g for XRD) and put it in the correctly labelled dish
- Take an after picture

- Repeat the process for the desired number of subsamples from each microbialite

Preparation method:

- Thoroughly clean and dry the mortar and pestle with MilliQ water
- *Gently* crush the subsample to a fine powder
- Carefully pour the powder into an acid cleaned falcon tube
- Add ~2-7mL of MilliQ water to tube and swirl/vortex to remove soluble salts
- Centrifuge the sample and carefully decant the MilliQ water
- Repeat twice more
- Dry the subsample in an oven overnight at 55°C
- If needed, re-powderize the sample in the morning

6mg of the sample will be dissolved for elemental and stable isotope analysis. The remaining 140mg will be prepared for XRD analysis.

C.2 Microbialite Carbonate Digestion Method

*modified from Li (2017)

Required Materials:

- Microbialite subsections (~6mg; crushed and rinsed as per subsampling method)
- Acid cleaned Teflon vials (15mL); one for each subsample
- 2N distilled HCl
- 30% H₂O₂
- 2% distilled HNO₃
- **Don't forget to prepare a method blank**

Digestion method:

- Weigh 6mg of rinsed microbialite powder into a clean Teflon vial
- Add 1mL 2N HCl, then sonicate for 30mins, dry on a ~90C hotplate
- Add ~1mL of 30% H₂O₂ to each vial, sonicate for 5mins, and reflux on a ~90C hot plate for 30mins
- Then uncap each vial and let them dry on the hotplate
- **REPEAT** H₂O₂ steps
- Dissolve in 3mL 2% HNO₃ and sonicate 10mins

One third of each sample is removed to a falcon tube and diluted to 5mL with 2% nitric for elemental analysis, the remainder is used for Ca isotopic analyses.

C.3 Cation Exchange Column Method for Calcium Isotopes

***don't forget the worksheet**

Preparing the materials (*done days before doing column work*):

- Clean the MCI resin **typically already done**
- Clean 3 vials for each sample and blank (collection and safety)
- Prepare 1.8N ultrapure (Optima) HCl (calibrated)
- Prepare 6N ultrapure (Optima) HCl– note 50% by volume works
- Samples should be spiked with double spike before column work - *Combine and sonicate for 10mins to mix completely*

Preparing Ca Samples for Ca Columns (*done at least 1 day before doing column work*):

- Dry down (evaporate) sample on hotplate (@100 to 150 deg C), ~1 hour per ml
- Reconstitute dried sample in 75 uL 1.8N HCl - *Ultrasonicate if needed to completely dissolve sample (~10 minutes)*

Ca Column Methodology for Ca isotopes

1. Fill columns with MilliQ on rack; using pipette to force air out of column
 - Verify both frits are place correctly
2. **Wash column** with 10mL 6N HCL
3. **Wash column** with 10mL MilliQ
4. **Load ~1 mL MCI resin** in water onto columns filled with water
 - *Remove excess water from reservoir, leveling resin bed above reservoir bottom*

5. **Wash columns** with 3 mL of 6N HCl (if needed sonicate samples during this run)
 - *Takes ~1 hr and 20 mins*
6. **Wash columns** with 3 mL of MilliQ - *adjust resin*
 - *Takes ~2.5-3 hrs – HIGHLY VARIABLE*
7. **Condition the columns:** with 2 mL of 1.8N calibrated HCl - *adjust resin*
 - *Takes ~1 hr and 15-30 mins*
8. **Load the sample** onto the column (75 uL of 1.8N HCl)
9. **Continue to load the sample by rinsing the sample vial and adding 50 uL twice, then 100 uL twice, then 200 uL**
10. **Wash with 3 ml of 1.8N HCl**
 - *Takes a little less than 2 hrs*
11. **Wash with 1.5 mL 1.8N HCl AND COLLECT for Ca**
 - *Takes ~1 hr*
12. **Wash with 3 mL 6N HCl; SAFETY** collection for potential Ca,
IMMEDIATELY switch to the safety collection Teflon vial after adding 6N HCl
13. Let columns run past the reservoir base for an extra 30mins or overnight
14. Remove collection vials

Discard the resin in the used resin waste bottle. Clean columns with 3 MilliQ rinses and return them to their home.

C.4 Calcium Column Worksheet

Ca separation cation exchange column using MCI gel resin								
Date: _____	Description	time start	Blank	2-	3-	4-	5-	6-
10 ml 6N HCl	wash							
10 ml MilliQ	wash							
Load 1 ml Resin	load							
3 ml 6N HCl	wash							
3 ml MilliQ	wash							
2 ml 1.8N HCl	condition							
Load Sample (75 ul)	SAMPLE							
50 ul 1.8N HCl	rinse sample vial							
50 ul 1.8N HCl								
100 ul 1.8N HCl								
100 ul 1.8N HCl								
200 ul 1.8N HCl								
3.0 mL 1.8N HCl	RINSE							
1.5 mL 1.8N HCl	COLLECT for Ca							
3 mL 6N HCl	COLLECT for safety							

C.5 MCI Gel Resin Cleaning Method for Calcium Isotopes

Work in clean lab only. Wear gloves and safety glasses.

1. Spoon dry MCI Gel CK08 resin into a large clean Teflon Container.
2. Fill the bottle with **milli-Q** water and shake vigorously. Allow resin to settle (this will take several hours). Decant water. Repeat twice more.
3. Fill the bottle with clean **8N HCl** and shake vigorously. Allow resin to settle. Decant acid to water container. Repeat 3 more times.
4. Fill bottle with **milli-Q** water and shake vigorously. Allow resin to settle. Decant water. Repeat twice more.
5. To make pH 5-6; continue rinsing with water until pH increases. Usually this is around 9x the volume of resin.

C.7 Sr-Spec Column Chemistry Method

*** don't forget the worksheet * entire method takes about 8 hours**

Required Personal Protective Equipment:

- Nitrile gloves
- Safety goggles
- Closed toed shoes

Preparing materials (*done days before doing column work*):

- Place columns in 8N HNO₃ overnight (cleaning empty columns)
- Clean the resin with 0.005 M HNO₃ several times (>3 times)
- Clean 2 vials for each sample and blank
- Prepare 0.005 M ultrapure (Optima) HNO₃ – 3% by volume
- Prepare 8 M ultrapure (Optima) HNO₃ – note 50% by volume works

Preparing Samples for Sr Spec Columns (*done at least 1 day before doing column work*):

- Add ____ mL of sample solution equivalent to 3 ug Sr to clean Teflon vials
- Dry down (evaporate) sample on hotplate (@100 to 150 deg C), ~1 hour per ml
- Reconstitute dried sample in 100 uL 8M (50%) HNO₃. Ultrasonicate for at least 10 minutes (while washing column).

Sr Spec Column Methodology (~hour per mL):

15. Take columns out of 8N HNO₃ and rinse in sink with MilliQ three times.
 - *First rinse should go in the hazardous nitric waste*

- *Use tweezers, but be sure to rinse tweezers with water many times before storing for next use.*
16. Fill columns with MilliQ on spinning rack; using pipette to force air bubbles out of the column
 17. **Load ~125 uL Sr Spec resin** in MilliQ onto columns filled with water
 - *Remove excess water from reservoir, leveling resin bed to just at reservoir bottom*
 18. **Wash columns** with 600 uL of 0.005N HNO₃ (wait until water level has reached the resin bed)
 19. **Condition the columns:** with 200 uL of 8N HNO₃ (wait until liquid level has reached resin bed)
 20. **Immediately load the sample** onto the column (100 uL of 8N HNO₃ from weighed Teflon vials)
 - *Load sample into bottom of the reservoir so it is immediately flowing through the resin*
 21. **Wash vial with 2mL 8N HNO₃**
 22. **Add 2mL 0.005N HNO₃ AND COLLECT for Sr isotopes** (wait until last mL of 8N HNO₃ is at the resin bed)
 23. **Immediately** remove waste collection vials; replace with empty (clean) Teflon collection vials for Sr
 24. Let liquid drain into resin bed and through the column for an extra half hour

After finishing the chemistry, discard the resin in the resin waste bottle and clean the columns by rinsing thrice with MilliQ and then placing them back in the container with 8M HNO₃. Make sure to use a pipette to pull acid up into the columns. Let them soak and clean overnight.

C.8 Sr-Spec Column Worksheet

Sr-specific column separation for carbonates/waters method

Date: _____			BLANK	2-	3-	4-	5-	6-	7-	8-	9-	10-	11-	12-
	Description	time start												
~250uL resin in MilliQ	load resin													
600uL 0.005N HNO3	wash resin													
200uL 8N HNO3	condition													
100uL in 8N HNO3	SAMPLE													
100uL 8N HNO3 wash vial	SAMPLE													
900uL 8N HNO2	COLLECT for Ca													
1mL 8N HNO3	COLLECT for Ca													
2mL 0.05N HNO3	COLLECT for Sr													

C.9 Loading Sr on Single Re Filaments

*Modified from the Thermo Triton loading method *in 359C Mendenhall

***NOTE: Remember to clean each pipette tip before using it. Everyone uses the same standard and activator. BE MINDFUL.**

NOTE: It is your responsibility to have to following items prepped PRIOR to loading

- Outgassed filaments – preferably outgassed 1 week prior to loading, but no more than 1 month
- Clean shields
- Clean blanks – these may be in place on the wheel already, but you should have them prepared if they are not
- Loading solution – 1N HNO₃ or 2N HNO₃
- Dried down samples

Required Personal Protective Equipment:

- Lab coat
- Lab goggles
- Nitrile gloves
- Closed toed shoes

Loading Procedure:

1. Wipe down work surface with Milli-Q
2. Set up wheel – move from dry box to loading area
 - a. *Make sure there are enough blanks to fill wheel*

3. Gather supplies – outgassed filaments, clean shields, dried down samples, pipette tips (2 times the number of samples plus some extra)
4. Remember to fill out sheet specifying sample location on the wheel
 - a. *Do this just for the filaments you are currently loading*
 - b. *Line up those 3-5 vials in the order that they are to be loaded onto the filaments*
 - c. *Don't forget your standards! At least 3 for each wheel.*
5. Organize work area (e.g. open HCl and Milli-Q cleaning vials and place them within easy reach)
 - a. *Pipette tips are cleaned as you use them, 1 volume of HCl followed by 3 volumes of Milli-Q deposited into the waste bottle. You may need to tap the side of the pipette to get the drop to fall*
6. Put filament posts gently into their positions on the loading mechanism with the switches off and the amperage set to zero
7. Flip the switches on for each filament
 - a. *Verify that the machine is in "single" mode*
8. Slowly turn the amperage up to 0.6A
9. Load 0.5 μ L of activator onto each filament
 - a. *SWIRL or SHAKE activator before each use - this is very important as the solids in the solution settle out very quickly*
 - b. *This solution contains very small amounts of HF, so the pipette tips go into the waste container*

- c. *DO NOT touch the tip to the filament; surface tension is your friend*
 - d. *Center the droplet as much as possible*
10. **Record any weirdness that may affect your data** (e.g. off center load, white fleck from the activator, accidentally touching filament with pipette tip, etc...)
- a. *This applies for the whole loading process*
11. Wait for the activator to be “almost” dry before loading sample or standard
- a. *This is subjective, it is also okay if the activator is completely dry*
12. **LOADING STANDARDS** – load 1 μ L straight from the small vial of SRM 987
- a. *This is 500ng of Sr*
 - b. *This is precious; put away immediately after use*
13. **LOADING SAMPLES** – dissolve in 1 μ L of loading solution (1N or 2N nitric acid) and load onto filament
- a. *Pull droplet around in the vial to find the sample, DO NOT scrape the Teflon*
 - b. *Mix with pipette tip to pick up sample (pull droplet in and out of tip; DO NOT pull up from second position)*
 - c. *Verify loading correct sample onto the right filament*
 - d. *Load directly on top of activator, even if off center*
14. Onto dry sample or standard, load 0.5 μ L of activator; don’t forget to SWIRL or SHAKE
- a. *Again tips go into the waste container*
15. **Record any weirdness that may affect your data**

16. Once all filaments are dry, SLOWLY turn up current to 1.8A and heat for 1min
 - a. *Use timer on the wall*
 - b. *During this time turn off all the lights in the lab*
17. **SLOWLY** turn up current until filament glows a dull red, then immediately switch it off; this will happen at different times for each filament
18. Load filament posts onto the wheel using Lindström pliers and cover them with shields immediately to protect them
 - a. *BE CAREFUL, it would be unfortunate to bend a filament now*
 - b. *Make sure the shield clicks into place*
 - c. *Homemade filaments may not be centered within the eye of the shield – check and record this*

Now repeat until all samples and standards for this wheel have been loaded.